Version 3
April 13, 2015

CALIBRATION DOCUMENT
OF
CADMIUM ZINC TELLURIDE (CZT) – IMAGER
ASTROSAT

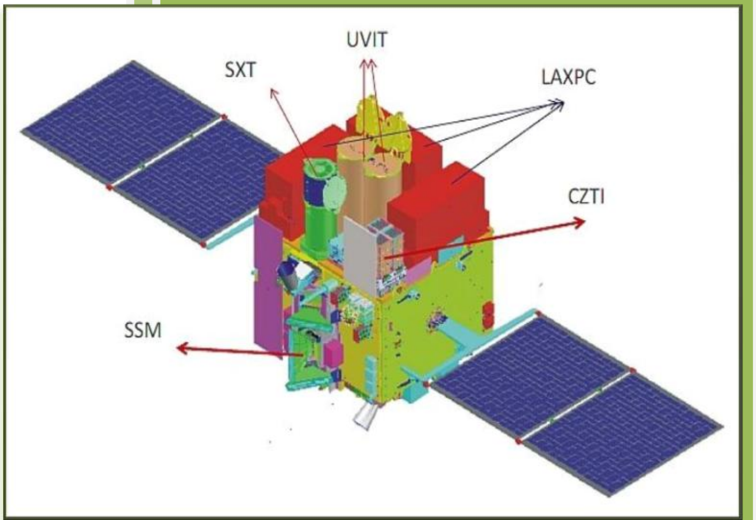

Prepared by

CZT Imager Team

- Tata Institute of Fundamental Research, Mumbai
- Vikram SarabhaiSpace Centre, Trivandrum
- Inter-University Center for Astronomy & Astrophysics, Pune
- Physical Research Laboratory, Ahmedabad

CONTENTS

1. Introduction ……………………………………………………………………………….....4

1.1 CZT Imager Configuration……………………………………………………....5

2. CZTI Calibration……………………………………………………………….....…...8

2.1 Evaluation of the dead, noisy, and bad pixels in CZTI……………...................8

2.2 X-ray spectroscopic calibration at various temperatures………………..……....13

2.3 Threshold Estimation..20

2.4 CAM Calibration……………………………………………………......…......25

2.5 Alpha-tagging in CZTI……………………………………………….....……27

2.6 Veto calibration………………………………………………………...…….27

2.7 Time tagging, cross talk and polarization capability of CZTI ……………..…….31

2.8 Response matrix generation for CZTI……………………………………..….....44

2.9 Testing at various modes…………………………………………………..…......45

2.10 HK Parameters...55

2.11 STBG Test...56

3. Tests and Evaluations of Detectors…………………………………………...…...57

3.1 Test Setup……………………………………………………………….....…...57

3.2 Test Sequence………………………………………………….……….…......58

3.3 Test Results for QM module……………………………………..…...........59

3.4 Test Results for FM module…………………………………………....…...62

4. Concluding remarks………………………………………………….…...…......63

Annexure I: A technical report on CAM testing 68

Annexure II: A draft paper on Alpha tagging 86

Changes made in this version (Version 2.0; December 2014)

In this version of the document (Version 2.0), the Flight Model (FM) calibration results are included. The following information may be used as a guide to go through the document.

Calibration results of CPM are completely removed and this information is given as a separate document.
Introduction: A section is added to give the overall configuration details, along with definitions of pixels, modules, quadrants etc.
A new sub-section (2.9) is added to give FM calibration results.
A new section (section 3) is added to give details of the FM qualification procedures and results.
Annexure III: The minutes of the calibration committee are answered point-wise
Annexure VI: The published version of the polarization paper is included here.
At the end of concluding remarks (section 4), a list of future work is given.

Apart from this, cosmetic changes are made throughout and other changes are indicated as response to calibration committee minutes.

Changes made in this version (Version 2.1; 10 April 2015)

1. Final close-out added as Annexure VIII

Changes made in this version (Version 3; 13 April 2015)

1. All annexure are removed, excluding annexure IV and V and listed them as annexure I and II respectively.
2. Figure 2.11 has been superseded with new one and labeled as fig. 2.12.
3. Minor corrections made throughout the document.

1. Introduction

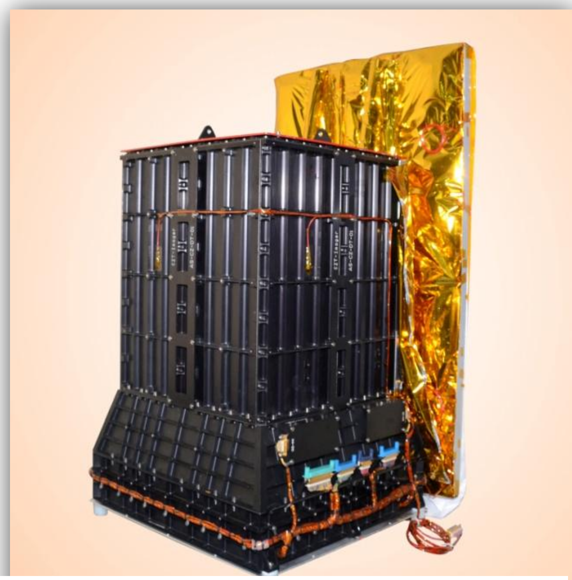

Cadmium Zinc Telluride (CZT) – Imager

The Cadmium Zinc Telluride (CZT) – Imager is one among the four X-ray instruments on ASTROSAT which covers a broad energy band of X-rays extending from 10 keV to 100 keV. It has a large detection area of976 cm^2 comprising of the CZT detector modules and uses an imaging process known as Coded Aperture Mask (CAM). The CZT detectors provide us with high stopping power, low thermal noise, room-temperature operation and excellent energy and spatial resolution. The Coded Aperture Mask is a method particularly suited to high energy radiations like X-rays and ϒ-rays where mirrors and lenses become impractical. The salient features of CZT-Imager are given in the following table 1.

Area	976 cm^2
Pixels	16384 (64 modules of 256 pixels each)
Pixel size	2.46 mm × 2.46 mm (5 mm thick); edge row pixels are 2.31 mm wide instead of 2.46 mm
Read-out	ASIC based (2 ASICs per module)
Imaging method	Coded Aperture Mask (CAM)
Field of View (10-100 keV)	$4.6^o \times 4.6^o$ FWHM (primary FOV) $11.8^o \times 11.8^o$ FWZM (incl. illumination leakage)
Angular resolution	~ 8arcmin (18 arcmin geometric)
Energy resolution	~ 5% @ 100 keV
Energy range	10 – 100 keV Up to 1 MeV (Photometric); no imaging above 100 keV
Sensitivity	0.5 mCrab (5 sigma; 10^4 s)
Memory	50 Mbytes per orbit

Table 1: CZTI features

The CZT Imager (CZTI) consists of two packages viz., the detector box and the processing electronics(PE). The detector box consists of 4 identical and independent quadrants while the PE package essentially consists of a power card and FPGA-card. All the satellite communications are handled by the PE.

The detector box is comprised of two detectors: the main CZT detector and the 'veto' CsI(Tl) detector used for reducing background generated by Cosmic rays and high energy ϒ-rays. The CZT detectors are continuously calibrated by a simultaneous radiation of α-particles and X-rays by a radioactive source (Am^{241})in the alpha box. A collimator along with the CAM is used to obtain moderate imaging to distinguish multiple X-ray objects in the field of view (FoV).

This document gives the calibration and test & evaluation results of the Flight Models (FM) of the CZTI payload. The comprehensive design and technical details and the QM test results are available in the Preliminary Design Review/Critical Design Review (*TIFR/AST/CZTI-CPM/CDR-01)* documents.

1.1 CZT Imager Configuration

The main scientific requirement of CZTI is to construct a low background X-ray detector to observe spectrum between 10 keV to 1 MeV and also do moderate imaging up to 100 keV. The overall area of 976 cm^2 is achieved using a total of 64 CZT detector modules of size 39 mm × 39 mm and thickness 5 mm, divided into 4 quadrants. Each detector module consists of a total of 256 (16×16) pixels of size ~ 2.5mm × 2.5mm and thickness 5mm. Each pixel is connected to a pre-amplifier embedded in an ASIC. The CsI(Tl) veto detector which is basically a scintillation detector acts as an active shield to the background counts. It is viewed by two photomultiplier tubes and has a minimum detection sensitivity of 50 keV. In the alpha box, a CsI crystal embedded with a radioactive Am^{241} source is viewed by a photo-diode. At every disintegration of an Am^{241}nucleus, a 60 keV photon as well as an alpha particle is emitted. The alpha particle gets absorbed in the CsI crystal while the X-rays are incident on the CZT detector below the crystal. The timings of both the detector pulse and the crystal pulse are looked for a match to identify the calibration events, and using them the detector is calibrated.

The PE consists of an FPGA, an EEPROM acting as the boot memory for the embedded processor, power-on circuits as well as various interface circuitries. The power card also routes the power supply to the detector quadrants. The satellite Bus Management Unit (BMU) provides pulse commands, data commands and the Low Bit rate Telemetry (LBT) and these are handled by the PE. The RAM holds the detector data, LBT bytes, High Bit rate Telemetry (HBT) packets, status words along with the temporary data used for preparing the LBT & HBT data. The LBT is transmitted through the BMU telemetry interface and it is used mainly for the house keeping data. A Baseband Data Handler (BDH) with a Low Voltage Differential Signal (LVDS) interface is used for transmitting HBT data. The Detector data is first packetized, then written to the onboard memory and sent periodically in 21 ms intervals to the BDH. The EEPROM holds various versions of the software. Onboard re-programming is possible with the assistance of tele-commands thus facilitating the editing of onboard software. PE also has the LAXPC and CPM interfaces. The LAXPC signal is used for time synchronization while the CPM signal is used to know about the high influx of charged particles in the SAA region. The onboard software would be booted to the RAM based on the respective command. Initialization command would be given foremost, upon which reset release command would be issued to the detectors by the onboard software and each detector would be taken to event mode serially. The software will then scan for second boundary which will issue second command to all detectors.

The primary mode of operation is the Normal Mode where data for every incident event is time tagged and recorded. The event information consists of Module id, pixel id, pulse height (12 bits), alpha-id, associated veto spectrum in 7 bits and time with a resolution of 20 μs.

Definitions

Some of the commonly used terms are defined here:

Pixel: The basic detection element. Actual size: 2.46 mm × 2.46 mm × 5 mm thick CZT crystal. Electronically segregated into this size from a large area crystal in the Detector Module (see below). Edge pixels in a module are of the size 2.31 mm × 2.46 mm and the corner pixels are 2.31 mm × 2.31 mm. Each pixel has its own electronics like amplifiers etc.

Detector Module: A large area CZT crystal of size 39.06 mm × 39.06 mm × 5 mm thick, made from a single block or at most 4 pieces joined together. 256 pixels (16×16) with sizes as described above are electronically segregated and the electronics for all pixels are embedded in two ASICs. The electronics in the ASICs also includes ADC, temperature sensors and digital electronics to make the system work in a self-triggering mode and communicate the results (pixel id and event pulse height in 12 bits) to external circuits. It also contains the required connection to give HV bias and a cold finger to drain the heat.

<u>Quadrant:</u> 16 Detector Modules are arranged in a quadrant in a 4 × 4 matrix. A separation of 2.5 mm (one typical pixel size) is kept between modules. All 16 modules are mounted on a Detector Board and connected to a Front Electronics Board. All cold fingers coming out of the modules are thermally connected to a 3 mm thick Aluminum plate called the internal radiator plate and heat pipes connect the internal radiator to an external radiator. Each module has its own collimator and Coded Aperture Mask. Four identical but electrically independent quadrants make up the full CZT-Imager detector.

2. CZTI Calibration:

The Orbotech CZT detector detectors are meant for commercial use. To qualify these detectors for flight, a rigorous screening procedure was evolved. After the screening process, it was found that the yield was very low (about 65%). Though there were no catastrophic device failures during the screening process *per se*, some devices did fail at the start of the test (about 5% of the detectors); these catastrophic failures are attributed to the inappropriate handling of supply voltages. It was, however, noticed that the number of noisy pixels increased after screening, resulting in the rejection of a large number of detectors (acceptance criterion is that the number of dead+noisy+bad pixels out of the 256 pixels in a given detector should be less than 15).

Hence, it is indeed a matter of concern to know about the number of unusable pixels in a given detector and to have confidence that they will remain within the limits during the onboard operation. The next section specifically addresses this issue.

The CZT detectors are primarily designed as gamma-ray devices (40 – 200 keV) to be operated at room temperature. We are using them as X-ray spectroscopic detectors in the 10 – 100 keV regions. To extend the low energy response to 10 keV, the devices are cooled to 10°C (+/- 5°C) – but in some orbits the temperature can go up to 20°C. The X-ray spectroscopic capabilities are examined critically in the full energy range and the results are given in this report.

CZTI uses a Coded Aperture Mask (CAM) as an imaging device. Calibration of the CAM is done separately. Similarly, the efficacy of alpha-tagging and CsI veto anti-coincidence are dealt with separately. All X-ray photons registered in CZTI are time tagged to an accuracy of 20 μsec. This provided an unexpected bonus of using CZTI as an X-ray polarization instrument above about 150 keV. This aspect of the calibration is discussed separately.

2.1 Evaluation of the dead, noisy, and bad pixels in CZTI

Definitions:

Dead pixels are defined as pixels with zero counts and having no sensitivity to detect X-rays in a given integration.

Noisy pixels are defined as pixels which have counts that are more than 5-sigma above the mean count rate in that detector for a given observation. The mean and sigma for the detector are calculated using an iterative sigma-clipping procedure. These noisy pixels can be considerably reduced by taking appropriate action against the origin of noise.

Bad pixels are defined as pixels whose energy resolution is significantly worse as compared to the other pixels in the detector. In comparison to normal (good) pixels, the average count from the source or background are quite less in number (<10 counts per 150 sec for photo-peak). In this case, the pixels having energy resolution more than 12% are considered as bad pixels.

Pixels which are not dead or noisy are called **photometric pixels.**

Pixels which are not dead, noisy or bad having a very good efficiency and a Gaussian shaped photo peak for any radioactive source and uniform background spectrum are called **spectroscopic pixels.**

Photometric pixels: We flagged dead (D) and noisy (N) pixels at various stages of screening. Based on the number of sub-optimal pixels, and the change in this number with time, we rank the detectors of all quadrants by performance as follows:

Very Good: Total number of dead + noisy pixels is less than 10, and is within 5 of original D+N (Change <= 5).

Good: Total number of dead+noisy pixels is 11-15, or there are 6-10 new D+N pixels since screening.

Fair: Total number of dead+noisy pixels is 16-20

Poor: Total number of dead+noisy pixels is more than 20, or there are 10 or more new D+N pixels since screening.

These criteria are summarized in this table:

	D+N = 0-10	D+N = 11-15	D+N = 16-20	D+N = 21+
Change <= 5	Very Good	Good	Fair	Poor
Change = 6-10	Good	Fair	Poor	Poor
Change >10	--	Poor	Poor	Poor

Table 2.1 Detector grade as a function of total number of Dead+Noisy pixels and change in number since detector

The results of screening and calibration are given in the tables 2.2 to 2.5 below. Columns of this table are as follows:

Current location of the detector on the respective quadrant.

The unique 4-digit ID associated with each detector.

Lot in which the detector was procured.

VSSC screening: Quick integrations at room temperature with ^{241}Am, with LLD (Threshold) set at 40 keV. Dead pixels are ones with zero counts.

Flight calibration at VSSC: Dead, noisy and bad pixels identified from 4 hour data for all sources(^{241}Am, ^{57}Co, ^{109}Cd and BG). T=10°C (ambient) at 15 keV threshold.

Comments and ranking of the detector.

FQ0 DNB List

No.	ID	LOT	Screening	Flight DNB at	Comments
0	3213	1	0D, 0N	1D, 2N, 12B	Very Good
1	5051	2-II	0D, 1N	0D, 1N, 3B	Very Good
2	5384	2-I	1D, 1N	2D, 1N, 0B	Very Good
3	4733	1	0D, 0N	3D, 6N, 2B	Good
4	5685	2-II	0D, 0N	7D, 3N, 5B	Good
5	2999	1	0D, 0N	0D, 2N, 1B	Very Good
6	5323	2-II	0D, 1N	2D, 4N, 4B	Very Good
7	4977	2-II	2D, 0N	7D, 1N, 1B	Good
8	5025	2-II	4D, 0N	5D, 1N, 12B	Very Good
9	5488	3	3D, 1N	6D, 2N, 99B	Very Good
10	5368	2-I	0D, 0N	0D, 2N, 24B	Very Good
11	5174	2-II	2D, 0N	4D, 2N, 1B	Very Good
12	3748	1	0D, 1N	0D, 2N, 3B	Very Good
13	4827	2-II	2D, 5N	3D, 3N, 33B	Very Good
14	5732	3	1D, 0N	10D, 1N, 4B	Fair
15	5711	2-II	2D, 1N	3D, 2N, 14B	Very Good

Table 2.2

FQ1 DNB List

No.	ID	LOT	Screening	Flight DNB at	Comments
0	17230	LOT4	0D,0N	0D, 7N, 12B	Good
1	17746	LOT4	0D,0N	0D, 1N, 1B	Very Good
2	5635	LOT2-II	1D,1N	2D, 3N, 4B	Very Good
3	3747	LOT1	1D,1N	4D, 3N, 4B	Very Good
4	17756	LOT4	0D,3N	0D, 1N, 7B	Very Good
5	5721	LOT2-I	1D,6N	1D, 5N, 2B	Very Good
6	17285	LOT4	0D,0N	0D, 1N, 0B	Very Good
7	17223	LOT4	0D,0N	6D, 7N, 0B	Fair
8	17257	LOT4	0D,1N	0D, 2N, 2B	Very Good
9	21027	LOT5	1D,0N	1D, 1N, 16B	Very Good
10	3726	LOT1	4D,6N	2D, 2N, 22B	Very Good
11	21143	LOT5	0D,1N	0D, 1N, 20B	Very Good
12	21123	LOT5	0D,0N	0D, 2N, 4B	Very Good
13	21113	LOT5	0D,0N	0D, 2N, 14B	Very Good
14	21121	LOT5	0D,0N	0D, 1N, 1B	Very Good
15	17052	LOT4	1D,4N	1D, 1N, 69B	Very Good

Table 2.3

FQ2 DNB List

No.	ID	LOT	Screening	Flight DNB at	Comments
0	5102	LOT2-II	1D,0N	4D, 2N, 2B	Very Good
1	5688	LOT2-II	2D,0N	2D, 1N, 1B	Very Good
2	5060	LOT2-II	0D,0N	0D, 3N, 3B	Very Good
3	5002	LOT2-II	1D,0N	5D, 3N, 6B	Good
4	5669	LOT2-II	1D,0N	1D, 2N, 3B	Very Good
5	4794	LOT2-II	0D,0N	6D, 2N, 0B	Good
6	4815	LOT2-II	3D,1N	4D, 1N, 1B	Very Good
7	5673	LOT2-II	1D,1N	7D, 4N, 4B	Fair
8	3743	LOT2-II	0D,3N	15D, 1N, 3B	Poor
9	5720	LOT2-II	0D,1N	11D, 3N, 4B	Poor
10	5733	LOT2-I	1D,0N	19D, 1N, 4B	Poor
11	5394	LOT2-I	0D,1N	2D, 1N, 3B	Very Good

12	5690	LOT2-II	0D,0N	0D, 1N, 1B	Very Good
13	5682	LOT2-II	3D,0N	1D, 3N, 5B	Very Good
14	5671	LOT2-II	1D,1N	2D, 2N, 2B	Very Good
15	4997	LOT2-II	0D,0N	3D, 1N, 0B	Very Good

Table 2.4

FQ3 DNB List

No.	ID	LOT	Screening	Flight DNB at	Comments
0	2767	LOT1	0D,0N	1D, 2N, 8B	Very Good
1	3231	LOT1	0D,0N	6D, 2N, 13B	Good
2	4023	LOT1	0D,2N	9D, 2N, 14B	Fair
3	4750	LOT1	0D,0N	6D, 5N, 0B	Fair
4	3972	LOT1	0D,0N	1D, 1N, 0B	Very Good
5	3970	LOT1	1D,1N	7D, 2N, 3B	Good
6	5426	LOT2-I	0D,0N	0D, 1N, 1B	Very Good
7	4777	LOT1	2D,0N	11D, 6N, 3B	Poor
8	5382	LOT2-I	0D,0N	0D, 3N, 1B	Very Good
9	5716	LOT2-I	1D,0N	2D, 1N, 6B	Very Good
10	4055	LOT1	0D,1N	6D, 6N, 16B	Poor
11	4784	LOT1	0D,0N	3D, 1N, 3B	Very Good
12	4711	LOT1	3D,2N	5D, 3N, 19B	Very Good
13	4032	LOT1	0D,0N	3D, 2N, 1B	Very Good
14	4586	LOT1	5D,1N	4D, 3N, 27B	Very Good
15	3269	LOT1	0D,0N	3D, 1N, 25B	Very Good

Table 2.5

Overall, 84% of the modules are of Very Good or Good category. About 8% are of poor category, based on a large number of dead+noisy pixels in the final flight calibration. The number of dead pixels increased mainly due to disabling some pixels because of their repeated noisy performance. In case of the noisy pixels, it is seen that the noise is present just above the LLD (figures), which was set at 15keV in flight calibrations at 10°C. If the threshold were set at a higher value, these pixels would have appeared normal.

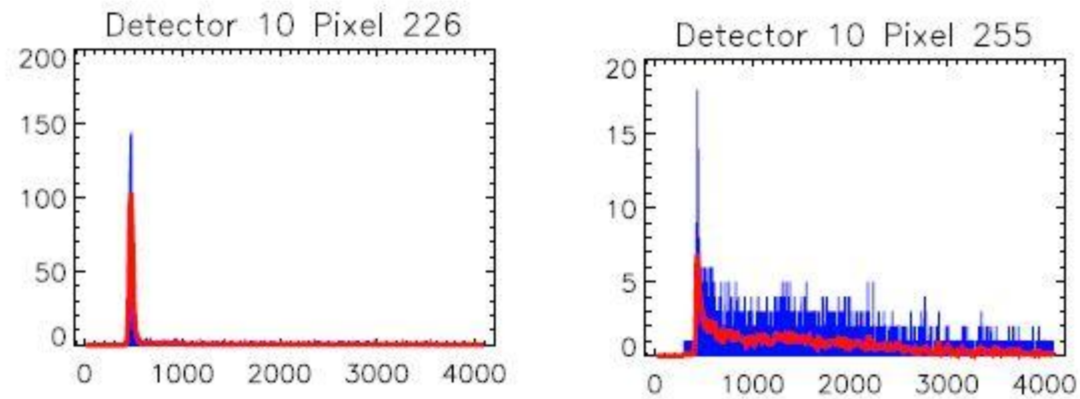

Fig. 2.1: Background-only spectra of two pixels in FQ3- Detector 10 at 10°C ambient temperature. Blue lines show unbinned spectra and the thick red lines show the same spectrum binned in 8 channel bins. Left: Pixel 226 appears noisy when LLD threshold is set at 15 keV, but would appear normal if threshold were 20 keV. Right: Pixel 255 is normal, but shows hints of noise near the LLD. If threshold is reduced further under same operating conditions, this pixel may be flagged as noisy.

Based on these observations, we conclude that there is no significant change in the dead+noisy pixels of all the detectors of all quadrants between selection (VSSC screening) and flight calibrations.

Spectroscopic pixels: Bad pixels are pixels where energy resolution for the 59.54 keV Am line is worse than 12 percent. The screening process for bad pixels was not rigorously documented; extreme outliers were flagged by-eye. Bad pixels in final flight configuration were identified from 4 hour data of all sources (^{241}Am, ^{57}Co, ^{109}Cd and BG) at 10°C (ambient) with 15 keV threshold.

Bad pixels in final calibration are listed in the tables above. Most detectors show < 5 pixels with energy resolution worse than 12% at 60 keV. The number of bad pixels is higher than initial screening; we attribute this to more rigorous test and evaluation procedures employed now.

2.2 X-ray spectroscopic calibration at various temperatures

Calibration data were obtained by the CZTI team by shining various radioactive sources on the quadrant at various temperatures in the range 5-20°C (ambient temperature). Detectors heat up due to power dissipation, and the detector temperature is usually a few degrees higher than ambient. We used these data to test the stability of detectors, identify the best pixels, calculate their gains and offsets, and test the temperature dependence of these properties.

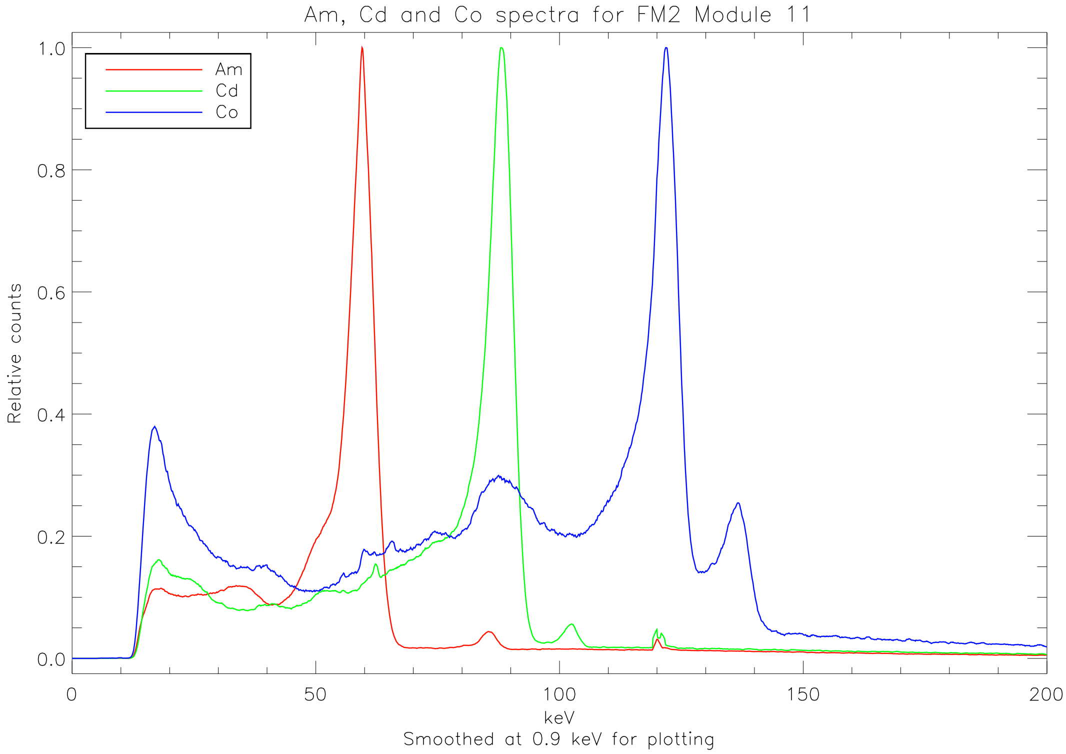

Fig. 2.2

Under the time constraints for laboratory testing, it is not possible to obtain data at all temperatures and all thresholds. Typically, the low energy noise decreases at lower temperatures. We took advantage of this by lowering the threshold values as we cooled the detectors, thus obtaining lower energy data as well. However, not all pixels show a similar performance enhancement at lower temperatures. The operator then picked a tradeoff, which typically involved disabling a few more noisy pixels in order to enable a lower threshold value for the entire detector. This reflects itself as a larger number of noisy pixels at lower temperatures.

We have extensively discussed Dead, Noisy and Bad pixels in the previous section. Another type of pixels, not addressed in the requirements, is flickering pixels. These pixels are stable for most of the time, but occasionally show large noise outbursts (Figure). Visual examination of count rates over several data sets has shown that CZTI detectors have very few flickering pixels. We have flagged these pixels on the basis of manual examination of count rate variations of the pixels. If a pixel is seen to flicker very often, it will potentially be marked as a noisy pixel and disabled in flight.

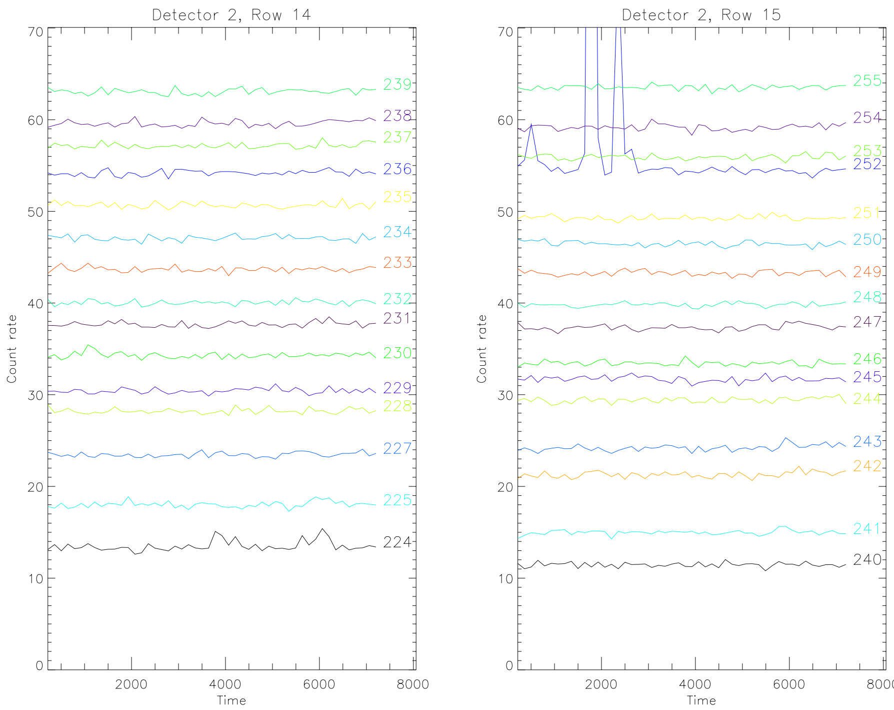

Fig. 2.3: Visual identification of flickering pixels. The plot shows count rate as a function of time for pixels in two rows of FQ2 Detector 2, during two hour integration. The plot for each pixel is vertically offset for clarity. Pixel 252 shows flickering behavior at the start of the dataset.

The following table 2.6 lists the no of frequently occurring flickering pixels in all detectors of all quadrants.

module position	Number of flickering pixels			
	FQ0	FQ1	FQ2	FQ3
0	7	12	0	3
1	0	0	0	3
2	1	0	1	22
3	4	9	1	8
4	0	1	0	1
5	0	11	0	7
6	0	1	0	0
7	0	1	0	0
8	0	3	0	0
9	0	0	1	8
10	4	5	0	21
11	0	0	0	9
12	7	0	0	8
13	6	0	0	11
14	2	0	0	6
15	0	1	0	1

Table 2.6

The number of flickering pixels constitutes about 1% of the total and if they are found to be flickering most of the time, they will be suppressed or ignored during the analysis. Bulk of these flickering pixels (about 60%) are in FQ3 and it can be seen that half of the flickering pixels in this quadrant comes from module numbers 2,3, and 10, classified as Fair or Poor. Hence, the issue of flickering pixels essentially is the tail end of the distribution of noisy pixels and they are small in number and hence can be handled by software.

Energy resolution

X-ray spectra of monochromatic lines in Cadmium Zinc Telluride (CZT) are typically modeled as a Gaussian "photopeak" and a low energy tail created by various charge transport factors (impurities, charge trapping, etc.). Apart from any source features, the spectra also show an excess at low energies (15 keV) which is created by electronic noise and background. This excess is higher at lower energies, and decreases with temperature. The ambient background spectrum in the lab also shows a hump at around 100 keV. With this general nature of the spectrum in mind, let us proceed to the measurement of energy resolution of CZTI using various radioactive sources.

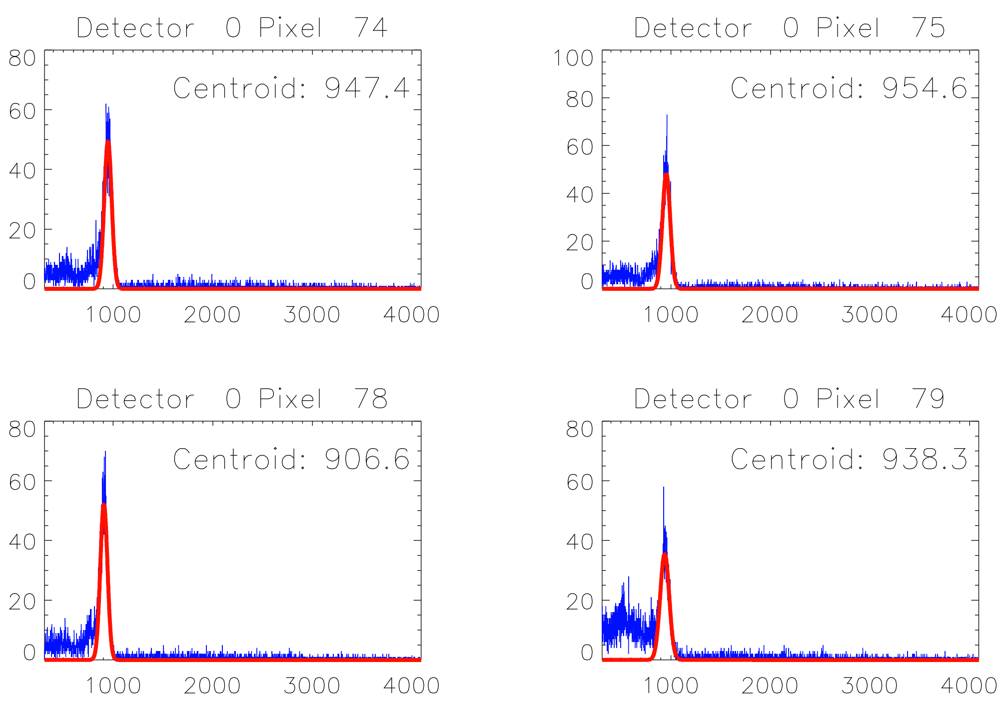

Fig. 2.4: Sample ^{241}Am spectra of a few pixels in FQ2, Detector 0. The X axis is channels, and Y axis is counts per channel as measured in 4hr. integration. Data were acquired at 5∘C with threshold set at 10 keV. A Gaussian fit to the 59.56 keV line is over plotted on the spectra in red. Deviations from the Gaussian are clearly seen on the lower side. Pixel 79 shows a low energy noise component that dominates over the tailing from the line.

We define the energy resolution as the Full Width at Half Maximum (FWHM) of this Gaussian photopeak core. We find the peak channel in the spectrum, and fit a Gaussian function to a region around it (Fig. 2.4). If this fitting region is large, the fit is affected by charge tailing on the lower side and background events on the higher side. On the other hand, we lose out on statistics by selecting too small a fitting region. We experimented with various datasets and determined that the optimal fitting region extends from $-1\sigma'$ to $+2\sigma'$ of the channel with highest counts, where σ' is the approximate Gaussian σ. If the actual line σ obtained from the fit does not agree with the assumed σ', we revise the input parameters and fit again. After our fits converge, we calculate the FWHM as 2.35σ.

Energy calibration

Energy calibration of detectors is carried out using measurements of various radioactive lines from ^{241}Am, ^{57}Co and ^{109}Cd sources. We fit the line locations in channels as described in the previous section. Next, we use the known energies of these lines to fit a straight line mapping channels to energy, correctly accounting for measurement errors. The slope and intercept of this line gives the gain and offset of the detector. The mapping between ADC channels and energy (keV) is given by,

$$Energy = Channels \times Gain + Offset$$

Gains and offsets measured for FQ2 Detector 5 at 15°C are shown in Figure. In most detectors, inter-pixel gain variations are small (< 10%).

The gain and offsets of detectors vary with temperature. This manifests itself as a shift in the peak channel for radioactive spectra (Fig. 2.4). In order to accurately reconstruct the energy of each incident photon, we have to take this temperature variation into account. We have measured the gains and offsets of detectors at various temperatures (Fig. 2.5). While analyzing flight data, appropriate gain and offset values interpolated from these measurements will be used.

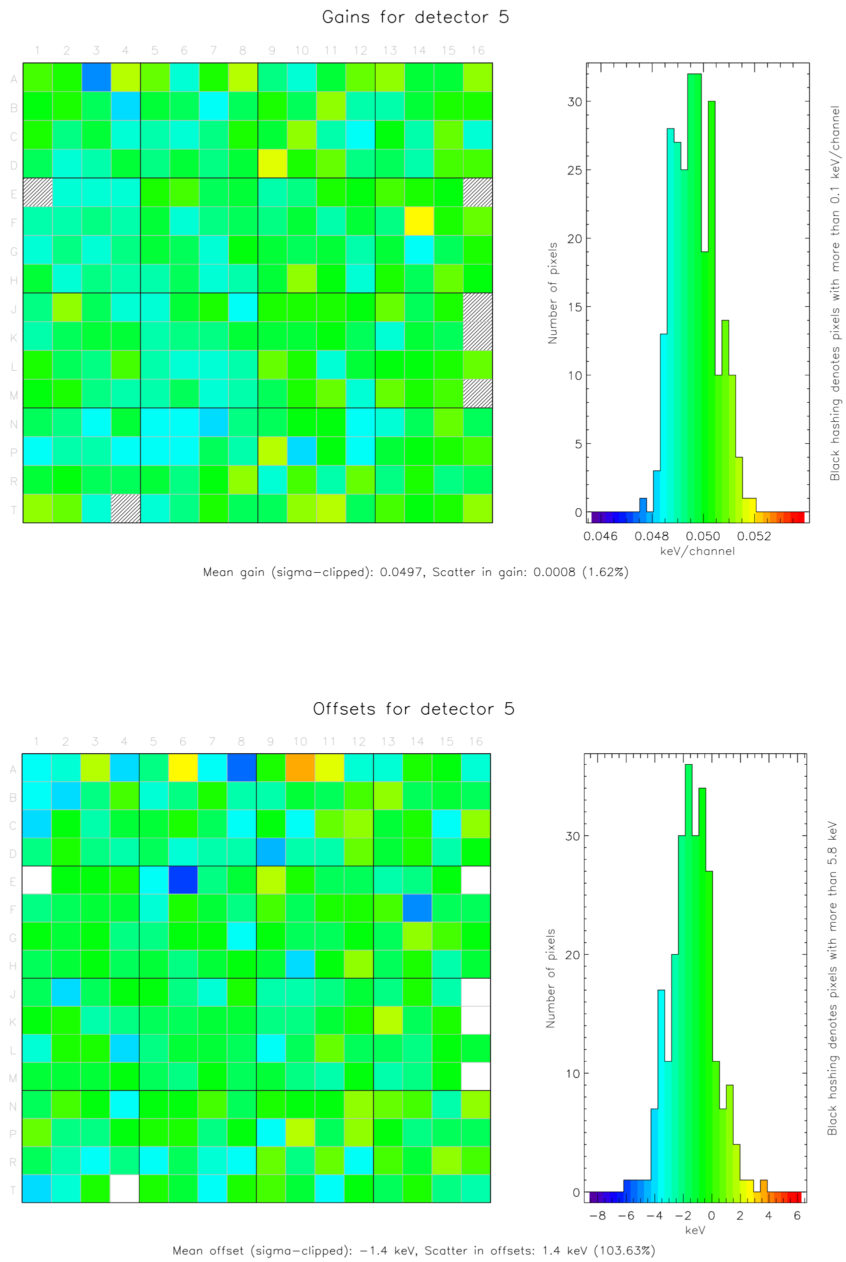

Fig. 2.5: Gain (top panel) and offset (bottom panel) measurement for all pixels in FQ2 Detector 5 at 15◦C. The insets on the right show colour-coded histograms of the gain and offset distributions. Gains and offsets were calculated using the 241Am 60 keV and 57Co 122 keV lines. The gains for all pixels agree to two percent, and the offsets agree to about 1.5 keV.

The energy resolution of detectors also changes with temperature. Fig. 2.6 shows the energy resolution as a function of temperature for Am, Co and Cd lines at 59.5, 122 and 88 keV for FQ2 respectively. It is seen that the resolution does not change drastically with temperature. We show in Fig 2.7 a plot of energy resolution with energy. The measurements at low energies (22 keV and 33 keV) suffer from the blend of energies at theses energies and hence are underestimates. Values above 50 keV agree with the expected relation with square root of energy.

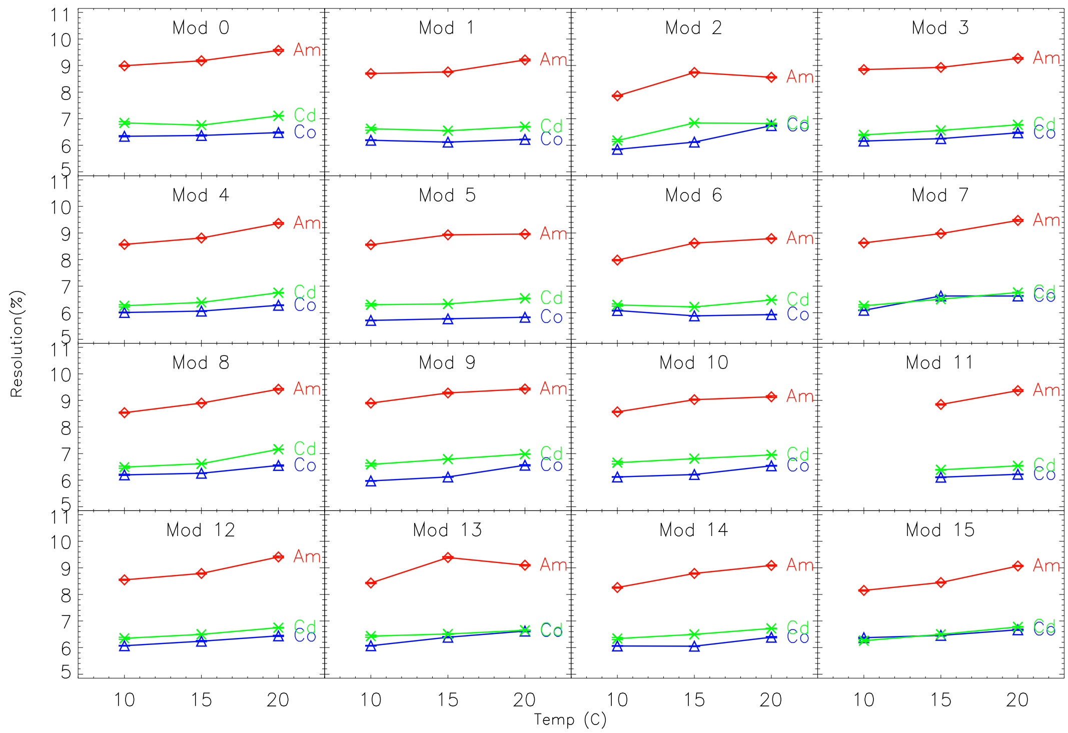

Fig. 2.6

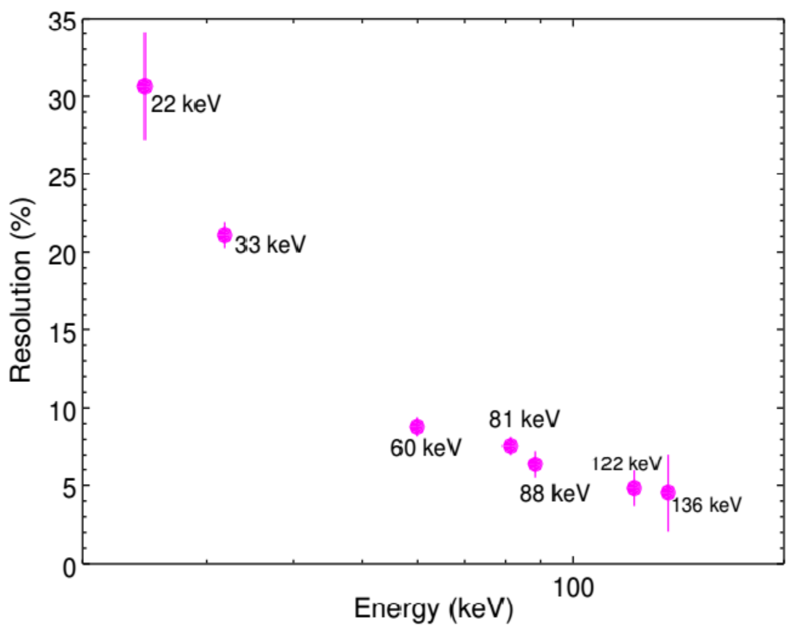

Fig. 2.7 shows the energy resolution of FQ1 module 02, measured at different energies.

2.3 Thresholds Estimation

During the thermovac tests, calibration sources were mounted on each of the quadrants at a height of about 20 cm from the CAM. Though the source counts varied from pixel to pixel and module to module, there was sufficient number of source counts to do a detailed comparison with the earlier results. The following things were established during this calibration:

To measure the thresholds and number of noisy pixels: About 2% of the pixels were dead or permanently disabled. In the room temperature tests, further 3 % (a total of 5%) pixels were disabled and the threshold was kept at 40 keV. The achievable threshold and the number of noisy pixels were carefully studied as a function of temperature during the thermovac. The results are given in the following tables 2.7-2.9. It is found that in the operating temperature (0 to 15 C), a majority of the modules could be operated at a threshold of 10 keV and the number of noisy pixels is less than 3%.

Quadrant	**Temperature**	**-5°C**	**0°C**	**5°C**	**10°C**	**15°C**	**20°C**	**25°C**
	Module	**Threshold**	**Threshold**	**Threshold**	**Threshold**	**Threshold**	**Threshold**	**Threshold**
Quadrant 0	**0**	10	18	18	18	18	30	40
	1	10	10	10	10	10	20	40
	2	10	10	10	10	10	35	40
	3	15	15	15	15	15	30	40
	4	18	18	18	18	18	30	40
	5	10	10	10	10	10	20	40
	6	10	10	10	10	10	20	40
	7	15	15	15	15	15	30	40
	8	10	10	10	10	10	20	40
	9	10	10	10	10	28	30	40
	10	14	14	14	14	14	30	40
	11	10	10	10	10	10	20	40
	12	10	10	10	10	10	20	40
	13	10	10	10	10	20	30	40
	14	10	10	10	10	22	30	40
	15	14	14	14	14	25	30	40
Quadrant 1	**0**	10	10	10	10	10	30	50
	1	10	10	10	10	10	20	40
	2	10	10	10	10	10	20	40
	3	15	15	15	15	15	30	40
	4	10	10	10	10	10	20	40
	5	12	12	12	14	25	30	40

	6	10	10	10	10	10	20	40
	7	15	15	15	17	17	30	40
	8	10	10	10	17	22	30	40
	9	10	10	10	10	10	20	40
	10	10	10	10	10	28	50	40
	11	10	10	14	14	14	30	40
	12	10	10	10	10	10	20	40
	13	10	10	10	10	10	20	40
	14	10	10	10	10	10	20	40
	15	20	20	20	20	20	30	40
Quadrant 2	**0**	10	10	10	14	32	40	50
	1	10	10	10	10	10	20	40
	2	14	14	14	14	25	30	40
	3	10	14	18	18	18	30	40
	4	10	10	10	10	10	20	40
	5	14	14	14	14	14	30	40
	6	10	10	10	10	10	30	40
	7	15	15	15	15	20	20	40
	8	10	10	10	10	10	30	40
	9	10	10	10	10	10	20	40
	10	10	10	10	10	22	40	40
	11	10	10	10	10	10	20	40
	12	18	18	18	20	20	30	50
	13	10	10	10	10	10	20	40
	14	10	10	10	10	10	20	40
	15	10	12	12	12	12	30	40
Quadrant 3	**0**	10	10	10	10	20	30	50
	1	13	20	20	20	35	40	70
	2	14	18	18	18	32	40	70
	3	25	25	25	25	40	30	40
	4	10	12	12	12	12	30	40
	5	14	14	18	18	18	30	40
	6	12	12	12	12	60	70	40
	7	20	20	20	25	25	30	40
	8	14	18	18	25	40	50	40
	9	14	14	16	16	20	30	40
	10	14	14	14	16	20	40	40
	11	12	18	18	18	18	30	70
	12	12	12	12	14	20	40	40
	13	15	15	15	15	20	40	70
	14	10	10	10	10	40	40	70
	15	16	16	16	16	16	40	70

Table 2.7

Temperature (°C)	Threshold				
	10 keV	**11-15 keV**	**16-20 keV**	**21-30 keV**	**>30 keV**
-5	38 (59%)	20 (31%)	5 (8%)	1 (2%)	--
0	34 (53%)	19 (30%)	10 (15%)	1(2%)	--
5	33 (52%)	17 (26%)	13 (20%)	1(2%)	--
10	31 (48%)	16 (25%)	14 (22%)	3 (5%)	--
15	24 (38%)	8 (12%)	16 (25%)	9 (14%)	7 (10%)
20	--	--	21 (33%)	30 (47%)	13 (20%)
25	--	--	--	--	64 (100%)

Table 2.8 Achieved Threshold as function of Temperature

Temperature	No. of Disabled Pixels						
	-5°C	**0°C**	**5°C**	**10°C**	**15°C**	**20°C**	**25°C**
Quadrant 0	100	100	102	111	131	139	152
Quadrant 1	76	78	81	93	110	126	142
Quadrant 2	129	136	143	162	176	185	199
Quadrant 3	148	152	158	170	183	198	224
Total No. of Disabled Pixels	453 (3%)	466 (3%)	484 (3%)	536 (3%)	600 (4%)	648 (4%)	717 (4%)

Table 2.9 Number of pixels disabled

The table 2.10 and 2.11 below gives the list of the number of frequently noisy, permanently dead, spectroscopically bad, flickering pixels along with expected and obtained thresholds for all 64 modules of 4 quadrants.

Quadrant	Detector	No of Frequently Noisy Pixels	No of Permanently Dead Pixels	No of Spectroscopically Bad Pixels	No of Flickering Pixels	Threshold (10C)	
						Expected	Obtained
0	0	2	1	12	7	10	12.95
	1	1	0	3	0	10	13.363
	2	1	2	0	1	10	14.17
	3	6	3	2	4	10	12.84
	4	3	7	5	0	10	12.287
	5	2	0	1	0	10	12.103
	6	4	2	4	0	10	13.113
	7	1	7	1	0	10	12.99
	8	1	5	12	0	10	11.917
	9	2	6	99	0	10	11.953
	10	2	0	24	4	10	12.437
	11	2	4	1	0	10	11.233
	12	2	0	3	7	10	13.04
	13	3	3	33	6	10	11.687
	14	1	1	4	2	10	13.867
	15	2	3	14	0	10	12.61
1	0	7	0	12	12	10	13.57
	1	1	0	1	0	10	11.267
	2	3	2	4	0	10	13.55
	3	3	4	4	9	14	18.607
	4	1	0	7	1	10	14.073
	5	5	1	2	11	10	10.673
	6	1	6	0	1	10	12.07
	7	7	0	0	1	14	18.48
	8	2	1	2	3	10	13.613
	9	1	2	16	0	10	14.86
	10	2	0	22	5	10	12.36
	11	1	0	20	0	10	14.74
	12	2	0	4	0	10	14.193
	13	2	0	14	0	10	15.153
	14	1	0	1	0	10	13.13
	15	1	1	69	1	10	11.923

Table 2.10

Quadrant	Detector	No of Frequently Noisy Pixels	No of Permanently Dead Pixels	No of Spectroscopically Bad Pixels	No of Flickering Pixels	Threshold (10C)	
						Expected	Obtained
2	0	2	4	2	0	10	13.093
	1	1	2	1	0	10	13.947
	2	3	0	3	1	10	11.97
	3	3	5	6	1	16	19.59
	4	2	1	3	0	10	11.803
	5	2	6	0	0	10	11.613
	6	1	4	1	0	10	12.943
	7	4	7	4	0	14	17.96
	8	1	15	3	0	10	11.98
	9	3	11	4	1	10	12.503
	10	1	19	4	0	10	11.993
	11	1	2	3	0	10	12.463
	12	1	0	1	0	10	12.603
	13	3	1	5	0	10	13.32
	14	2	2	2	0	10	12.58
	15	1	3	0	0	10	13.167
3	0	2	1	8	3	10	13.533
	1	2	6	13	3	10	12.47
	2	2	9	14	21	10	11.583
	3	5	6	0	8	12	14.75
	4	1	1	0	1	10	14.347
	5	2	7	3	7	10	11.793
	6	1	0	1	0	10	13.363
	7	6	11	3	0	16	20.73
	8	3	0	1	0	10	12.76
	9	1	2	6	8	10	12.853
	10	6	6	16	21	10	11.01
	11	1	3	3	9	10	13.123
	12	3	5	19	8	10	10.537
	13	2	3	1	11	10	11.02
	14	3	4	27	6	10	12.677
	15	1	3	25	1	10	14.16

Table 2.11

2.4 CAM Calibration

The solid-state CZT detector has a very good combination of energy resolution and detection efficiency and is best suited with CAM pattern in terms of required spatial resolution. CAM is used as the coding device for imaging in the CZTI detector. The shadow patterns of the CAM and the coding techniques can be tested to check the efficiency of the coding device to the given radiation and to background. This is done by shining strong sources at known positions. A detailed report on the QM testing is given in Annexure I.

It is concluded that source localization should be possible within a few arc-minutes.

2.4.1. Field of View of the CZT imager

The Field of View (FoV) of the CZT imager is energy dependent due to greater transparency of the collimator material at higher photon energies. The angular response pattern contains a central core of ~6 deg radius which is common to all energies, and represents the view through the top coded mask surface. Transmission through the collimator slats and side walls contribute wings to the response pattern, the relative strength of which rises with increasing energy. The FoV may therefore be quantified as the amount of solid angle the response pattern covers at a given fraction of the peak on-axis response. It is to be noted that not all of this coverage may be contiguous. We compute the FoV by summing the solid angle of all parts of the effective area distribution that rise above a specified fraction of the on-axis value. The resulting estimates, for different photon energies, are presented in the fig. 2.8 below. The FoV evaluated at 50%, 20% and 10% of the peak response at each energy is shown. The FoV increases monotonically with photon energy, apart from a bump near 67 keV due to Tantalum K escape.

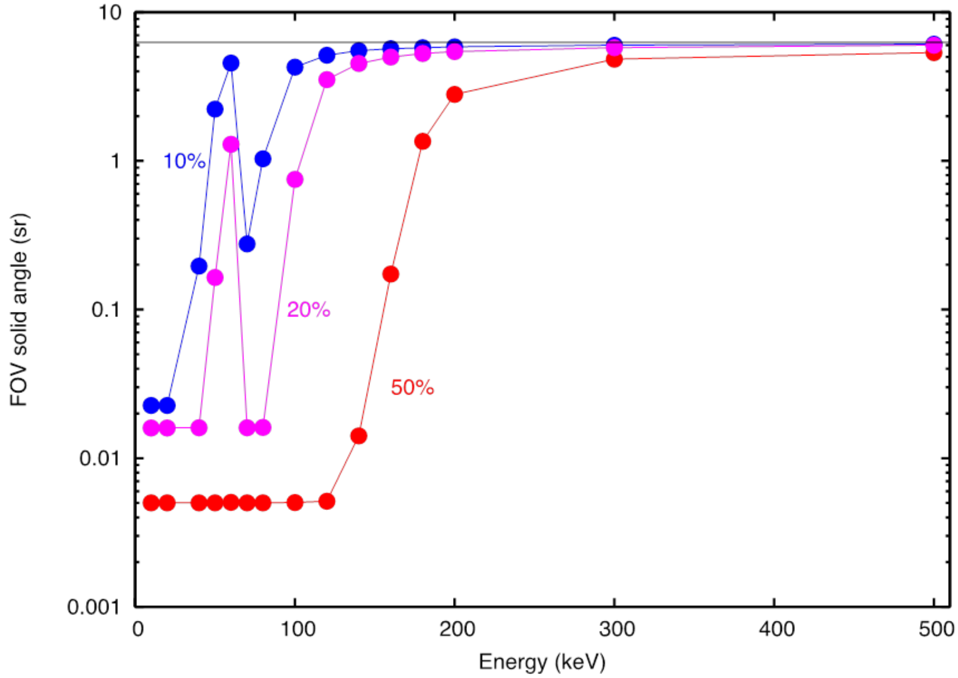

Fig. 2.8

The figure 2.9 below shows, the effective area as a function of energy has been calculated for various opening angles.

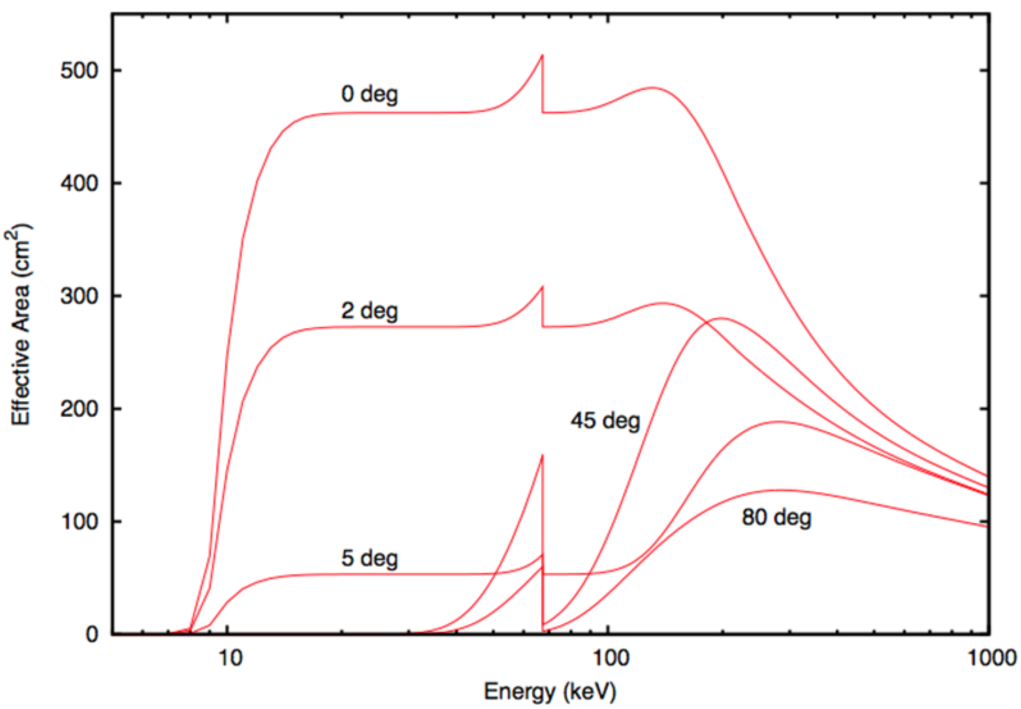

Fig. 2.9

2.5 Alpha-tagging in CZTI

A 10 mm^3CsI(Tl) crystal, embedded with a radioactive source ^{241}Am and viewed by a photodiode of 10 mm^2 area, is placed beside the CZT detector. With each disintegration of the 60 keV photon from this source, an Alpha particle (energy about 5 MeV) is also emitted. The alpha particle is absorbed in the small CsI(Tl) detector, whereas the 60 keV X-rays will escape from this detector and, in most cases, will interact with the CZT detector. The alpha particle produces a light pulse in the CsI(Tl) crystal, which in turn is converted into an electrical pulse at the output of the photo-diode. Any output in the CZT detector coincident with the pulse output from the CsI(Tl) detector is deemed to be originating from a 60 keV photon. This method is used to calibrate the energy response of the CZT detector for its energy response.

The basic design principles are discussed in Rao et al. (2010, NIMPA. 616, 55) and it was estimated that, for an alpha source strength of 1000/s, about 20 – 30 60 keV X-rays should be emerging from the alpha module. The time co-incidence was done digitally and this aspect is rigorously tested in the QM and one FM detector. A detailed report is given in Annexure II. The tunable parameters were examined carefully, and it was found that the alpha-tagged information can indeed be extracted from the data. However, the final flight configuration is such that the final alpha count rate is as low as ~1 count/s, necessitating a large integration time, grouping of pixels, and use of background lines for the onboard calibration.

2.6 Veto calibration

The veto detector is a 20 mm thick CsI(Tl) scintillation, of size 167 mm × 167 mm, viewed by two one inch Photo-multiplier tubes (PMT) positioned at two sides of the crystal. Minimum detection sensitivity is 50 keV for incident photons. The main purpose of this detector is to recognize background X-ray/ gamma-ray radiation (above 100 keV) and tag the main X-ray events (in the CZT detector) with the information that the X-rays are accompanied by a background X-ray/ gamma-ray. The energy resolution of this detector is not significant. These detectors are procured from Scionix Holland, the same suppliers who have provided the RT-2 phoswich detectors and the ACS system for Chandrayaan-I. For the CZT-Imager, it was decided to carry out a minimum screening of 10 cycles of thermovac cycling (passive). The temperature range was -20 to +50° C.

The HV parts were potted with HV 93-500 and the screening and thermovac tests were done after the potting. It was found that the gain uniformity over the area is correct to 10%.

After the FM assemblies, the amplifier gain was adjusted so that the upper level corresponds to about 500 – 600 keV. The LLD, however, can be changed by command. The test result for one of the FM quadrants is shown in the Figure 2.10. The spectra, from the top, are for Am (60 keV), Cd (88 keV), Co (122 keV) and Ba (356 keV) respectively. Gaussian fit to the Ba data is also shown in the same figure. The linearity plot is shown in the figure 2.11.

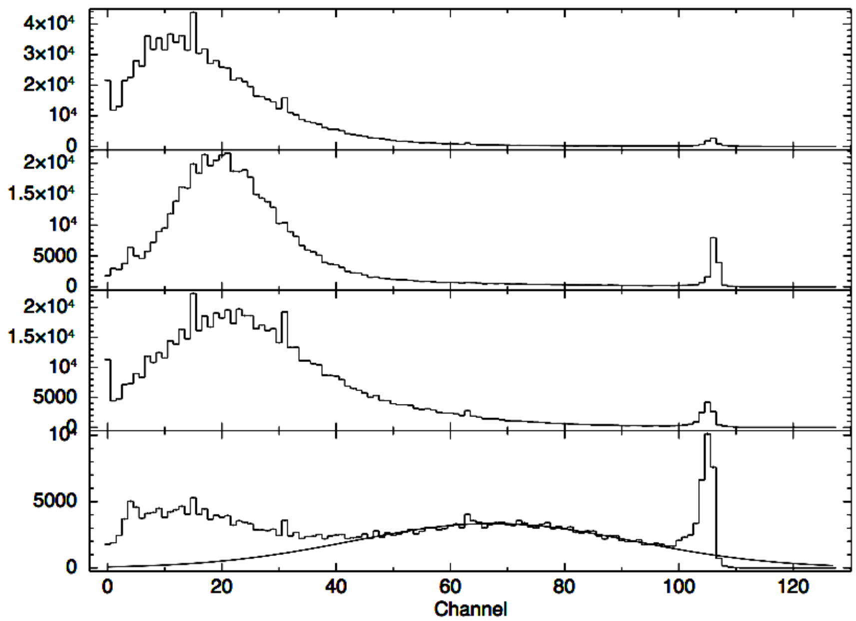

Fig. 2.10

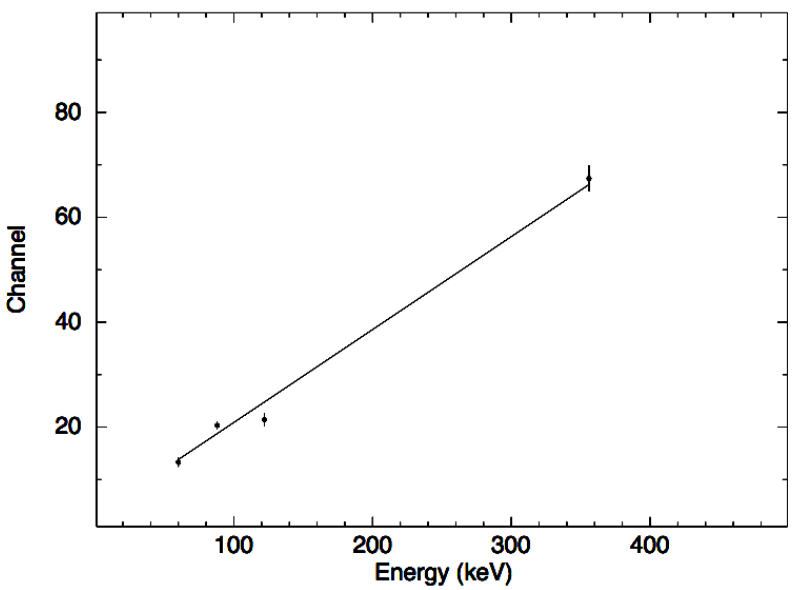

Fig. 2.11

The Veto detectors were re-calibrated before the final assembly and the gain-offset results are given below.

Four sources, namely ^{241}Am, ^{109}Cd, ^{57}Co and ^{133}Ba were shined on the veto detectors from behind the CZTI payload.

Using the spectral fitting, we obtain peak position for each energy for each quadrant as follows:

Energy (keV)	**FQ0**	**FQ1**	**FQ2**	**FQ3**
59.54	21.92±0.06	18.57±0.1	17.49±0.92	15.86±1.06
88.04	24.80±0.19	22.85±0.26	21.49±0.62	23.73±0.1
122.06	28.85±0.2	26.97±0.21	25.99±0.47	28.03±0.2
356.02	54.46±0.74	74.18±1.79	69.51±1.15	69.78±0.49

Table 2.12

The energies are fitted to the observed peak positions to get gain and offset for each quadrant. The energy v/s channel plot is shown for FQ1 in fig. 2.22. Table 2.13 lists the calculated gains and offsets for all quadrants. The relation between energy and channel is:

$$\text{Energy} = \text{Gain} \times \text{Channel} + \text{Offset}$$

Quadrant	**Gain**	**Offset**
FQ0	7.938±0.173	-112.09±4.30
FQ1	5.594±0.122	-41.239±2.823
FQ2	5.943±0.130	-41.682±2.823
FQ3	5.222±0.115	-26.528±2.521

Table 2.13

Background Rejection:

The Veto detector is designed to capture the forward scattered gamma-rays. In the laboratory, it is quite difficult to reproduce this result because any gamma-ray source, like ^{133}Ba, has a low energy line with much higher probability of interaction. It was, however, possible to capture the Compton scattered events by restricting the energy range of CZT detectors to a narrow window of 40 – 70 keV (to detect only the Compton scattered events). When plotted against the coincidence window time, at > 12 micro-seconds, the data shows the expected coincidence events (about 10% of the total events).

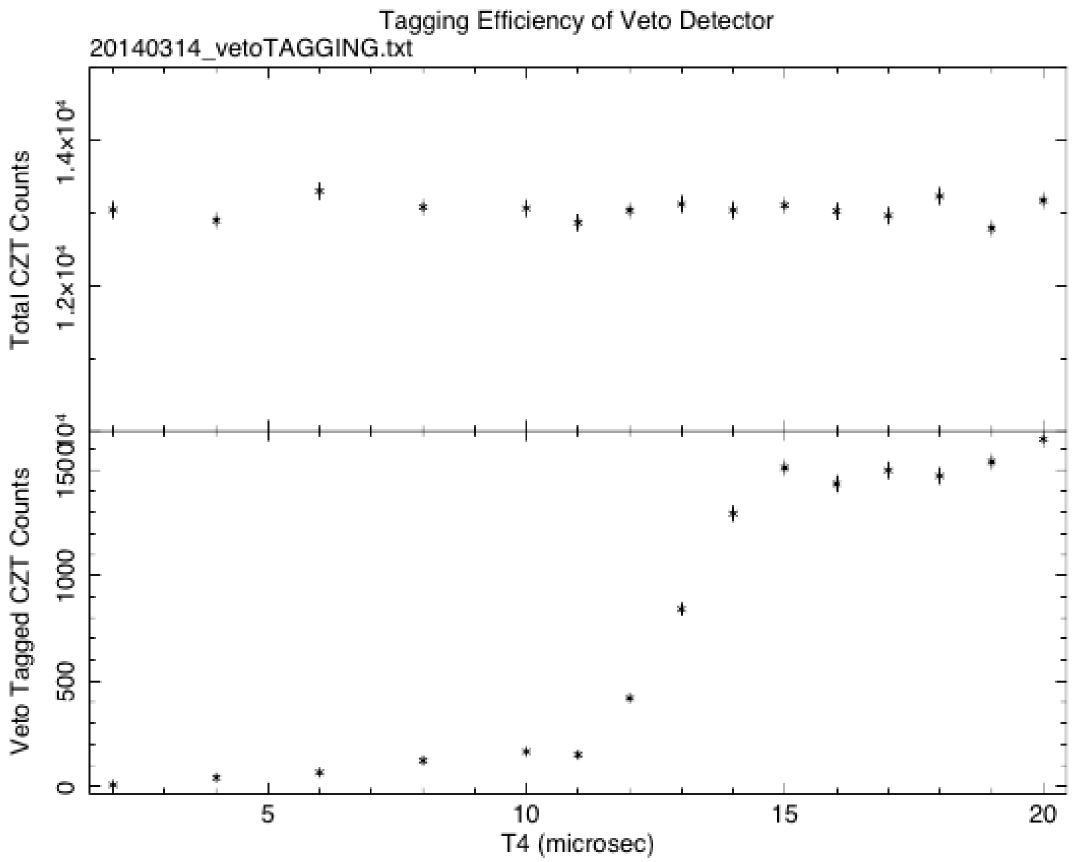

Fig. 2.12 Tagging efficiency of veto detector

2.7 Time tagging, cross talk and polarization capability of CZTI

A rigorous test was carried out for the time tagging of the events and their accuracy. Based on the observation of the regularity of the time for the LAXPC pulse (generated from the Ground Check system) it is concluded that the onboard time can be accurate to 20 µsec, with respect to the calibration pulse.

A rigorous test for cross-talk showed some cross talk, but at a level compatible with the known processes (see section 2.7.1).

The accurate time-tagging has indeed resulted in a bonus of making CZTI sensitive to polarization. This is discussed in section 2.7.2.

2.7.1 Quantification of Crosstalk between pixels of CZT Imager of ASTROSAT

Crosstalk between the pixels may contribute to the spectroscopic background. Further, in polarization measurements, crosstalk may mimic the double pixel events jeopardizing the polarization signature hidden in the incident beam. It may be due to various reasons, e.g. Compton scattering of photons, escape photons corresponding to photoelectric absorption, electronic noise and charge sharing between two pixels and can be quantified by estimating the fraction of double pixel events in two separate pixels. All these processes depend on the incident energy, position of interaction and energy threshold set in CZTI. Therefore, it is possible to quantify the contribution from each of the processes in overall crosstalk by shining the pixels by different sources at different positions with varying energy thresholds. Here we describe the experiment set up and procedure in detail and the results obtained from the analysis.

Experiment Set up

The experiment set up is shown in Figure 2.13. To illuminate the pixels at different positions with an accuracy of a few um, a micrometer system is used which can move both horizontally and vertically to adjust the position of source. The pixels were shined by source through a narrow slit of 0.2 mm in one direction and 20 mm in the perpendicular direction in a lead plate

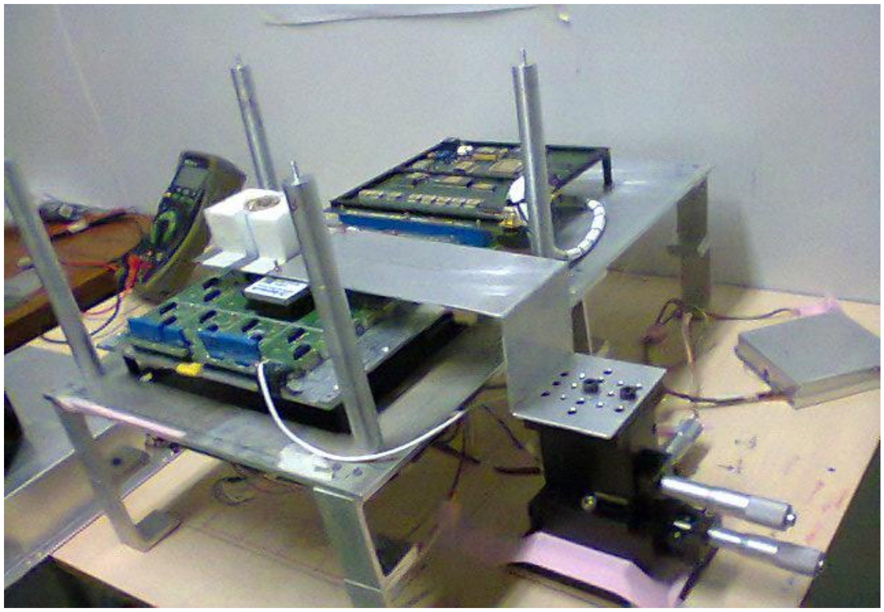

Fig. 2.13 Experiment set up for Crosstalk experiment. The pixels were illuminated by source through a narrow slit to localize the pixel position.

of dimension 60 mm × 60 mm with thickness 3 mm which was kept on the movable arm of the micrometer system. Special care was taken so that the slit is aligned parallel to the pixel edges. The distance between the detector surface and the slit is kept very small (3 mm) so that the beam does not diverge across the boundaries of the pixels. In this way, for a particular position of the source-slit system, a narrow strip (~ 0.2 mm) of eight pixels (along the slit length) is illuminated simultaneously. By moving the micrometer system in horizontal direction (perpendicular to the slit length) at small steps, various positions of the group of eight vertical pixels can be illuminated.

Experiment Procedure

As mentioned earlier, all the processes contributing to the overall crosstalk depend on the energy of photons, position of interaction and energy thresholds set in the detector. We used two X-ray sources, ^{241}Am and ^{57}Co having line energies of 59.5 keV and 122 keV respectively. First, the position was set by looking at the pixel image in labview. For a particular position, the narrow strip of pixels was illuminated first by ^{241}Am and then by ^{57}Co. The same procedure was repeated for other positions by moving the micrometer system in the horizontal direction. In this way, total 13 data sets were taken across 2 pixels, i.e. approximately 6 data sets across the surface of one pixel. The exposure time for each measurement was about 600 seconds. For ^{241}Am, the experiment was repeated for two different thresholds - 25 keV and 35 keV and for ^{57}Co, data at three different thresholds were taken - 25 keV, 35 keV and 50 keV.

Possibility of different kinds of crosstalk for ^{241}Am and ^{57}Co is given in Table 2.14 and Table 2.15 respectively at different energy thresholds set in CZTI during the experiment.

Table 2.14 Truth table for contribution of different processes to Crosstalk for ^{241}Am at various energy thresholds in CZTI.

Energy Threshold in CZTI	**CP**	**ES**	**EN**	**CS**
25 keV	NO	YES	YES	YES
35 keV	NO	NO	YES	YES

Table 2.14

Table 2.15 Truth table for contribution of different processes to Crosstalk for ^{57}Co at various energy thresholds in CZTI.

Energy Threshold in CZTI	**CP**	**ES**	**EN**	**CS**
25 keV	YES	YES	YES	YES
35 keV	YES	NO	YES	YES
50 keV	NO	NO	YES	YES

Table 2.15

where CP, ES, EN and CS stand for Compton scattering, Escape photons, Electronic noise and Charge sharing respectively. Since energy of escape photons from Tellurium is around 31 keV, possibility of crosstalk due to escape is zero when threshold is set at 35 keV or more. Again, Compton scattering of 60 keV incident photons from ^{241}Am deposits very low energy far less than the detection limit. However, for ^{57}Co, crosstalk due to Compton scattering is still possible if the threshold < 50 keV. Detection of Compton scattered photons or escape photons in the neighboring pixel will also depend on the position of interaction in the primary pixel, for example, if the interaction takes place near the boundary, possibility of crosstalk due to Compton scattering and escape will be higher. Similar is the case for charge sharing which is expected to be higher at the pixel boundaries whereas zero in the midway region. On the other hand, electronic noise is a random phenomenon and is expected to be independent of photon energies, and pixel position. Therefore, with proper modeling, it is possible to estimate the contribution of all these processes in the overall crosstalk.

Data Analysis and Results

Here we present the results obtained from the data. First, the illuminated column of pixels was found out for different positions. Two columns with approximately 8-9 pixels in each were illuminated. Two adjacent pixels (pixel number - 133 and 117) from two illuminated columns were selected and total count rate was estimated for these two pixels and their neighboring and next-neighboring pixels individually. In this way, count rate was estimated for 6 different pixels (pixel number - 165, 149, 133, 117, 101, and 85) at different source positions.

Figure 2.14 shows the count rate for ^{241}Am as a function of source-slit position for those six pixels.

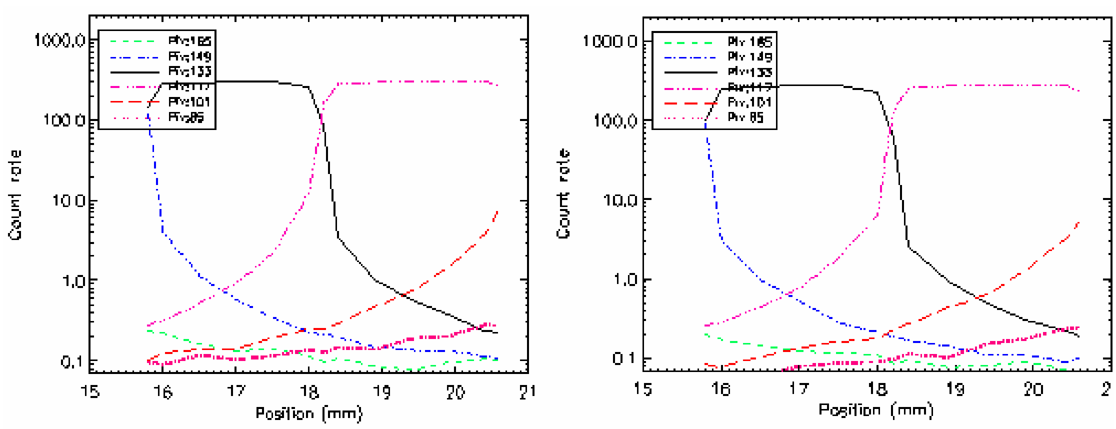

Fig.2.14 Count Rate for 241Am as a function of source-slit position. Different pixels are denoted by different colors and line styles. Left and right plot refer to 25 keV and 35 keV energy thresholds in CZTI.

We see that count rates are quite distinct for the illuminated pixels, neighboring pixels and next-neighboring pixels. The variation in count rate with interaction position as shown in figure is as expected. A similar plot is shown in figure 3 for ^{57}Co. The variation of counts with position for a pixel and its next neighbor shows an expected behavior for the source size of 0.2 mm and it is found that the dead layer in between pixels is very low and can be neglected. Further, the count rates in the next-to-next pixels (which is the sum total of contribution of different processes including electronics crosstalk) is less than 0.01% (for ^{241}Am). Hence we can conclude that inter-pixel dead layer and undesired cross talks are of negligible proportions.

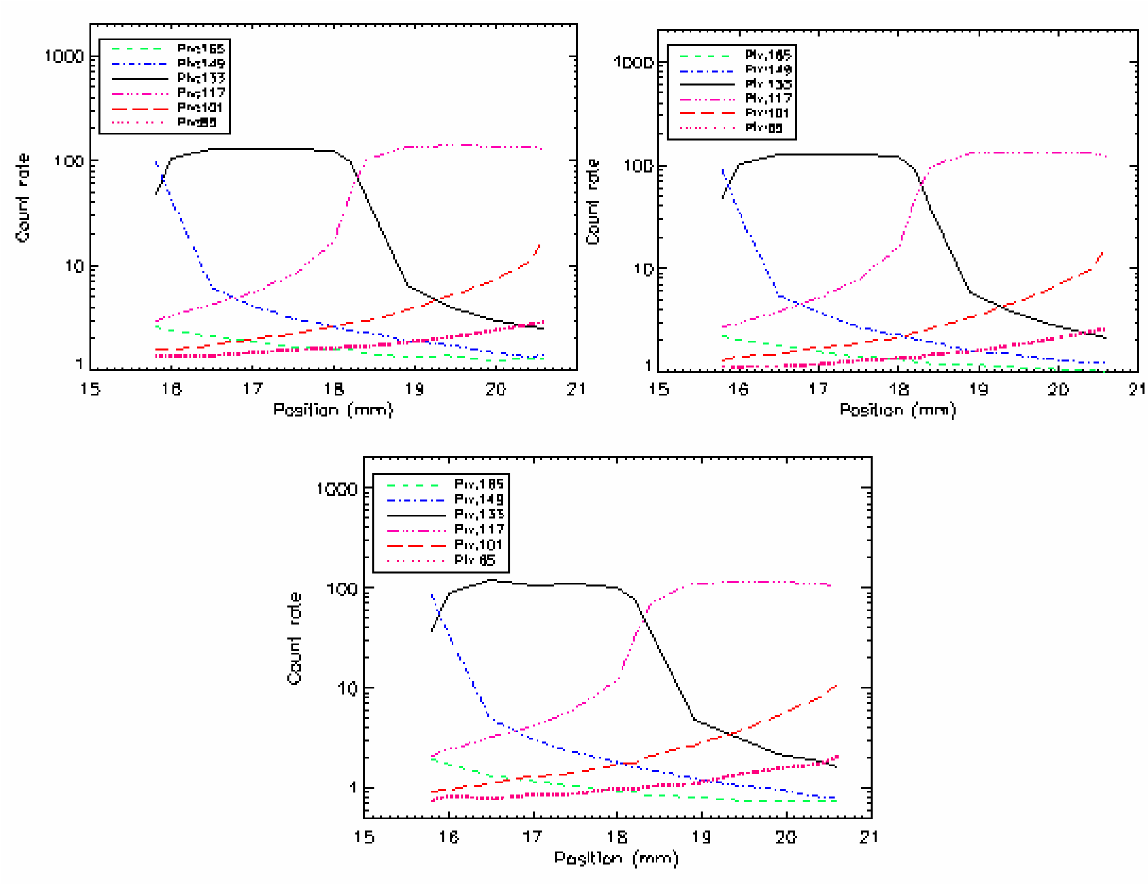

Fig.2.15 Count rate for ^{57}Co as a function of source-slit position. Top left, top right and bottom plot refer to 25 keV, 35 keV and 50 keV energy thresholds in CZTI.

2.7.2 Hard X-ray Polarization measurements with CZTI

Multi-pixel capability of CZTI detectors

The detector plane of CZTI is composed of 64 CZT detector modules. The detectors are procured from Orbotech Medical Solutions. Each detector is 4 cm × 4 cm in dimension and thickness is 5 mm and is further pixilated as an array of 16 × 16 pixels of dimension 2.5 mm × 2.5 mm. Such a pixilated detector can in principle be used for measuring the polarization of the incident X-ray photons based on the principle of Compton scattering by detecting the Compton scattering event in one pixel and the scattered photon in another pixel. However this requires the capability of recording two simultaneous events in different pixels.

In order to verify multi-pixel capability of CZTI detectors, we conducted an experiment in which one CZTI detector was illuminated with a partially polarized beam of energy ~100 keV. The experiment setup is shown in Figure 2.16.

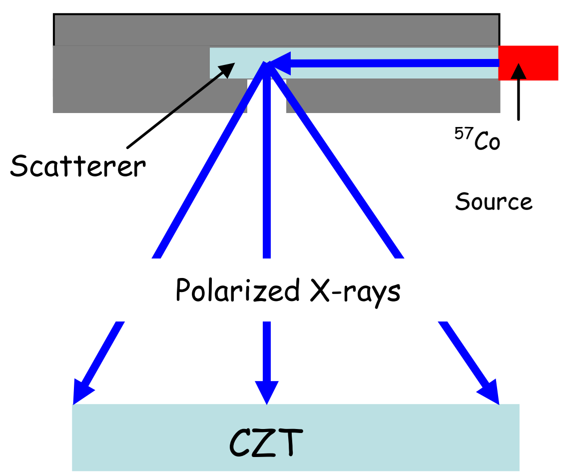

Figure 2.16: Schematic Diagram of the experiment setup to verify the multi-pixel capability of the CZTI detectors. The 122 keV photons are scattered by a plastic scatter at 90° where the CZTI detector is kept.

Polarized beam of 100 keV photons was produced by Compton scattering of 122 keV line of ^{57}Co from a plastic scatterer constraining the angle of scattering at 90°. This scatterer placed in front of ^{57}Co is 6 cm in length. Both the plastic scatterer and source are kept inside a thick lead cylinder (thickness 2 cm) with a narrow slit of dimension 5 cm × 5 mm. The CZTI detector was kept at an angle 90° with respect to the axis of cylinder as shown in Figure 2.15. Alignment of the slit and the CZTI detector was carefully done from the pixel image of the detector. Figure

2.17 shows the results the histogram of time interval, ΔT, between two successive events recorded during this experiment.

Since, radioactivity is a random phenomenon, time interval between two successive independent events recorded in CZTI detector can be modeled by Poisson's statistics. It can be seen that the ΔT distribution agrees perfectly with the expected Poisson distribution for all intervals greater than 40 μs. However, for ΔT less than 40 μs, there is a clear excess of events than expected from the Poisson distribution.

Figure 2.18 shows the spectrum of each pixel from these double pixel events after applying two filtering criteria expected to be satisfied by true Compton scattering events –

1) Two events must be in adjacent pixels and

2) The ratio of energy deposition in two pixels should be greater than 2.

Since the events in two pixels are simultaneous, it is not possible to identify the pixel in which the actual scattering event occurred and the pixel which detected the scattered photon. Therefore the spectra of both pixels look similar.

However, the well separated peaks show that both the energy deposition due the scattering as well as due to the detection of scattered photon can be distinguished as expected.

This experiment clearly demonstrates that the CZTI detectors have the capability of detecting the simultaneous events occurring in multiple pixels and thus CZTI will have the capability of measuring polarization of the incident X-rays by detecting two simultaneous events, first event of actual Compton scattering of the incident photon and the subsequent detection of the scattered photon in a different pixel.

Since only those Compton scattering events which deposit energy greater than the threshold can be detected and the lower energy threshold of the CZTI is likely to be 15 – 20 keV, this sets the lower energy limit for polarization measurements to be ~100 keV. The upper energy limit is set by the saturation limit of the ASIC which is around 250 keV. Thus CZTI is likely to have polarization measurement capability in the energy range of 100 – 250 keV.

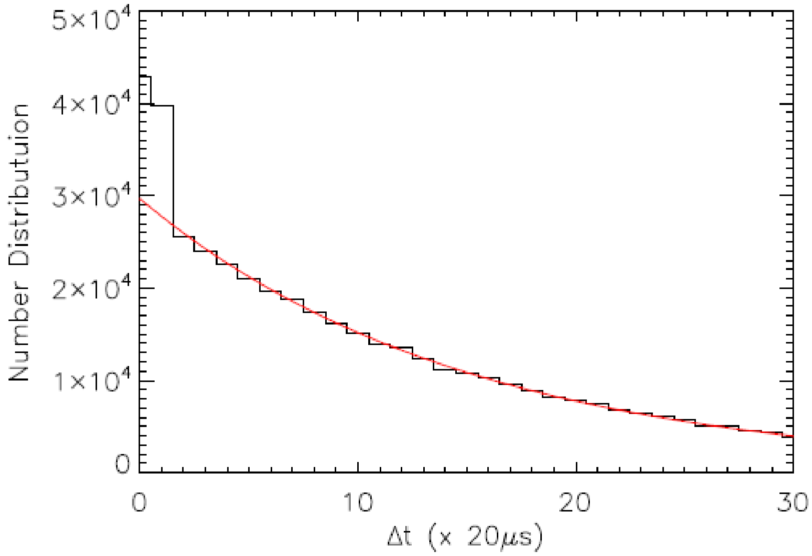

*Figure 2.17**:** Distribution of time intervals of all successive events recorded in CZTI module. The events beyond 40 μs time interval have been fit with a Poisson's function shown by solid red line. There is a clear excess of events with time interval less than 40 μs indicating the detection of the Compton scattering events.*

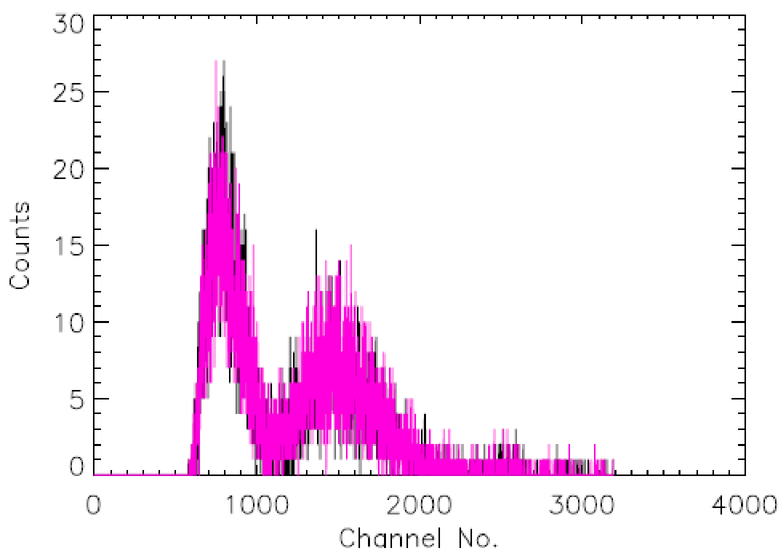

*Figure 2.18**:** Spectra of the individual pixels of the double pixel events satisfying filtering criteria of adjacent pixels and ratio of energy deposited to be >2. The lower energy peak corresponds to the Compton scattering and the higher energy peak corresponds to the scattered photon.*

Geant4 simulations and polarimetric background:

In order to determine whether the CZTI will have meaningful sensitivity for the polarization measurements of X-rays from astrophysical sources, it is necessary to know the modulation factor, polarimetric efficiency and the polarimetric background for the CZTI. We estimated the modulation factor and the polarimetric efficiency with the help of Geant4 simulations. We also calculated polarimetric background which includes both the chance coincidence rate as well as the Compton scattering of the cosmic diffuse X-ray background. We found that the Compton scattering of the cosmic diffuse X-ray background is the predominant component of the polarimetric background, mainly because the polarimetric energy range of CZTI is beyond the primary spectroscopic energy range and hence the mask, collimators and other support structure become partially transparent in the polarimetric energy range. Detailed results of the Geant4 simulations and the calculation of the polarimetric background are provided in the Appendix.

One important result from the Geant4 simulations is that the polarimetric sensitivity of CZTI will depend on the relative angle of polarization direction of the incident X-rays and the instrument axis. For most of the astrophysical sources, the polarization direction, if they have measurable polarization, is not expected to be known a priory. However, once there is some indication of thepresence of polarization for any source, this angle dependent sensitivity of CZTI provides an important handle to verify the polarization, by making observation of the same source at different roll angle. Thus, CZTI will have intrinsic cross verification capability for the measured polarization.

With the modulation factor and polarimetric efficiency provided by the Geant4 simulations and the polarimetric background estimated as mentioned above, we calculated the polarimetric sensitivity of CZTI as shown in Figure 2.19. It can be seen that the polarimetric sensitivity of CZTI in terms of Minimum Detectable Polarization (MDP) for a Crab like source and exposure time of 1 Ms will be of ~2.5% to 7% as a function of difference between the CZTI instrument axis and polarization angle of incident X-rays.

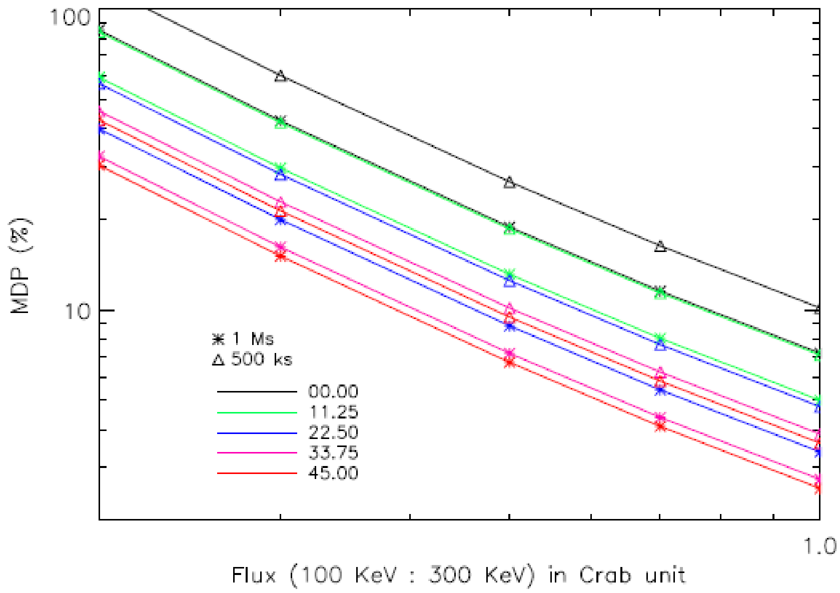

Figure 2.19:Minimum Detectable Polarization (MDP) as function of source intensity and polarization angle. 1 Ms and 500 ks time exposures are denoted by asterisks and triangles respectively.

Experimental verification of CZTI polarization measurement

In order to further confirm the hard X-ray polarization measurement capability of CZTI, we carried out another experiment using ^{133}Ba source. The experimental setup, as shown in Figure 2.20, was similar to the first experiment. However, considering much higher energy, 356 keV of X-rays from the ^{133}Ba source, a thicker (~3 cm) lead cylinder was used and the plastic scatterer was replaced by an aluminum cylinder. The 356 keV X-ray photons after Compton scattering at 90°, result in ~90% polarized beam with energy of 209 keV. However, in our experimental setup the allowed range of scattering angle was from 70° to 110°, and thus the resultant beam was expected to be ~70% polarized with a broad energy range of ~190 keV to 240 keV. Height of the polarized X-ray source was kept such that one full detector is fully illuminated. With this setup the data was acquired at polarization angles of 0°, 45°, 90° and 135° with respect the CZTI detector axis and exposure time at each angle of a few hours. Data was also acquired for the direct un-polarized beam of 356 keV X-rays. All data sets were analyzed by identifying the double pixel events i.e. two consecutive events occurring within 40 μs of each other in two adjacent pixels and satisfying condition of ratio of deposited energy. Histogram of azimuthal scattering angles for these events was generated assuming the pixel with lower energy deposition to be the scattering pixel.

Figure 2.20: Experimental setup to verify the hard X-ray polarization capability of CZTI. The partially polarized beam is generated by 70° – 110° scattering of 356 keV X-rays from ^{133}Ba source. The polarization plane of the incident beam is rotated by rotating the source to observe the change in modulation of the azimuthal scattering angle histogram

Figure 2.21 shows the histogram of the azimuthal scattering angles for the un-polarized beam. Since only eight adjacent pixels are considered, the histogram has only 8 bins.

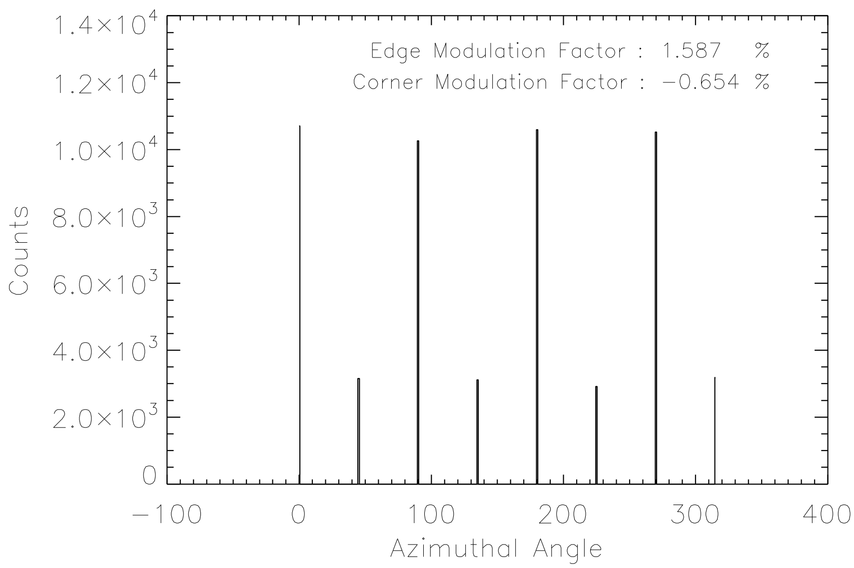

*Figure 2.21**:** Histogram of azimuthal scattering angle for un-polarized beam of 356 keV X-rays. The bins corresponding to edge pixels and bins corresponding to corner pixels do not show any modulation as expected.*

Further the bins at 0°, 90°, 180° and 270° angles corresponding to the edge pixels have more counts because these pixels cover larger azimuthal angle range, whereas the bins at 45°, 135°, 225° and 315° angles corresponding to the corner pixels have less counts because these pixels cover smaller azimuthal angle range. However, it can be seen that within four edge pixels or within four corner pixels, all pixels have same counts i.e. no modulation is observed. Figure 2.22 shows similar histograms for azimuthal scattering angles corresponding to the partially polarized incident X-rays.

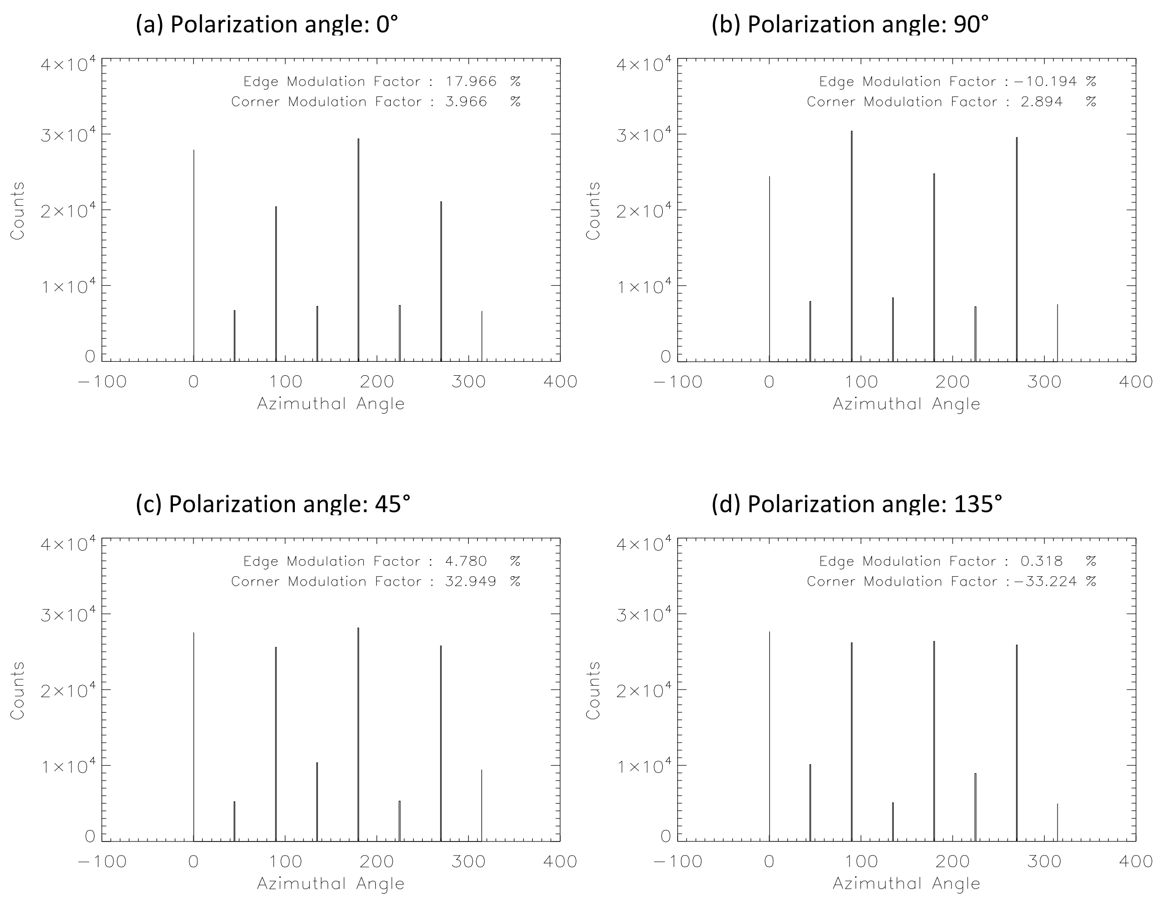

*Figure 2.22: Histograms of azimuthal scattering angles for the different polarization angles of incident X-rays. Changing modulation in edge pixels in case of polarization angles of 0° and 90° (panels **a** and **b**) and in corner pixels in case of polarization angles of 45° and 135° (panels **c** and **d**) can be clearly seen indicating that the CZTI modules can detect the polarization of incident X-rays*

It can be seen that for the incident polarization angles of 0° and 90°, the edge pixels show clear modulation but the corner pixels do not show any modulation as expected. In the case of the incident polarization angles of 45° and 135°, the corner pixels show clear modulation but the edge pixels do not show any modulation as expected. The modulation factors in both the cases are slightly smaller than those obtained from the Geant4 simulations, however this is because of two factors – 1) The beam is not 100% polarized as assumed in the simulations. 2) There is a significant contribution from the background as measured without any source. We verified this by repeating the Geant4 simulations for the actual experimental setup i.e. simulating the generation of the partially polarized beam due 70° – 110° scattering of the incident photons of 356 keV. We find that after considering both these effects, the modulation factor estimated by Geant4 and experimentally measured modulation factor agree within 1%. This suggests that for astrophysical observations, it is certainly possible to achieve the sensitivity as estimated in the previous section.

Thus CZTI is expected to have significant sensitivity for measuring hard X-ray polarization from the astrophysical sources and this will add completely new dimension to the scientific importance of CZTI.

2.8 Response matrix generation for CZTI

In general, the background intensity depends on the space environment as well as the material surrounding the detectors. Understanding the behavior of the background noise in the detector is very important to extract the precise source information from the detector data. This background noise measured with the detectors is estimated with Monte Carlo simulations, making use of GEANT-4 toolkit, and is presented in PDR.

The onboard calibration strategy would be:

a. Observe Crab at various incident angles.

b. Calculate the geometric area using the known CAM pattern and the known incident angle.

c. Use the calculated response to derive the source spectral index.

d. Critically examine the residuals.

e. Examine the spectral index as a function of angle and compare it with the published values.

f. Refine the assumptions based on the above two results.

It is expected that systematic errors would be less than the statistical errors for one hour of Crab observations, based on the response and area estimated before flight. Finer refinements (for longer and sensitive observations) have to be done based on the Crab observations.

Based on the test results, the strategy for the response matrix generation is as follows:

Use the multi-temperature lab data to generate gain-offset record for each pixel as a function of temperature. Periodically verify this onboard by using a collection of pixels.

For a group of pixels with similar characteristics, evolve a method of parameterizing the response. See Annexure VII for preliminary results. Study the variation of these parameters with energy, parameterize them, and store these data for each pixel.

Based on these parameters for each pixel, generate response matrix for a group of pixels. Assume computed effective area as a function of energy.

Since at high energies, the calibration sources are not `clean' (with a lot of Compton scattering in the holder as well as characteristic X-rays from the holder itself), use a small area high resolution CZT or CdTe detector to get the source emittence. Use the input energies and their relative strengths to fit the observed calibration spectrum.

The enormous amount of data collected during the calibration would be very useful to arrive at a good response matrix of the detectors.

2.9 Testing at various modes

The CZT Imager payload consists of 64 CZT detectors, organized as 4 quadrants, with each quadrant having its associated Front end electronics Board (FEB) to acquire and record event data. The FEB of each quadrant polls the 16 detectors of the quadrant in sequence and reads out the events from those detectors which indicate that there is an event to be read. The event is then time tagged and a 3 word event report is generated and stored in FEB memory.

The data from each quadrant is acquired by the Processing Electronics every second, for transmission to the satellite BDH. Depending on the operating environment and commanded conditions, PE identifies a mode of operation for each second. The data is packetized based on the data format and processing interval of the selected mode of operation. Mode ID and Data ID completely characterize the packetisation format. The mode of operation is identified from the mode ID and processing interval and packet type is identified from the data ID.

In this chapter, a brief description of each mode of operation and its associated data format is given. The integrated spectrum calculated from the data of a quadrant (Quadrant 1 populated with 16 detectors, with Am3 source at 20 C) for each mode, along with selected house keeping parameters is also provided to see how data is affected with change in the mode of operation.

2.9.1 Modes with Processing Interval 1s

The normal mode and 7 reduced modes of operation have a processing interval of 1s i.e. data is packetized every second in PE in these modes.

2.9.2 Normal mode

If a quadrant is ON and either CZT or Veto (or both) High Voltages are ON, and if no mode is commanded from ground, the Normal mode is selected as the default mode of operation. In the normal mode, the entire data from a quadrant is packetized. The number of packets depends on the CZT event count, with a maximum of 10 packets per quadrant. The data is prepared every second and packetized in the same second. The mode ID associated with this mode is ‘0’and processing interval is 1s. The normal mode packet is identified with Data ID ‘0-3’ for quadrants 0-3 respectively.

The integrated spectrum plotted from normal mode data is given below (note that the X-axis is channels rather than the generic title `Time’).

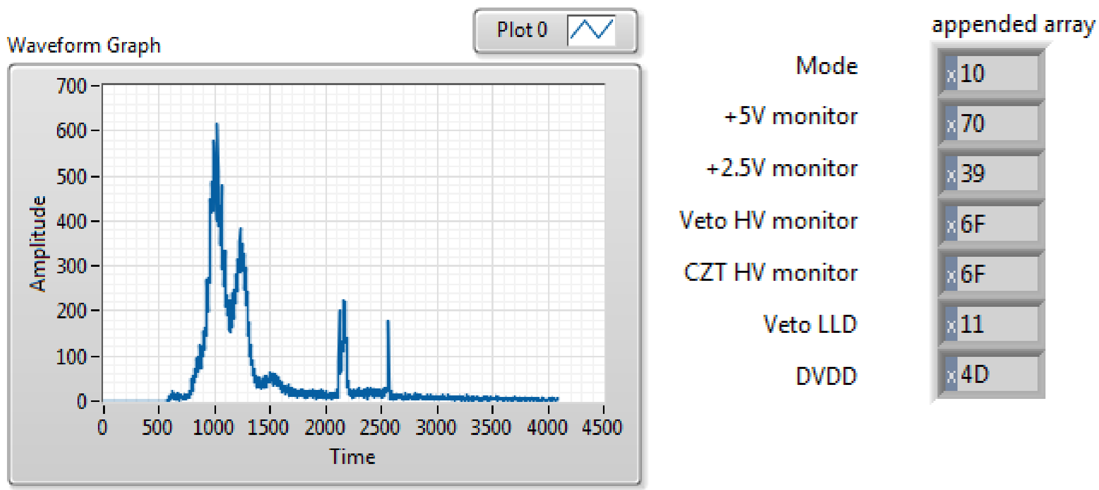

2.9.3 Reduced modes

If there is a need to reduce the number of packets generated from a quadrant, any of the reduced modes of operation can be commanded from ground. There are three primary reduced modes of operation, and all combinations of these primary modes are also possible; hence 7 reduced modes are possible. The mode IDs of the reduced modes are 1-7 and the associated data IDs are 0-3 (for quadrant 0-3). The processing interval for reduced modes is 1s.

<u>Reduced mode with Veto Spectrum Disabled</u>

In this mode, the 232 word veto spectrum from the quadrant is not packetized. The mode ID for this mode is ‘1’. The CZT event reports remain unaffected. The integrated spectrum plotted with reduced mode ‘1’ data is given below.

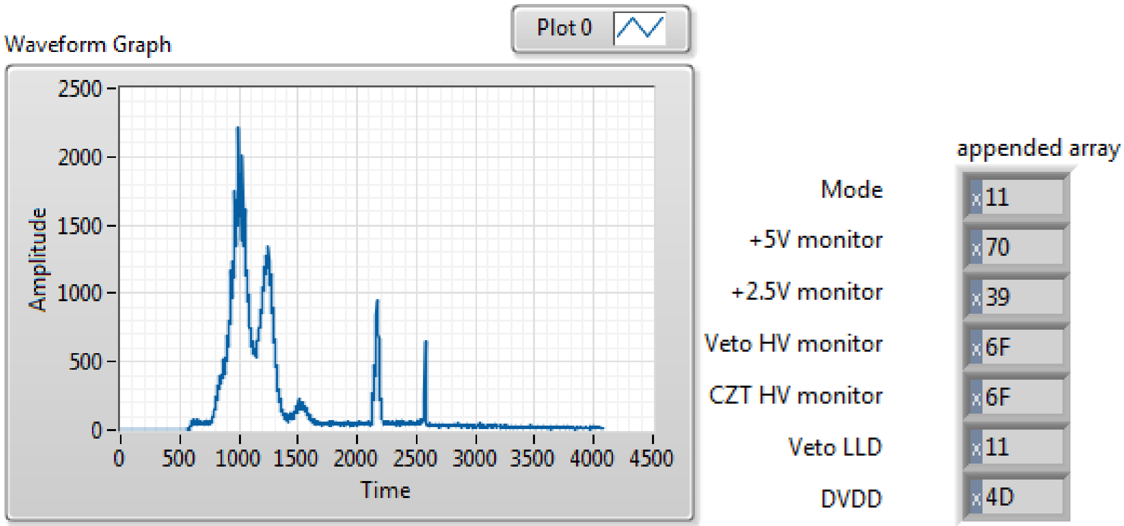

Reduced mode with 2 word event reports

In this mode, the three word event reports pertaining to the CZT events is converted to a 2 word event report in the following manner:

16 bit time is reduced to 9 bits

12 bit event energy is reduced to 9 bits in the following manner:

Event energy = Event energy -950

If event energy <0, event energy=0

If event energy > 2047, event energy = 2047

Event energy = event energy >>2

Detector ID, Pixel ID and alpha bit are maintained as such

7 bit veto ADC value is reduced to one bit indicating presence or absence of veto

This is applied to all the event reports received from the quadrant. The 232 word veto spectrum is also packetized in this mode. The mode ID associated with this mode is ‘2’.The integrated spectrum obtained from mode ‘2’ data is given below.

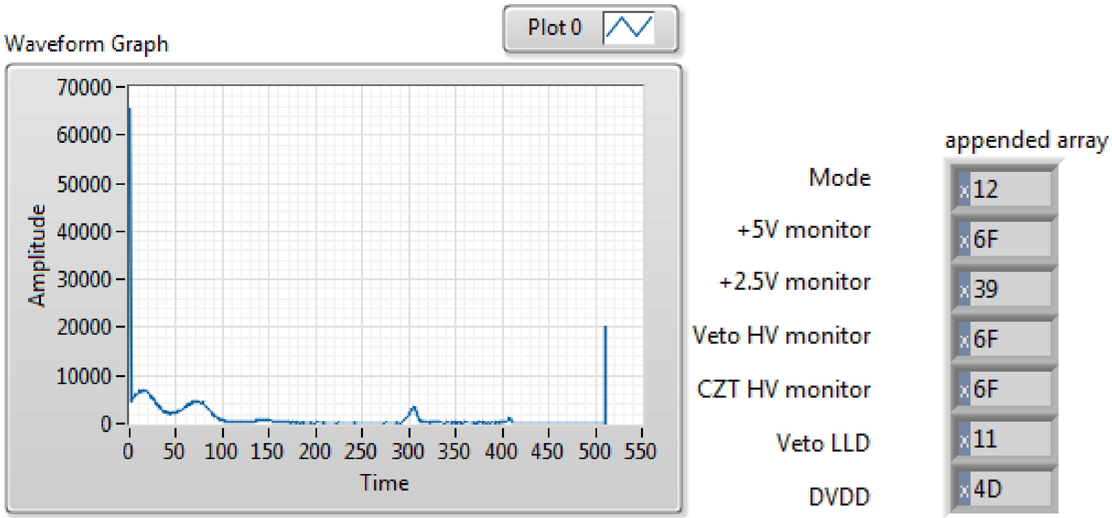

Reduced mode with Veto spectrum disabled and with 2 word event reports

This mode is a combination of modes 1 and 2. In this mode, the three word event report is converted to two word report as outlined above and the 232 word veto spectrum is not packetized. The mode ID of this mode is '3'. The integrated spectrum of mode '3' data is given below.

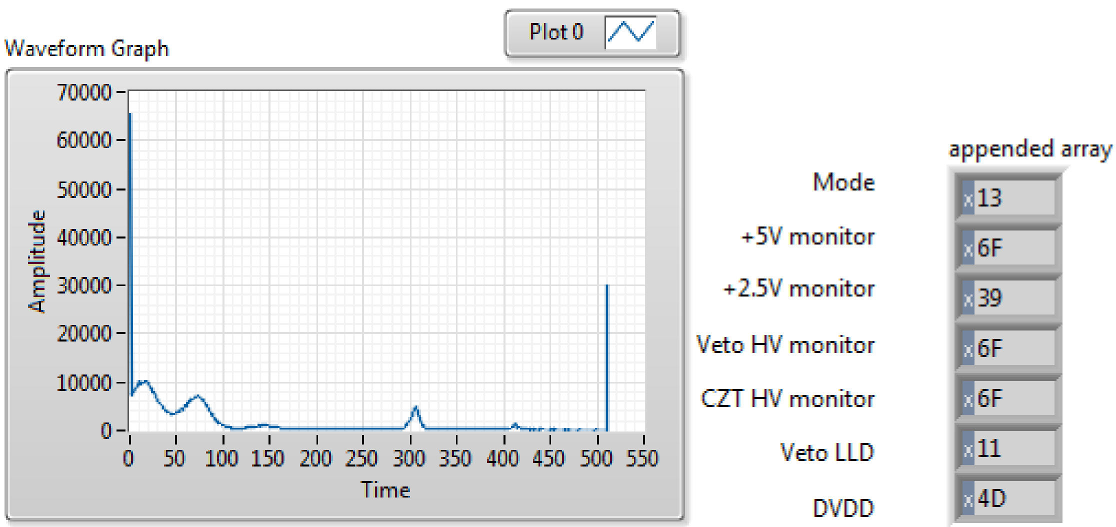

Reduced mode with fixed number of packets

In this mode, the number of packets to be generated in PE is as commanded from ground. If the number of packets required to packetize the events is less than commanded packet count, the lesser number of packets is chosen, otherwise, only those event reports which can be accommodated in the commanded packet count are packetized. The mode ID of this mode is '4'. If the commanded packet count is '0', no packets are generated in every second. A header packet will be sent at the 100 second boundary.

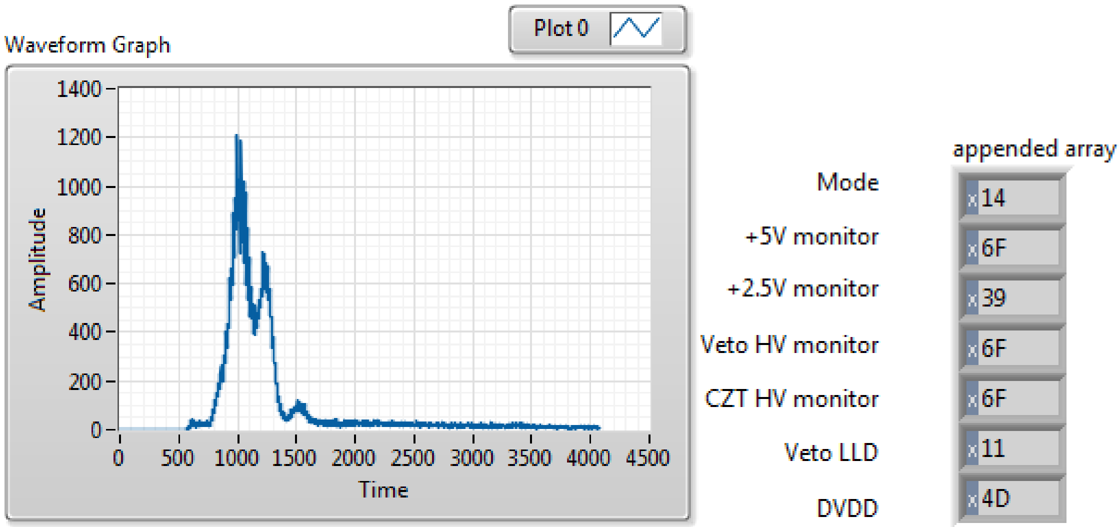

Reduced mode with fixed number of packets and Veto spectrum disabled

This mode is a combination of modes 4 and 1. The 232 word veto spectrum is not packetized in this mode and the maximum number of packets generated per second is the commanded packet count. The mode ID of this mode is '5'.

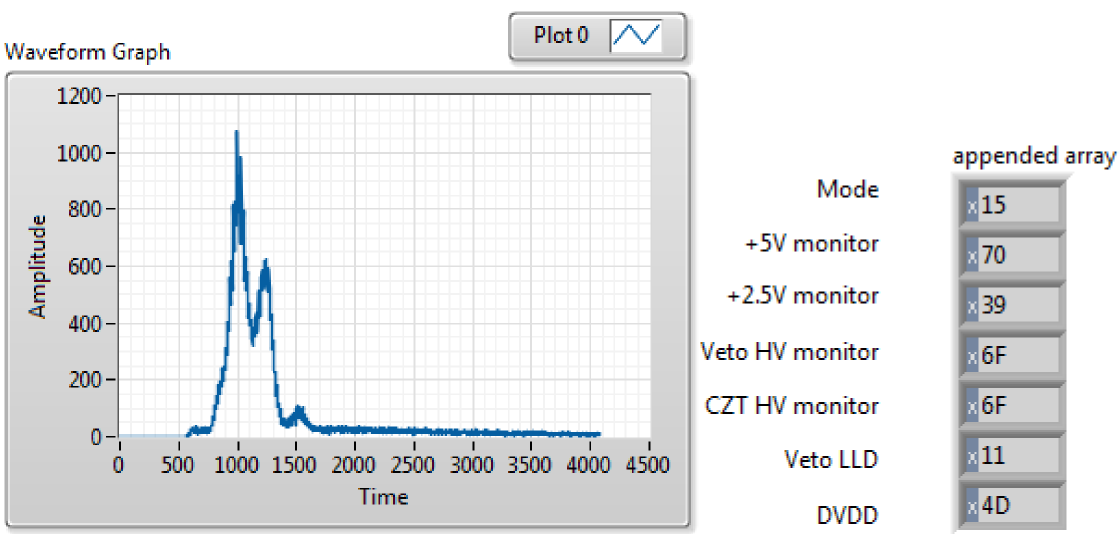

Reduced mode with fixed number of packets and 2 word event report

This mode is a combination of modes 4 and 2. The 3 word event reports are converted to 2 word reports as in mode '2' and only those many events are packetized as can be accommodated in the commanded packet count. The mode ID of this mode is '6'.

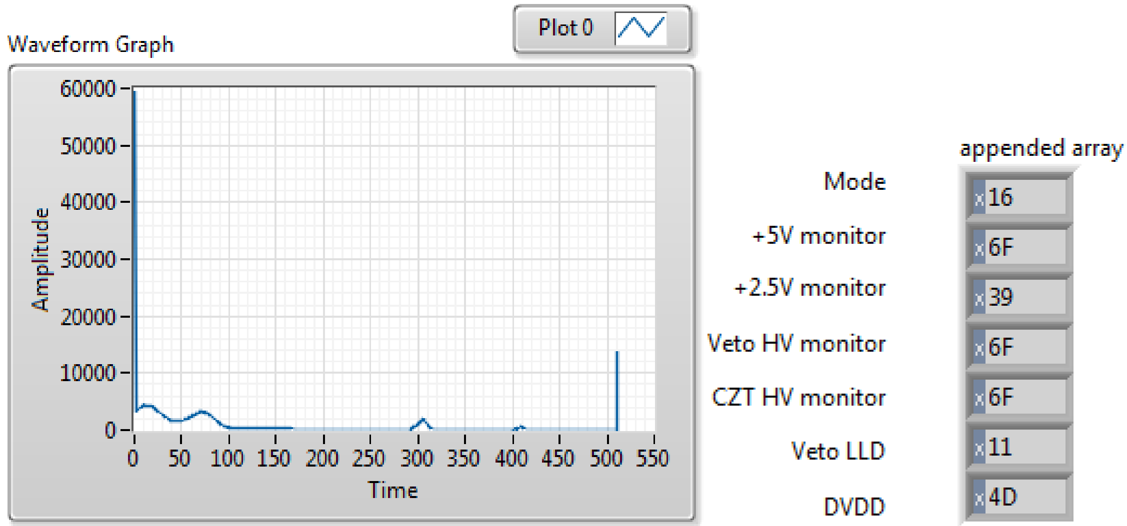

<u>Reduced mode with fixed packet, veto spectrum disabled and 2 word event report</u>

This mode is a combination of all three primary reduced modes. The maximum number of packets generated is as specified in command and the 232 word veto spectrum is not packetized. The three word event reports are converted to 2 word reports. The mode ID of this mode is '7'.

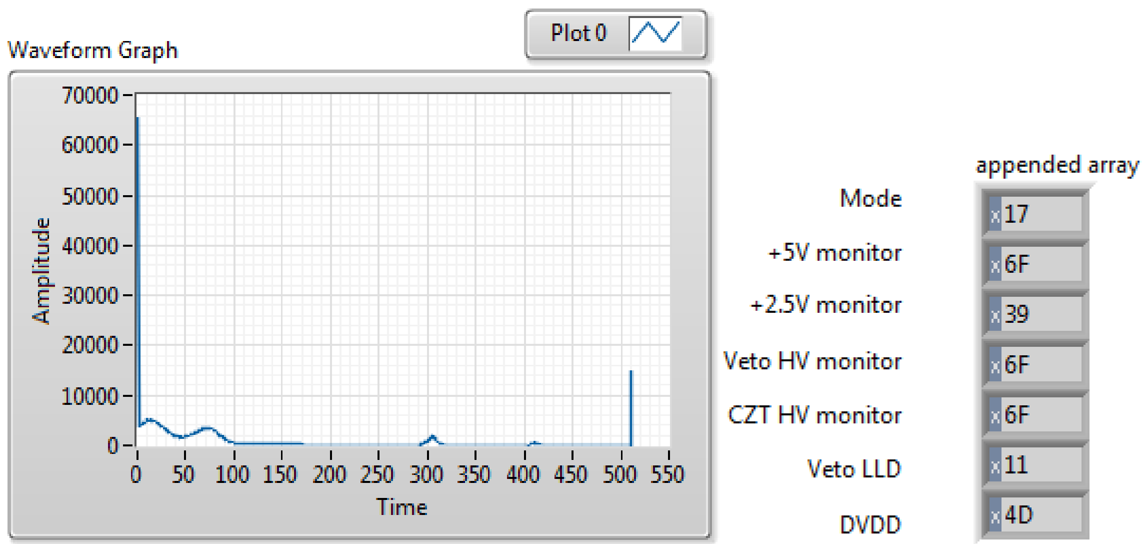

2.9.4 Modes with Processing Interval 100s

This includes SAA, shadow and Memory full modes and their various combinations. In these modes, data is prepared every second from the acquired FEB data, but is packetized only at the 100s boundary. In these modes, header and SSM packets are received. Header packet is identified with data ID 4-7 and SSM packets with data ID 8-11.

2.9.5 SAA mode

This mode of operation is entered into if PE finds that both the High Voltages are Off. This can either be due to both HVs being turned off through command or due to entry into SAA region. SAA region is characterized by high charge particle count and the detector HVs are automatically turned Off by PE when an indication regarding SAA entry is received. When indication of SAA exit is received, the previous state of operation is resumed automatically. SAA entry/exit is determined through tele- command or level signal from CPM and the selection between the two logics (Command alone, CPM alone, command or CPM) can be commanded. In this mode, the FEB header of each second is compiled into a header packet that is packetized at the 100s boundary. The SSM packets are not received in this mode. The mode ID of this mode is '9'.

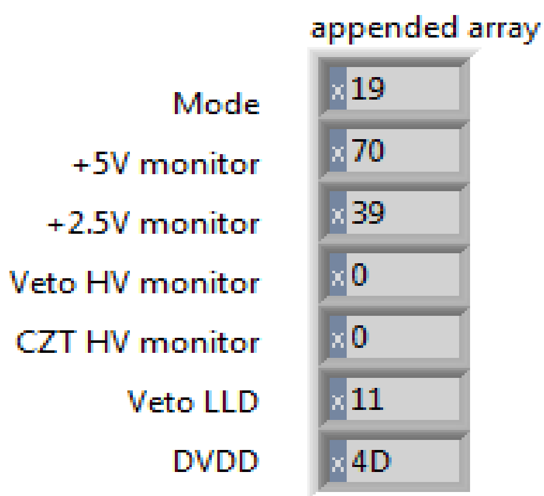

2.9.6 Shadow mode

This mode is entered into when the respective command is received from ground. Shadow exit is also as per ground command. In this mode, 1s data is not packetized. As in SAA mode, FEB header of each second is compiled into a header packet which is packetized in the 100s boundary. However, in this mode, SSM packets are also received. The spectra plotted from the SSM packet data is shown below. In the SSM packet, 12 bit energy is converted to 9 bit energy as explained in mode 2 and the 512 word spectrum is calculated over a 100s intervals. The mode ID of this mode is '10'.

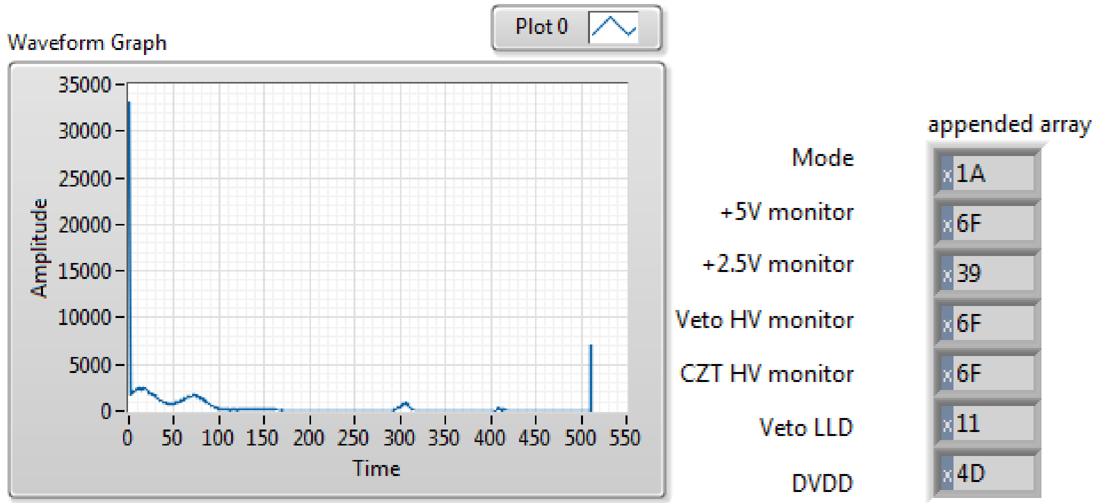

2.9.7 SAA and Shadow mode

This mode is a combination of the SAA and Shadow mode. Both HVs are turned off in this mode and only header packet is received at the 100s boundary. The mode ID of this mode is ‘11’.

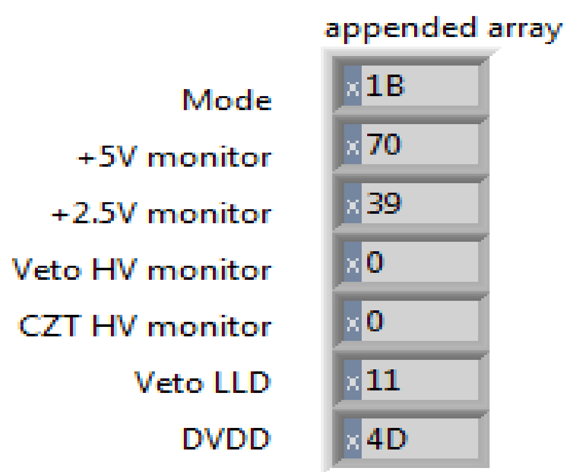

2.9.8 Memory full modes

PE continuously sends packets to satellite BDH as long as memory full signal from BDH is low. When MF is high, PE stops sending packets to BDH and stores them in PE internal memory. To prevent overwriting and for efficient utilization of the limited PE internal memory, memory management schemes are implemented where the number of packets generated reduces as PE memory gets filled up. In this regard, various memory levels are defined and the packetisation scheme varies with each level. In level 0, normal packetisation is done. In level 1, any of the reduced modes (as preset through command) is entered into. In level 2, header and SSM packets are only sent. In level 3, only header packets are sent and in level 4, no data is packetized. Memory level greater than 1 (2 and 3) is included in the 100s modes to differentiate the cause for receiving 100s data.

2.9.9 Memory level >1 mode

In this mode, header and SSM packets are packetized at the 100s boundary. The mode ID of this mode is '12'. The spectra plotted from the SSM packet of mode '12' data is given below.

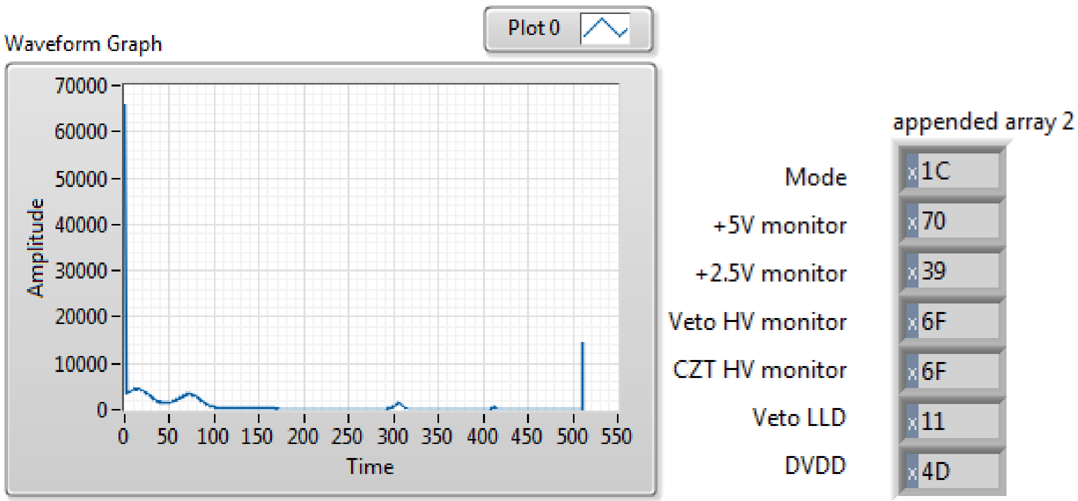

2.9.10 Memory level>1 and SAA mode

In this mode, memory level is greater than 1 and both HVs are Off as in SAA mode. The mode ID of this mode is '13' and only header packet is received at the 100s boundary.

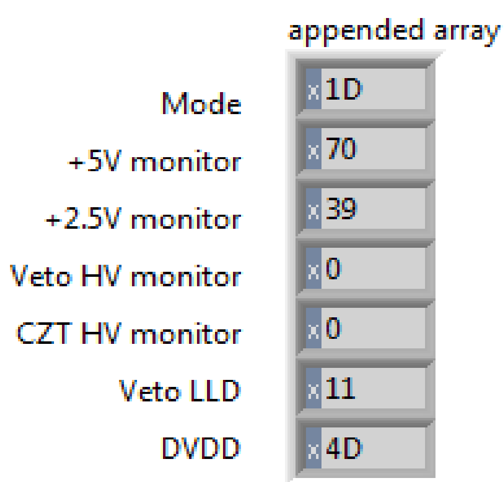

2.9.11 Memory level>1 and Shadow mode

This mode is a combination of modes 10 and 12. The mode ID of this mode is '14' and header and SSM packets are received at the 100s boundary. The spectra plotted from SSM packet of this mode is shown below.

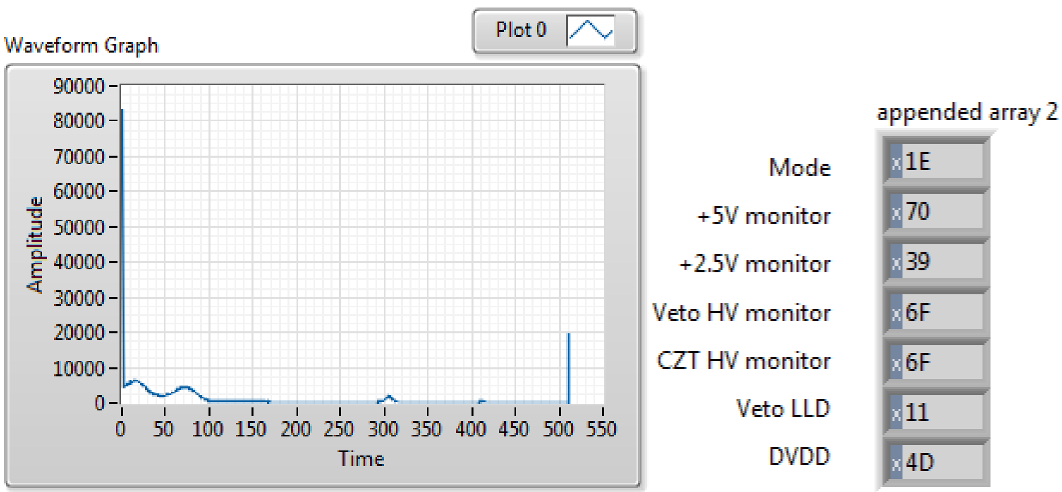

2.9.12 Memory level>1, SAA and Shadow mode

This mode is a combination of modes 9, 10 and 12. In this mode, both HVs are OFF and only header packet is received at the 100s boundary. The mode ID of this mode is 15.

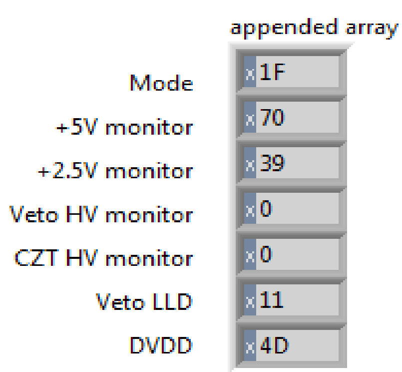

2.9.13 PE Header mode

In this mode, all the quadrants are switched OFF. There is no FEB data to be packetized, so certain parameters of PE are compiled into 1 packet at the 100s boundary. This mode is characterized by a data ID of '16'.

2.10 HK Parameters

The average values and variations of the HK parameters have been added in the following tables

FQ0						
Temperature(C)	HK1 (Supply Voltage)	HK2 (Thermistor)	HK3 (VCCA)	HK4 (CZT HV)	HK5 (Veto HV)	HK6 (DVDD)
0	1814 ± 5	721 ± 15	926 ± 6	1811 ± 5	1806 ± 5	1249 ± 5
5	1810 ± 6	705 ± 12	925 ± 5	1807 ± 5	1802 ± 5	1253 ± 5
10	1807 ± 4	686 ± 16	923 ± 6	1804 ± 8	1798 ± 6	1256 ± 5
15	1804 ± 5	664 ± 12	921 ± 6	1800 ± 5	1795 ± 4	1260 ± 5
20	1800 ± 4	639 ± 11	920 ± 6	1797 ± 4	1792 ± 5	1263 ± 5

FQ1						
Temperature(C)	HK1(Supply Voltage)	HK2 (Thermistor)	HK3 (VCCA)	HK4 (CZT HV)	HK5 (Veto HV)	HK6(DVDD)
0	1817 ± 6	712 ± 16	934 ± 6	1814 ± 5	1809 ± 6	1277 ± 6
5	1814 ± 5	696 ± 9	932 ± 5	1811 ± 6	1806 ± 6	1280 ± 5
10	1811 ± 6	677 ± 12	931 ± 5	1807 ± 4	1802 ± 5	1284 ± 4
15	1807 ± 5	655 ± 7	930 ± 6	1804 ± 4	1799 ± 4	1288 ± 4
20	1804 ± 5	631 ± 6	928 ± 6	1801 ± 4	1796 ± 5	1292 ± 5

FQ2						
Temperature(C)	HK1(Supply Voltage)	HK2 (Thermistor)	HK3 (VCCA)	HK4(CZT HV)	HK5(Veto HV)	HK6 (DVDD)
0	1809 ± 5	710 ± 18	930 ± 6	1807 ± 6	1802 ± 5	1252 ± 5
5	1806 ± 7	694 ± 13	928 ± 5	1803 ± 6	1798 ± 6	1255 ± 5
10	1803 ± 5	675 ± 15	927 ± 6	1799 ± 5	1794 ± 4	1258 ± 7
15	1800 ± 5	653 ± 12	925 ± 6	1796 ± 3	1791 ± 5	1262 ± 4
20	1796 ± 4	628 ± 11	924 ± 5	1793 ± 5	1787 ± 5	1265 ± 4

FQ3						
Temperature(C)	HK1(Supply Voltage)	HK2 (Thermistor)	HK3 (VCCA)	HK4 (CZT HV)	HK5(Veto HV)	HK6 (DVDD)
0	1815 ± 5	717 ± 20	928 ± 6	1811 ± 6	1807 ±6	1269 ± 6
5	1811 ± 6	701 ± 7	927 ± 6	1807 ± 6	1803 ± 7	1273 ± 5
10	1807 ± 4	682 ± 12	925 ± 6	1804 ± 5	1799 ± 4	1278 ± 10
15	1805 ± 6	661 ± 15	924 ± 5	1800 ± 5	1796 ± 5	1282 ± 5
20	1801 ± 5	637 ± 4	922 ± 5	1797 ± 3	1792 ± 5	1286 ± 6

Table 2.16

2.11 STBG Test

The final assembled payload was tested with the flight STBG. The tagged onboard time (correct to a micro-sec), every 16 seconds accompanying the LAXPC pulse, are examined in detail. The Delta time (in micro-seconds) for successive pulses, over and above 16 seconds, is plotted in the following figure, as a function of LAXPC pulse number. It can be seen from the figure 2.23 that the drift of the PE clock is less than 1 ppm and based on the LAXPC signal the PE time can be calibrated and corrected to an accuracy of about a micro-sec.

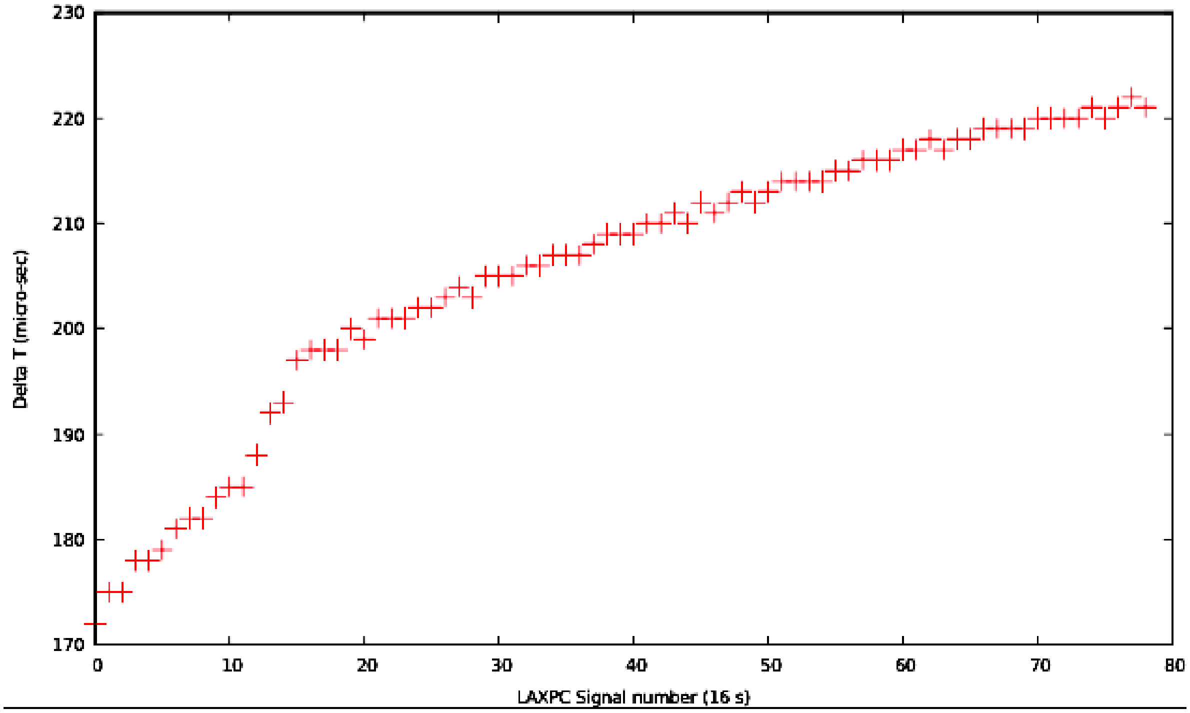

Fig. 2.23

3. Test and Evaluation of Detectors:

3.1 Test Setup:

The ASTROSAT Checkout System (ACS) consists of following equipments.

Power Supply : +37V, 2A

Power Supply : +5V, 1A

Power Supply : +5V, 1A

Function Generator

PC with NI Card 6534

NI Connector Box and Cable

ASTROSAT Check Out Card

Pulse Command Simulator

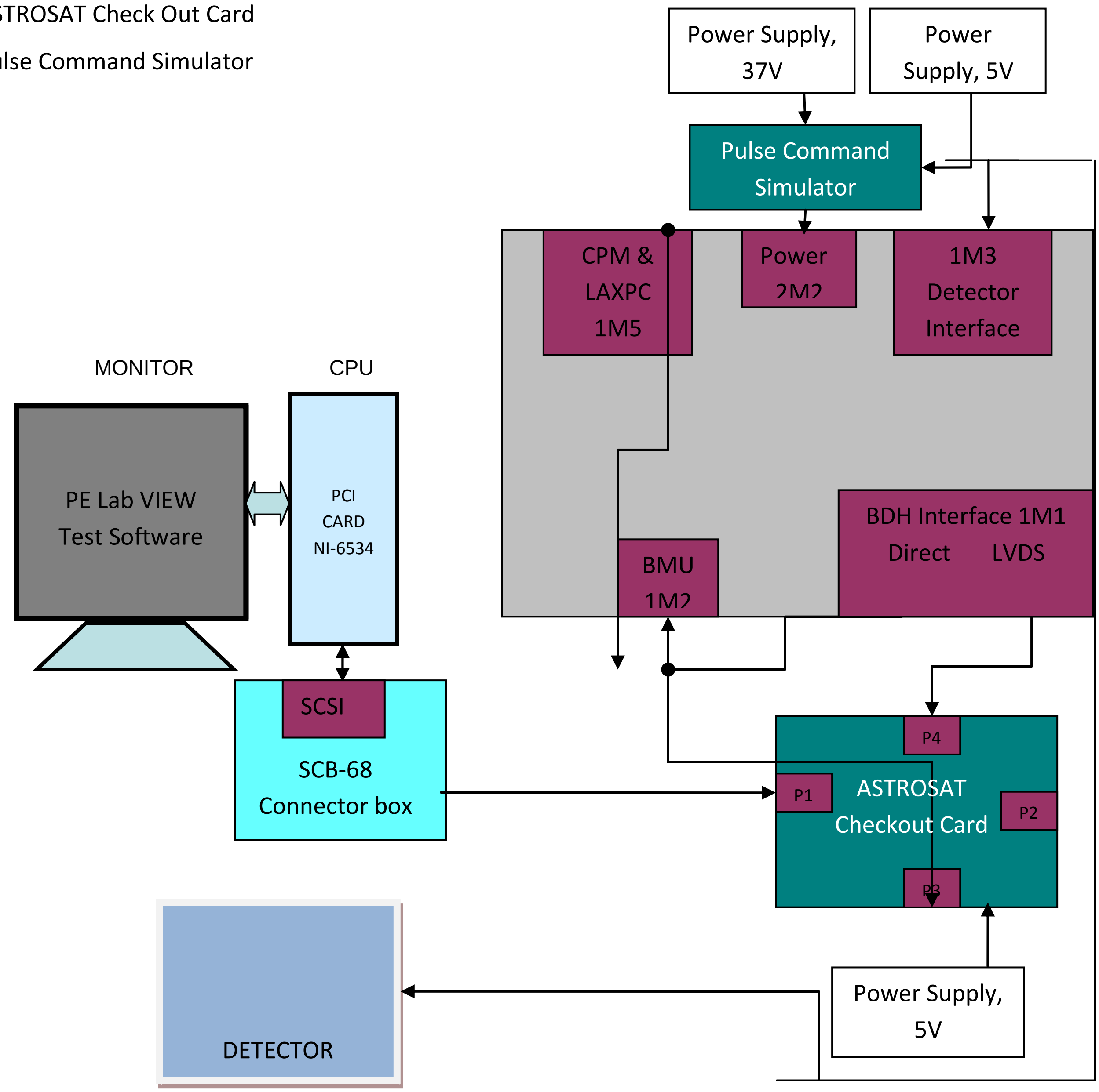

Fig 3.1: Test Setup for CZTI

3.2 Test Sequence:

The table below mentioned tests were performed as a part Qualifying the CZTI QM and FM at VSSC. (Annexure I)

Test	Description	
	QM	FM
Initial SRC	Pre environmental test at standard room condition	Pre environmental test at standard room condition
EMI/EMC	1. Conducted Emission :CE03, CE07 2. Radiated Emission :RE02 3. Conducted Susceptibility :CS01, CS02, CS06 4. Radiated Susceptibility	1.Conducted Emission :CE03 2. Radiated Emission :RE02 3. Conducted Susceptibility:CS01, CS02, CS06 4. Radiated Susceptibility :RS03
Thermal Cycling	1. -15^{0}C for 6 Hrs followed by 35^{0}C for 6Hrs	1. -15^{0}C for 6 Hrs followed by 35^{0}C for 6Hrs
Vibration test	1. Sine vibration 2. Random Vibration (3 axes QM levels)	1. Sine vibration 2. Random Vibration (3 axes Proto-FM levels)
Thermo vacuum test	1. at -15^{0}C and 35^{0}C 2. 5 short cycles – dwell time 2 hours 3. 1 long cycle – dwell time 24 hours	1. At -15^{o}C and 35^{o}C 2. 5 short cycles – dwell time 2 hours 3. 1 long cycle – dwell time 24 hours
Final SRC	Post environmental tests at standard room condition	Post environmental tests at standard room condition

Table 3.1: T&E sequence for CZTI QM & FM

Detailed test results are given in the appropriate documents and a summary of the Flight Model results are given here.

Ref: QDTE/TP/CZT Imager/257

3.3 Test Results for QM module

3.3.1 Summary of Failures:

Sub No.	Test condition	Failure symptom	Reason for failure	Corrective Action	Failure Category	FAB status
1.	Thrust axis random vibration	During thrust axis vibration, the four slots out of sixteen (CZT 5, 6, 10 & 11) of the CAM structure above the populated quadrant of the package were broken. The broken pieces fell inside the package.	Design error	CAM structure was redesigned as per the recommendations of the FAB and the vibration test was carried out in thrust axis.	Design	Closed
	Lateral-2 Axis Sine Vibration	During sine vibration in lateral 2 axis, three mounting screws (M6) on one side of the package along the axis of vibration were broken and got detached from the fixture. This has happened towards the end of the vibration	Setup related	Used new mounting screws recommended from ISAC	Setup	

Table 3.2

3.3.2 Deviations from specifications

S. No.	Test condition	Parameter	Specification	Measured Value
1	All the phases of T&E	CZT spectrum for the CZT 3 and 7	Background spectrum	Up to 25 counts peaks at energy levels near 1000 (CZT 3)
				Up to 25 counts peaks at energy levels near 1000 and1500(CZT 7)
2	All the phases of T&E	Thermocouple output value for TE11 (fixed at quadrant 3 inside the package)	Should vary w.r.t. the external temperature	Thermocouple value is showing open for TE11
3	Thrust axis vibration (2^{nd} sub)	Veto count in Veto spectrum	≈1000 counts	Veto count is high ≈4500 counts

Table 3.3: Deviations from specifications for QM

3.3.3 Detailed Test Results for QM module

Test Condition	Specification	Performance
Pre Environmental tests at SRC	Visual inspection	Normal
	Continuity & Isolation tests	Within specification
	Supply Voltage & Current Measurement	The current drawn by the package at 42V supply voltage was measured as 410mA.
	Functional Tests	Performance was found to be satisfactory
	Command checks	1. Switching on the HV by commands (to CZT and Veto detectors) and increment in current rating was noticed. 2. Invalid commands were given and observed that they are not affecting the previous commands/system functionality. For example, invalid CZT HV, Veto HV commands were given and no change in the detector performance or current increment is noticed.
Environmental Tests	EMI tests	Normal

	Pre Calibration test	Detector's performance to the source radiation compared to background was satisfactory
	Thermal Cycling Cold soak & Hot soak test	The overall performance of the payload was satisfactory during both cold soak and hot soak
	Vibration Test	The full functional verification of the package was carried out after each vibration test. The payloads' performance found satisfactory
	Thermo Vacuum Test	1. All the parameters in the functional test as given above were found to be satisfactory to the required values. 2. The detector module temperatures were also checked for the temperature levels which were found to be within the limits in the range of the operating temperature of the modules. 3. The thermistors' outputs were also monitored in each of the cycles. 4. The overall performance of the payload was found good.
	Post Calibration Test	1. It is observed that the number of pixels behaving as noisy and dead is more in the higher temperature levels when compared to the lower temperatures. 2. In the spectral analysis, it is noted that the peak position of the detected radiation found to be in the desired positions
Post-Environmental Tests	All the tests referred in Pre Environmental tests at SRC were conducted	The performance of the FM module conformed to Initial SRC results

Table 3.4: Detailed T&E Test Results for QM module

Ref :QDTE/PAR/308/2011

3.4 Test Results for FM module

The Flight Model (FM) was submitted for the final test and evaluation. The same test procedure, as was done for the QM, was used, but with the following major changes:

1. Proto-flight test philosophy was used
2. The proto model of PE was used for all test and evaluation.

In the EMI/EMC tests, the alpha detectors were found to be misbehaving during the conductivity tests. These detectors were using an electronic circuitry similar to that used for CPM (where a similar failure was noticed and rectified). The filtering circuitry were improved and the package was re-submitted. All EMI/EMC tests were conducted successfully.

During the final thermovac, the veto supply mal-functioned. This was attributed to the failure of a transistor. This component, and several other surrounding components, was replaced and the package was re-submitted. Again, during the final thermovac, the same transistor malfunctioned. After a detailed discussing with VSSC FAB and ISAC teams, it was decided to make a new power card. The fault was identified to corona, The potting method was improved, implemented in all 4 veto cards, card alone tests were conducted, and the final thermovac was carried out successfully.

After the thermovac, all the calibrations were carried out at different temperatures.

4. Concluding Remarks

The extensive calibration carried out on the FM detectors demonstrated the following:

They can be used as good spectroscopic detectors (~20% at 22 keV; 8-9% at 60 keV and 6% at 100 keV). The low energy threshold can be maintained at 10 keV for a majority of the detectors in the working temperature. The average threshold as a function of the operating temperature and the efforts involved in identifying and suppressing noisy pixels on a continuous basis are quantified. Detectors from the same flight batch have been used in the RT-2 experiment demonstrating stable on-orbit performance for about 9 months (with thresholds of 20keV for 1 detector and 40 keV for the other 2 detectors). The earlier versions of the detectors from the same manufacturer with similar CZT crystal growth and detector packaging processes have been flown onboard the Chandrayaan-I mission and operated successfully. Hence, once the package qualifies the performance tests during the environmental tests, it is safe to conclude that they will provide consistent onboard performance.

Since the devices are delicate and use LVDS for communication, they have to be handled carefully. Full detector failures (about 8 out of 150) are noticed in the past few years, which can be clearly attributed to bad electrical handling. Any operation in extreme conditions can lead to an incremental loss of good pixels (causing them to be dead or noisy), but the cumulative loss, for the selected detectors, has grown from < 1% from the fresh batch (dead and noisy pixels), to about 1 - 2% after screening, thermal cycling during calibration etc. The final desired objective is to have > 90% good pixels in-orbit. Another bad handling done with some disastrous effect was to subject them to sudden temperature excursion (the erroneous use of dry ice during lab tests for QM and one of the flight quadrants) which resulted in spectral deformity in about half a dozen detectors (one of these detectors showed a miraculous recovery after subjecting it to 60 C baking).

Classification of the pixels into photometric (for imaging and timing studies) and spectroscopic would be based on some subjective criteria like the desired range in resolution and will depend on the specific scientific purpose. For example, for spectral studies of weak sources like AGN, most of the pixels would be used whereas for a detailed spectral study of cyclotron lines, about 80% of the pixels would be used.

Another remarkable by-product of the detailed testing is the demonstration of the use of CZTI for above 100 keV operations. This is particularly important because ASTROSAT would be operational contemporaneously with NuStar and Astro-H and probably ASTROSAT would not be that competitive for spectral studies below about 60 keV. Hence, the demonstration of the use of CZTI above 100 keV for all sky monitoring, spectral studies above 100 keV for bright sources, making use of Compton scattering for polarization measurement are some of the unique capabilities which can be scientifically exploited.

The auxiliary detectors, CPM, Alpha, and Veto use old fashioned crystal detectors. Since the knowledge of SAA is critical for the operation of X-ray detectors, it is suggested that the CPM output should be used with an OR logic with the commanded SAA positions. CPM could be used to extend the SAA region. In case of CPM failure, commanded values will ensure proper functioning and the instruments would be operating in mildly higher rates for a few orbits.

Alpha was designed to provide onboard calibration. In the original estimation, it was expected to provide a few counts per second per detector, but the actual implementation caused a factor of 10 lower count rates. This has forced to make a collective pixel-wise onboard calibration for the verification of the stability of the spectrum. Perhaps, a better design would have been to have low noise amplifiers and use only the Si photo-diode and avoid the CsIcrystal which blocks the X-rays.

The Veto detector is efficient for Compton scattering events. Since this demands a forward scattering event, the background suppression is only a few percent, as was evident in the simulations. The large area (1000 cm^2) can be exploited as a transient detector: but without onboard calibration, this needs to be verified after the detection of a few GRBs and cross-calibrating with other instruments.

Since the CZT detectors were screened about 5 years ago, the main thrust of the multi-temperature calibration was to verify their behavior in the flight operating conditions. Though a majority of the detectors are of `Very good’ and `Good’ category, it was found that about 8% of detectors are of `poor’ quality.

Since a comprehensive understanding of the detector performance is required for the full utilization of the CZT-Imager data, the following works will be carried out in due course leading to the performance verification:

1. **Energy calibration:** It is found that the energy calibration, stability, and ability to correct for temperature, is accurate to about 0.5 keV (at 60 keV) to 1 keV (at 122 keV).

This is sufficient to get the desired results (spectrum, flux, etc.) to about 1% of the statistical accuracy. A parallel plan of improvement would be attempted. The radio-active sources used for the calibration were used to get spectrum by a high resolution CdTe detector. Using this data, the source function would be defined and the appropriate correction for source blending (particularly at 22 keV and 33 keV) would be incorporated. By this method, the energy scale, their stability, and extrapolation to low energy can be made accurate to 0.2 keV. This will be attempted and compared with PV data on the Crab nebula.

2. **Overall area**: The overall effective area is now measured correct to 10 – 20% accuracy. To improve on it, the line energy results described above will be used to measure the relative line intensities. An interactive source fitting method will be used to drive down the error to about 5% accuracy. This will be used in conjunction with the PV phase Crab observation.
3. **Imaging**: There is sufficient knowledge of the geometry of the system to recover the position and counts by the masking method. This is sufficient to derive the source intensity and spectrum, a major advance in this field is possible by developing new techniques to measure the position and spectrum simultaneously.
4. **Polarimetry and sources above 100 keV**: The present analysis technique (and calibration results) is sufficient to get polarization of bright sources (like Crab). To get these values for sources outside the FoV (like GRBs) would require a major effort in developing techniques to simulate Compton scattered events in a complex geometry. This aspect, as well as getting fluxes of bright sources outside the FoV, would be attempted at a later stage.

Calibration activities leading to PV Phase observations

1. **Spectral Response**

Currently, pixel-wise spectral response (gain and offset) is available. This is correct to 0.5 keV to 1 keV accuracy. For the first order response matrix generation, this information is sufficient. The major source of errors are identified to be: 1) blending of peaks at low energies, 2) count statistics and/or noise effecting the results in the automatic analysis, 3) method of taking the spectral asymmetry. An effort, however, will be made to improve this to about 0.2 keV. For this purpose, data taken using CdTe detectors would be used to determine the source function and joint spectral fitting method would be adopted to arrive at a pixel wise gain offset values. This will be repeated for all temperatures and finally a table would be generated with accuracy achieved for a) best 75% of pixels, b) 75 – 90 percentile pixels and the bottom 10% pixels.

A detailed paper would be brought out before the commencement of the PV phase observations.

2. **Response Matrix generation**

The current pixel-wise response matrix is correct to about 1% accuracy. Improvement on this would require major efforts in multiple directions. These are: a) spectral response (point 1, above), b) incorporating charge sharing effect at the edges, c) mu-tau effect, d) effective area. In the response matrix, appropriate facility to incorporate these would be implemented and the final verification would be done after the Crab observations. Hence, the activity in this area can be divided into two parts: a) summarizing the above factors in a document before the commencement of the PV phase observations and b) verification of the response using Crab data.

3. **Individual pixel understanding**

Flickering pixels are found to be rare occurrences (1 or 2 pixels in a module of 256 pixels). The methodology of identifying flickering pixels would be implemented and all data would be examined. A pixel-wise data base would be created before the commencement of the PV phase.

4. **Checklist before PV phase**

The following will be available before PV phase:

a. A detailed pixel-wise history log (including flickering)

b. A table giving best achieved accuracy in gain-offset correction

c. Response matrix incorporating the above two points

d. Caldb file

Annexure I

Imaging Tests With Astrosat Czti QM

The Qualifying Model (QM) of the ASTROSAT CZTI was used to test and validate the coded mask imaging procedure. A fixture was made to position a radioactive source at several possible locations, about 90 cm above the detector plane of a single CZT module of 16x16 pixels. The radiation from the radioactive source, on its way to the CZT detector, was intercepted by the coded mask plate situated at a height of 48 cm above the detector plane.

The photons detected by the CZT module were accumulated into an event list, recording the position (pixel number), energy (PHA channel number) and time of each event. These data were then analysed using the CZTI imaging algorithm and the location of the source thus reconstructed was compared with the position at which the radioactive source was placed during the acquisition of this data.

The reconstruction process began by counting the total number of events recorded in each detector pixel, resulting in a Detector Plane Histogram (DPH). Each count value in the DPH was then divided by the relative quantum efficiency of the corresponding pixel. The array resulting from this is called a Detector Plane Image (DPI). This DPI is a linear combination of shadows of the coded mask cast on the detector plane by sources in the field of view. It also contains a small component contributed by the background, which was ignored since the radioactive sources used in this experiment were very bright.

It is to be noted that this experimental set-up produces shadows that are different from what would be expected from astronomical sources duringthe flight of the instrument. This is because the radioactive source here, located close to the detector, shines a diverging beam of radiation on it, unlike the parallel beam expected from astronomical sources. Given the relative height of the mask and the source plane, the shadow footprint of a mask element is nearly twice as large as the element in every direction, causing the full detector to be populated by the shadow of only one quarter of the mask. This drastically reduces the available coding information at the detector plane and thereby affects the quality and precision of the reconstruction process.

To proceed further in the reconstruction, a library of shadow patterns expected from sources located at different (x,y) positions on the source plane was created by a ray tracing method, assuming the emission pattern of the radioactive source to be intrinsically isotropic. Source locations were chosen in the range -19.5 to +19.5 mm in both x and y direction, in steps of 0.25 mm. The zero reference for (x,y) was at the location on the source plane directly above the centre of the detector.

Three different methods were then followed to recover the source location from the DPI:
Cross correlation (CC): The DPI was cross correlated with each of the computed shadow patterns in the grid and the values of the cross correlation products were stored as a matrix on the grid
Shadow fitting: A chi-square value was computed for the deviation of the observed DPI from the expected shadow for each location of the grid. The position for which the value of this chi-square was minimum was chosen as the reconstructed location of the source.
The Richardson-Lucy (RL) algorithm, based on Bayesian inference, was applied. This is an iterative method that starts with a guess source distribution *S(k)* at sky elements *k*, and at each step improves the guess solution by a correction factor *C(k)* determined from:

$$C(k) = \sum_j R(j,k) D(j) / P(j)$$

where

$$P(j) = \sum_k R(j,k)S(k)$$

is the predicted count at detector element *j* for the source distribution *S(k).* The quantity *R(j,k)* is the shadow pattern, giving the expected counts at detector location *j* for an unit strength source at sky location *k*. *D(j)* is the observed DPI. All the distributions, *S(k)*, *D(j)*, *P(j)* and *R(j,k)* are area normalized to unity.

As the iteration proceeds, the values *C(k)* approach unity. The iteration is terminated when they have converged to unity within a pre-set tolerance.

Five different data sets were obtained by placing an Americium (60 keV) source at different locations, and one data set was obtained by simultaneously placing an Americium (60 keV) and a Cobalt (122 keV) source at two different locations on the fixture. All these data sets were subjected to the analysis outlined above. In case of the two-source data, two DPH-s were separately constructed, one from photons recorded near 60 keV, and another for those near 122 keV. Each DPH was analysed independently. The results of these reconstructions are summarised below:

Data ID	**Position In the lab (mm)**	**Reconstructed By Cross correlation (mm)**	**Located By Chi-square fit (mm)**	**Reconstructed By Richardson-Lucy (mm)**
20130306_134651	(0,0)	(0.7,0.75)	(0.25,0.25)	(0.5,0.4)
20130306_140913	(0,-10.25)	(0.2,-9.75)	(0.25,-10.0)	(0.25,-9.7)
20130306_142555	(0,10.25)	(0.5,11.0)	(0.5,11.0)	(0.5,11.0)
20130306_144252	(-10.25,0)	(-9.85,0.5)	(-10.0,0.0)	(-9.75,0.25)
20130306_145822	(10.25,0)	(11.0,0.5)	(11.0,0.5)	(10.65,0.35)
SIMULTANEOUS TWO-SOURCE TEST				
20130729_Am	(-10.25,0)	(-9.0,0.0)	(-9.0,-0.25)	(-9.0,-0.2)
20130729_Co	(10.25,0)	(10.7,-1.0)	(10.75,-1.0)	(10.5,-1.25)

It is noticed that the results from the three different methods agree well, to within 0.5 mm. The difference between the reconstructed position and the source position set at the laboratory is well within 1mm, except for one case where it is found to be 1.25 mm. This discrepancy may in part be due to the inaccuracy in the manual placement of the radioactive sources. Reduced ability of discrimination due to diverging radiation beam is another contributory factor, as the shadow cast by one mask element occupies nearly 4.6mm x 4.6mm on the detector instead of 2.5mm x 2.5mm expected from a parallel beam. Nevertheless, the location accuracy of 1 mm here corresponds to an angular accuracy of 3.8 arcmin. This is expected to improve significantly in flight operations, with the benefit of a parallel beam and multiple detector modules. The results above show that both CC and RL methods can be used to provide initial source locations in the reconstruction process. The final step will always involve shadow fitting by chi-square minimization, which is essential to correctly estimate the strengths of the detected sources.

The reconstructed profiles in both CC and RL methods are clean, without the evidence of any secondary false peak. Given that only a small portion of the mask pattern is being effectively used in this experiment, this is a rather heartening result.

The Full Width at Half maximum (FWHM) of the Point Spread Functions (PSFs) after reconstruction are typically less than 1mm x 1mm across, both CC and RL methods yielding similar PSFs. At 122 keV, the PSF is seen to widen slightly, by about 10%. Above 100 keV the mask plate begins to become transparent, reducing shadow contrast and worsening the imaging capability. As a result, PSF degradation is indeed expected. The results here, however, show that decent imaging would still be possible at energies as high as 120 keV, with a PSF of less than ~4 arcmin FWHM.

Dipankar Bhattacharya
Ajay Vibhute
25.10.2013

APPENDIX I: Detailed results of individual reconstructions

Reconstruction bin size 0.25mm x 0.25mm
Mask height is 484mm from the detector plane. Mask dimension 39mmx39mm

Data file 20130306_134651_MULTI_Am2_600_023C_40keV_regular
Source Positioned at (0mm,0mm); height from detector plane 897.5 mm

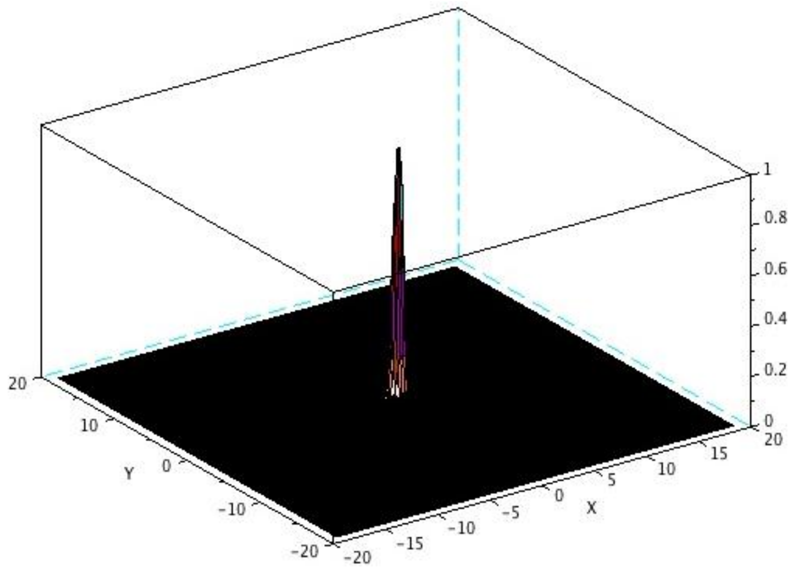

Reconstructed

Source profile,

Richardson-Lucy

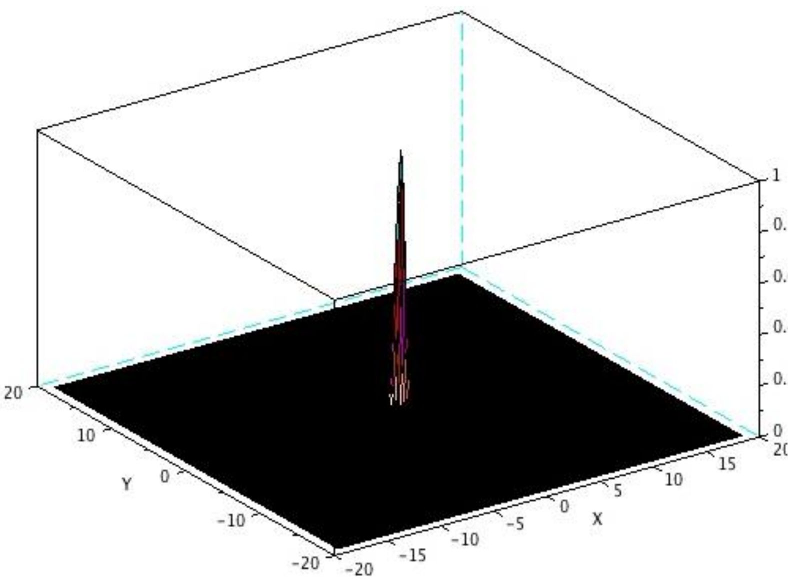

Reconstructed

Source profile,

Cross-correlation

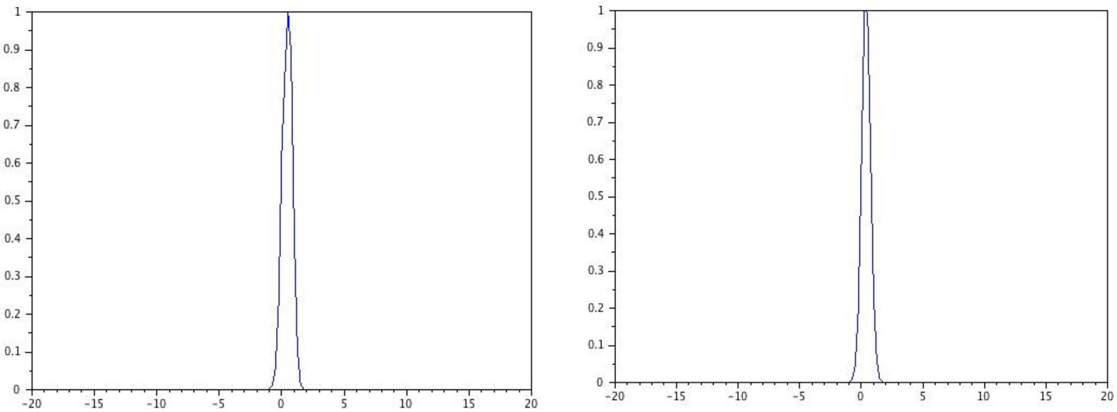

PSF x-section (left) and y-section (right) for RL reconstruction

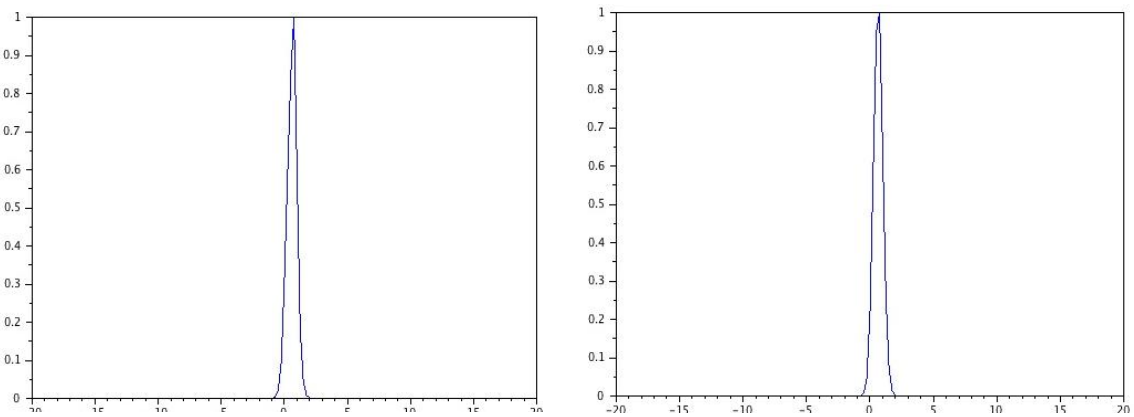

PSF x-section (left) and y-section (right) for CC reconstruction

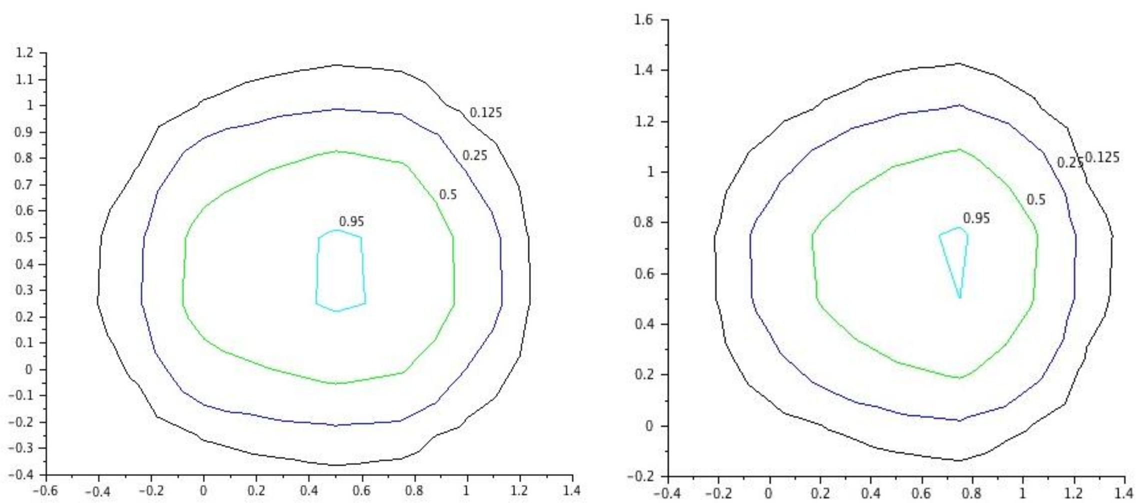

Profile contours: RL (left), CC (right). The green contour is at half maximum

	RL	**CC**
Central location (x,y) mm	0.5, 0.4	0.7, 0.75
FWHM (DX x DY) mm (arcmin)	1.0 x 0.85 (3.8 x 3.2)	0.85 x 0.85 (3.2 x 3.2)

Data 20130306_140913_MULTI_Am2_600_023C_40keV_regular
Source positioned at (0mm,-10.25mm) ; height from detector plane 897.5 mm

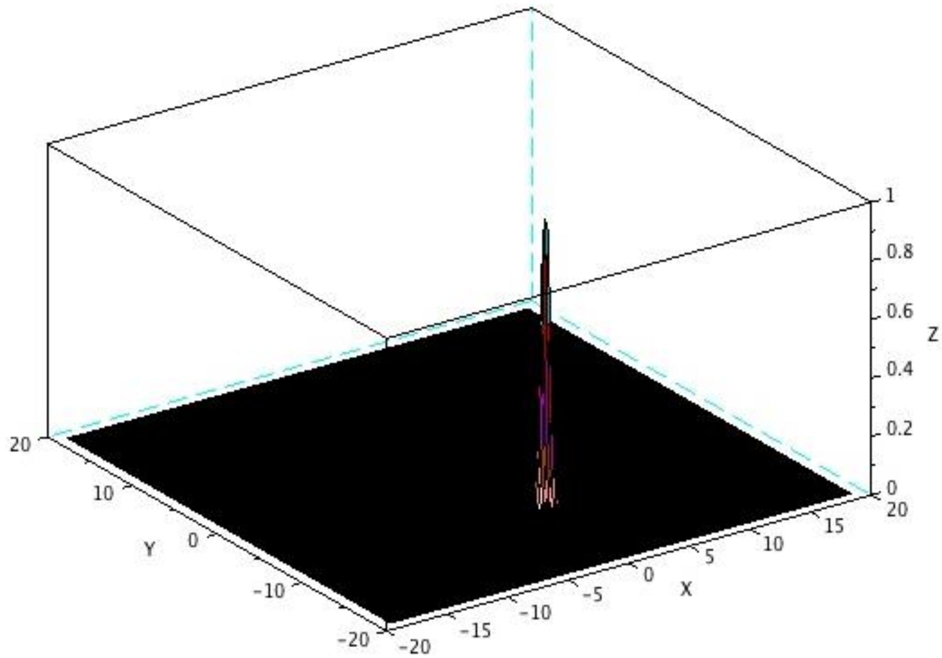

Reconstructed

Source profile,

Richardson-Lucy

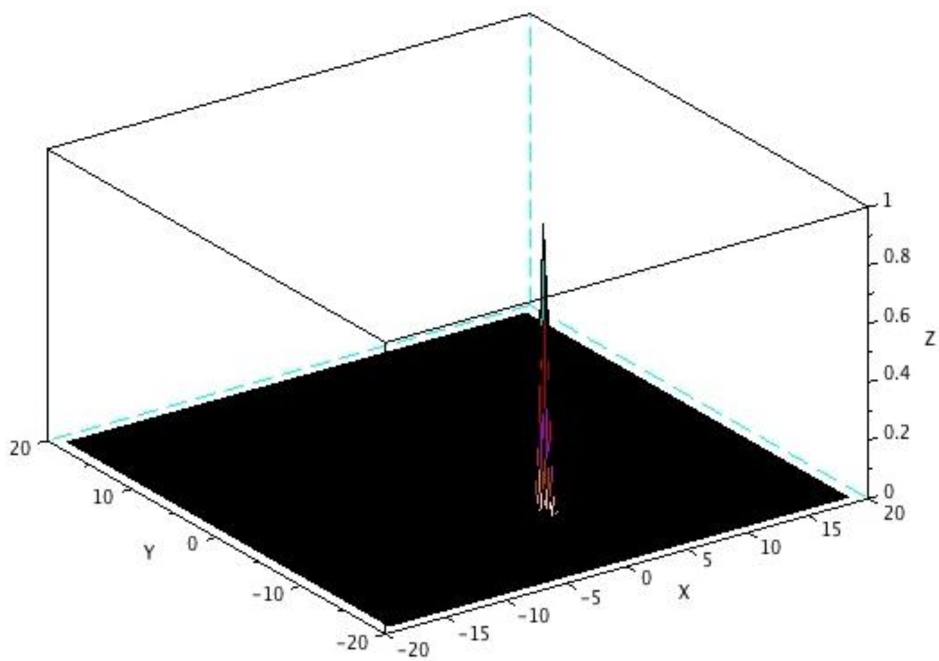

Reconstructed

Source profile,

Cross-correlation

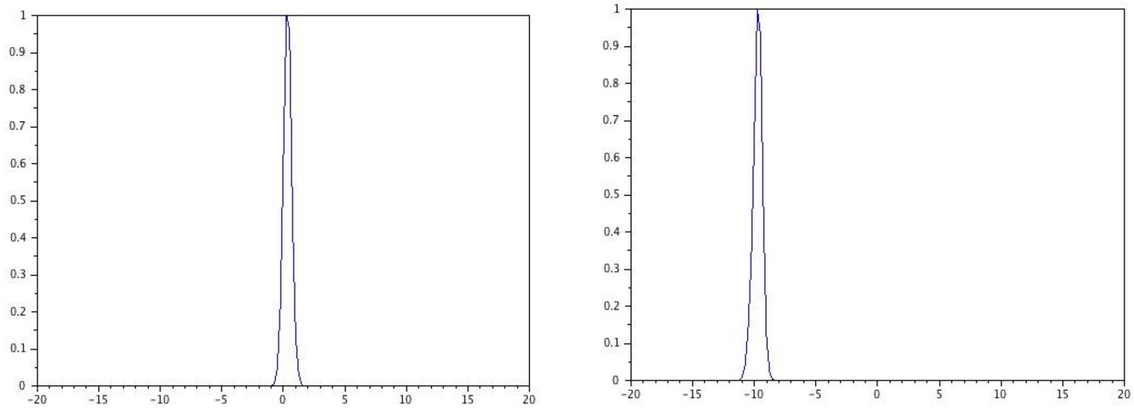

PSF x-section (left) and y-section (right) for RL reconstruction

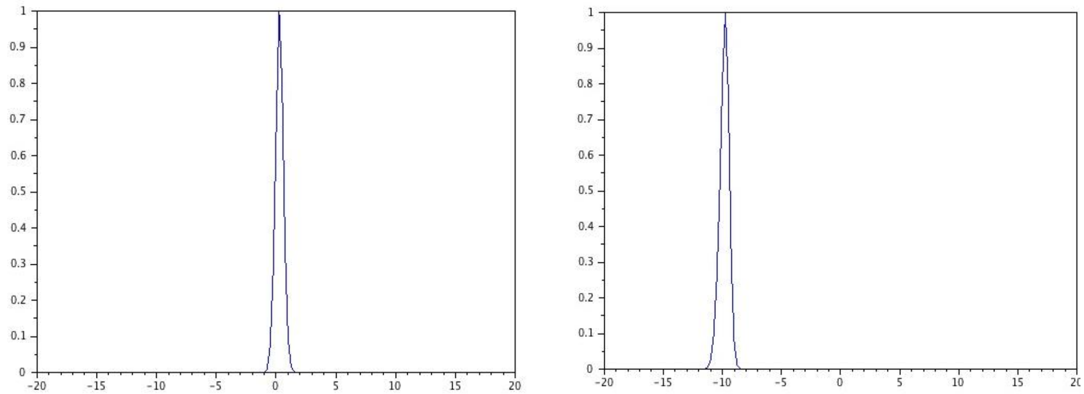

PSF x-section (left) and y-section (right) for CC reconstruction

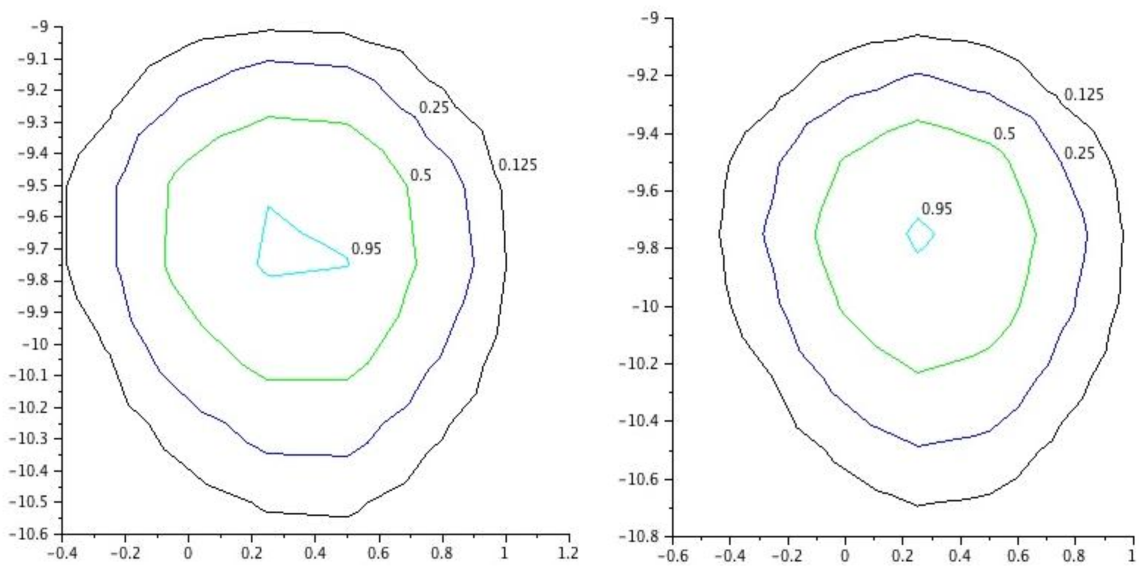

Profile contours: RL (left), CC (right). The green contour is at half maximum

	RL	**CC**
Central location (x,y) mm	0.25,-9.7	0.2,-9.75
FWHM (DX x DY) mm (arcmin)	0.8 x 0.8 (3.0 x 3.0)	0.8 x 0.85 (3.0 x 3.2)

Data 20130306_142555_MULTI_Am2_600_023C_40keV_regular
Source positioned at (0mm,10.25mm); height from detector plane 897.5 mm

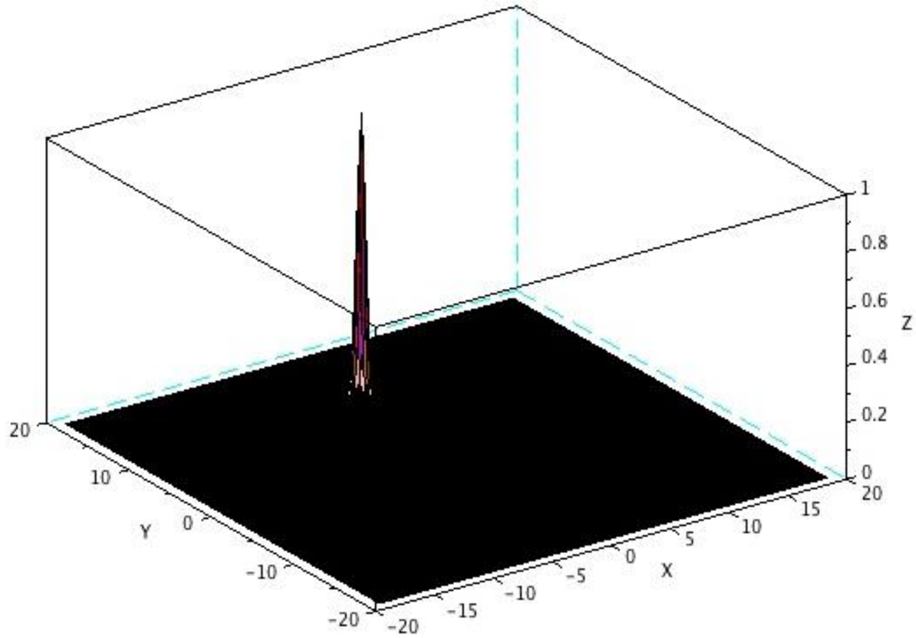

Reconstructed

Source profile,

Richardson-Lucy

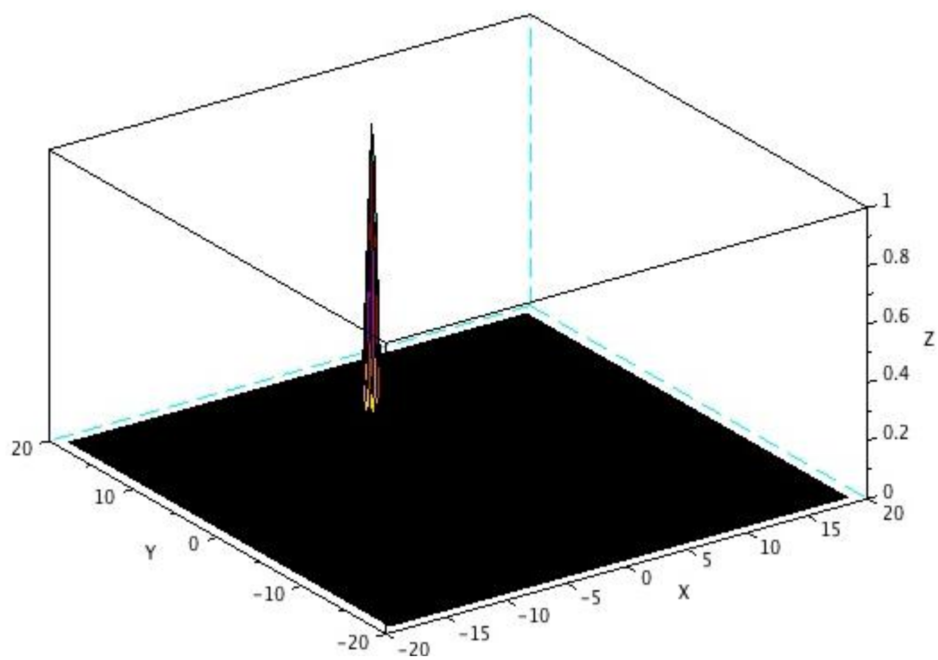

Reconstructed

Source profile,

Cross-correlation

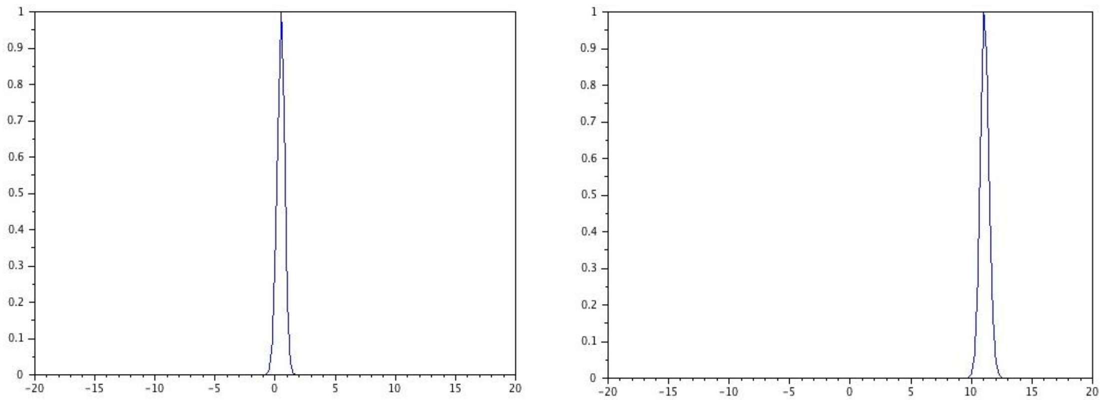

PSF x-section (left) and y-section (right) for RL reconstruction

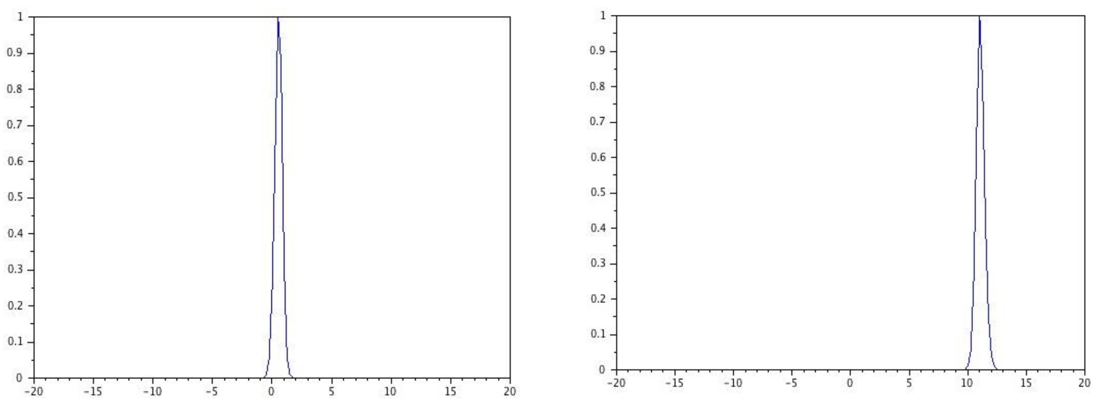

PSF x-section (left) and y-section (right) for CC reconstruction

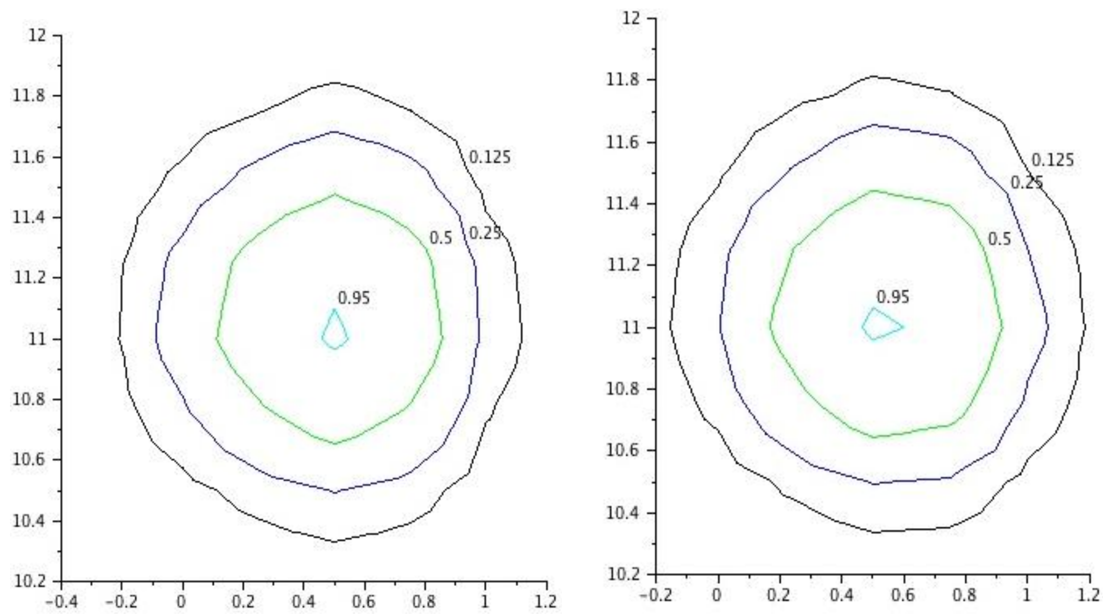

Profile contours: RL (left), CC (right). The green contour is at half maximum

	RL	**CC**
Central location (x,y) mm	0.5, 11.0	0.5, 11.0
FWHM (DX x DY) mm (arcmin)	0.75 x 0.8 (2.8 x 3.0)	0.75 x 0.8 (2.8 x 3.0)

Data 20130306_144252_MULTI_Am2_600_023C_40keV_regular
Source positioned at (-10.25mm,0mm); height from detector plane 897.5 mm

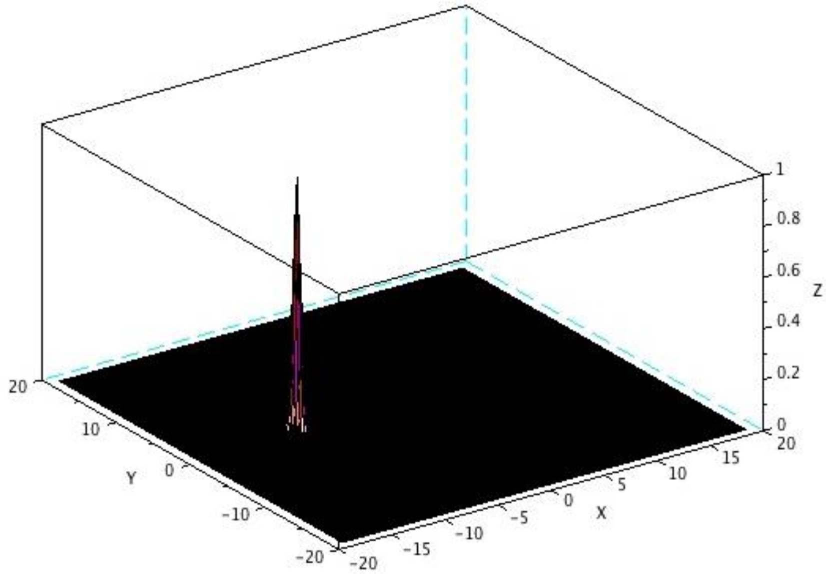

Reconstructed

Source profile,

Richardson-Lucy

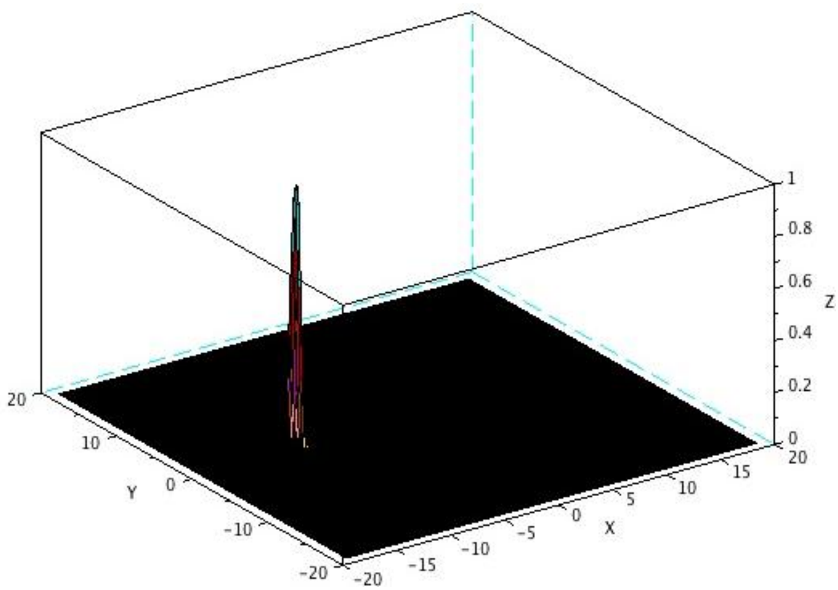

Reconstructed

Source profile,

Cross-correlation

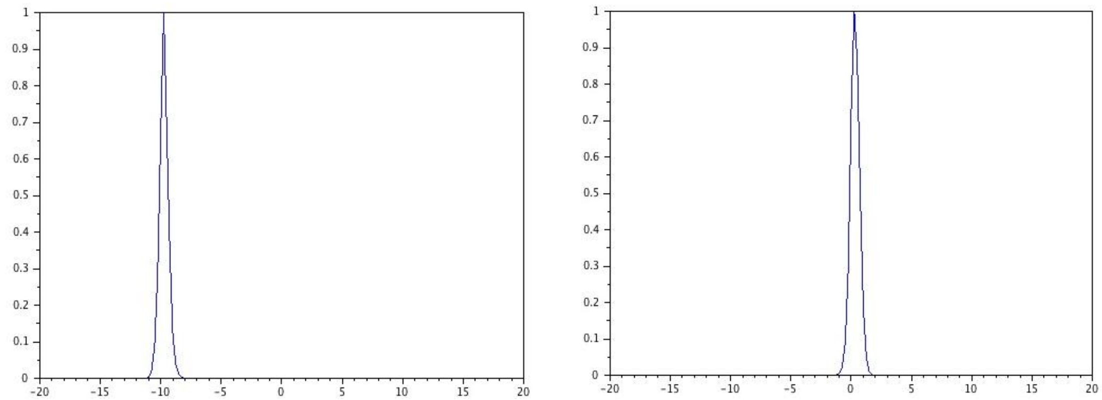

PSF x-section (left) and y-section (right) for RL reconstruction

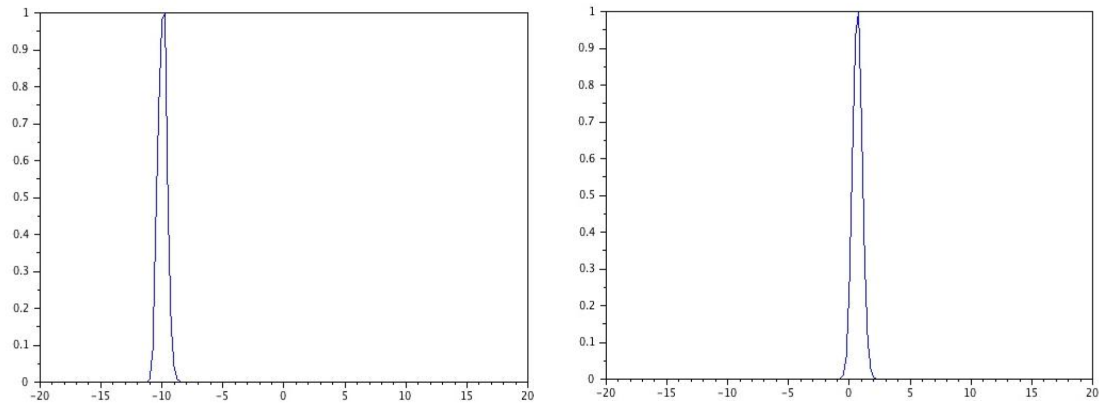

PSF x-section (left) and y-section (right) for CC reconstruction

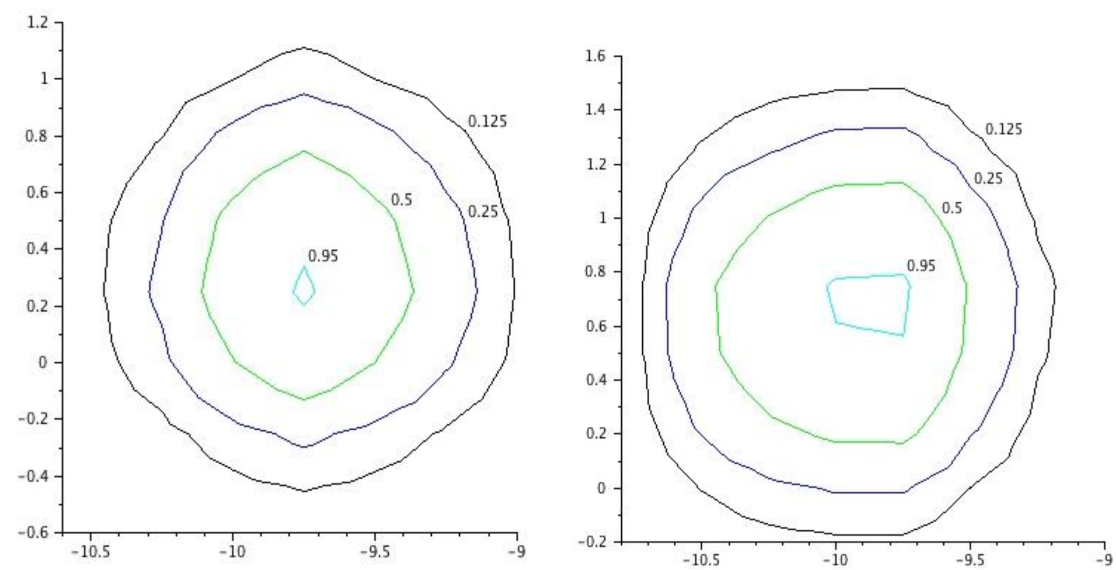

Profile contours: RL (left), CC (right). The green contour is at half maximum

	RL	CC
Central location (x,y) mm	-9.75, 0.25	-9.85, 0.5
FWHM (DX x DY) mm (arcmin)	0.75 x 0.9 (2.8 x 3.4)	0.9 x 0.9 (3.4 x 3.4)

Data 20130306_145822_MULTI_Am2_600_023C_40keV_regular
Source positioned at (10.25mm,0.0mm); height from detector plane 897.5 mm

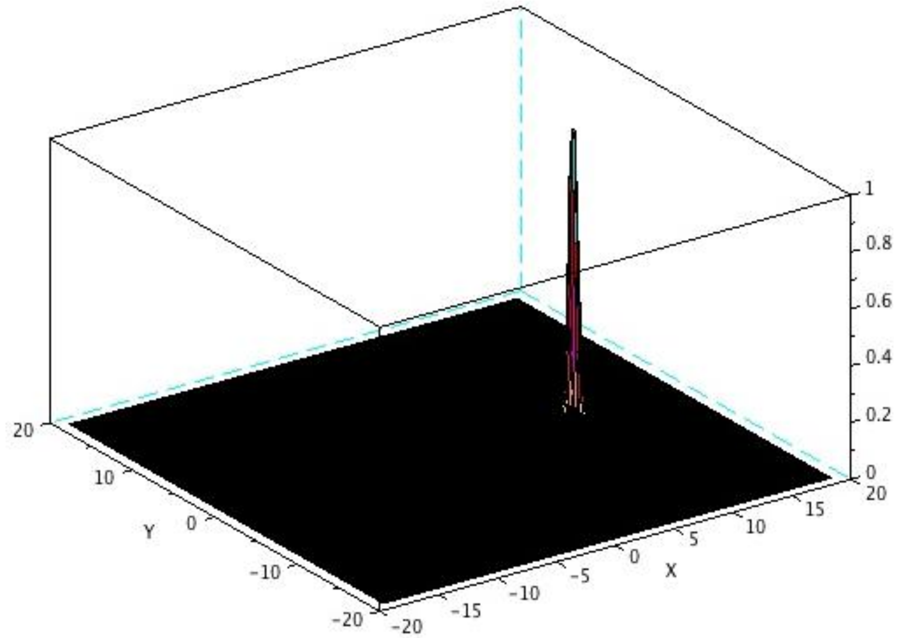

Reconstructed

Source profile,

Richardson-Lucy

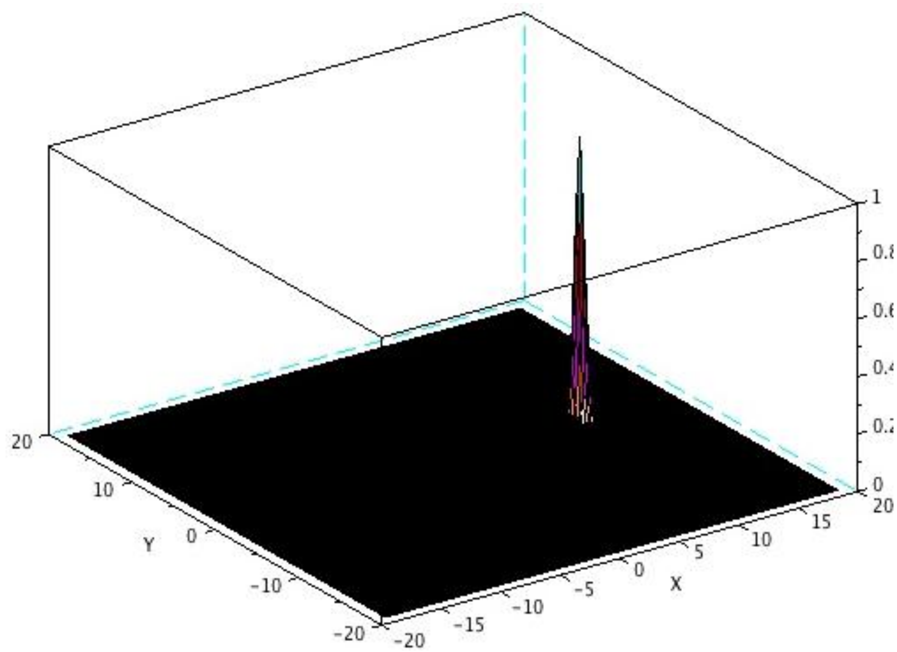

Reconstructed

Source profile,

Cross-correlation

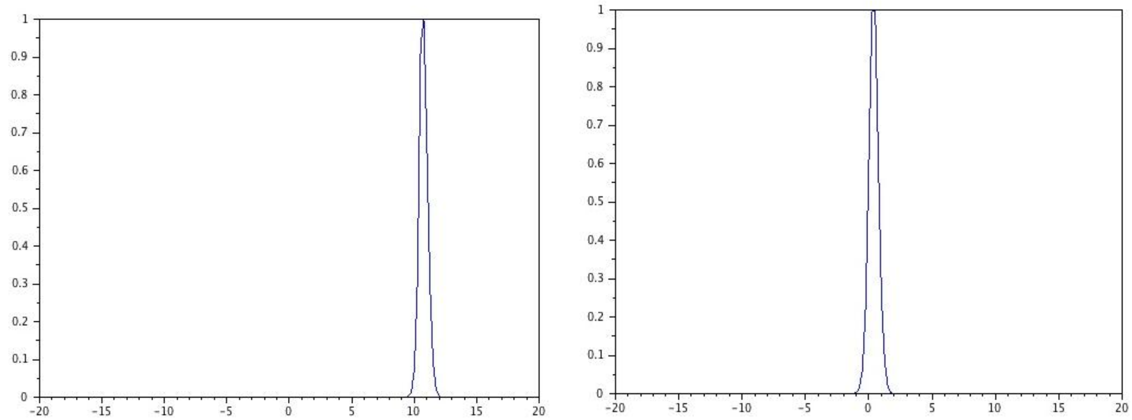

PSF x-section (left) and y-section (right) for RL reconstruction

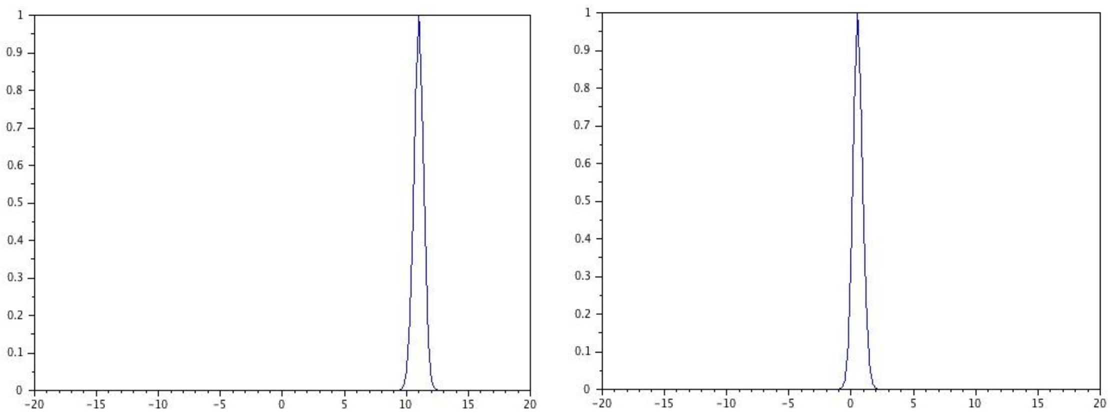

PSF x-section (left) and y-section (right) for CC reconstruction

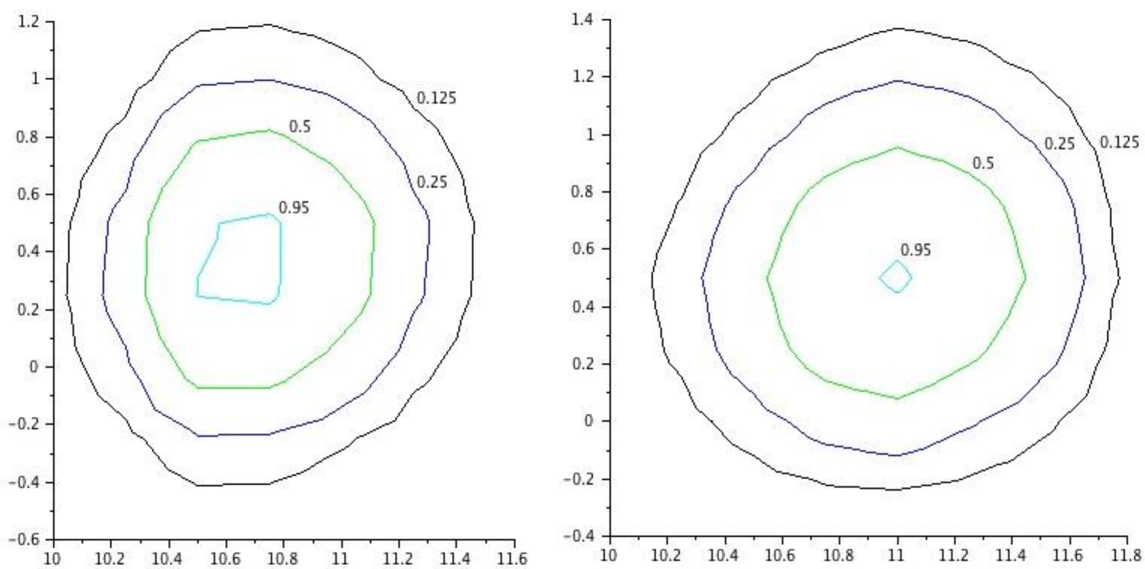

Profile contours: RL (left), CC (right). The green contour is at half maximum

	RL	CC
Central location (x,y) mm	10.65, 0.35	11.0, 0.5
FWHM (DX x DY) mm (arcmin)	0.8 x 0.9 (3.0 x 3.4)	0.9 x 0.9 (3.4 x 3.4)

Test of Energy Dependence of PSF, if any

One observation was carried out with simultaneous exposure of two radioactive sources, an Americium source with a 60 keV line and another Cobalt source with a 122keV line, shining on the same module. The sources were separated in the x-direction and placed at locations (-10.25,0) and (10.25,0) respectively.

The resultant data were analysed by first constructing the Detector Plane Histograms for the two energies separately – namely, events recorded with energy near 60 keV and with those near 122 keV were binned separately. These two DPHs were then subjected individually to Richardson-Lucy reconstruction. The results are displayed below.

Data: 20130729_161532_MULTI_Co2_600_022C_40keV_regular
(Cobalt source, 122 keV); position (10.25,0); height from detector plane 895.5 mm

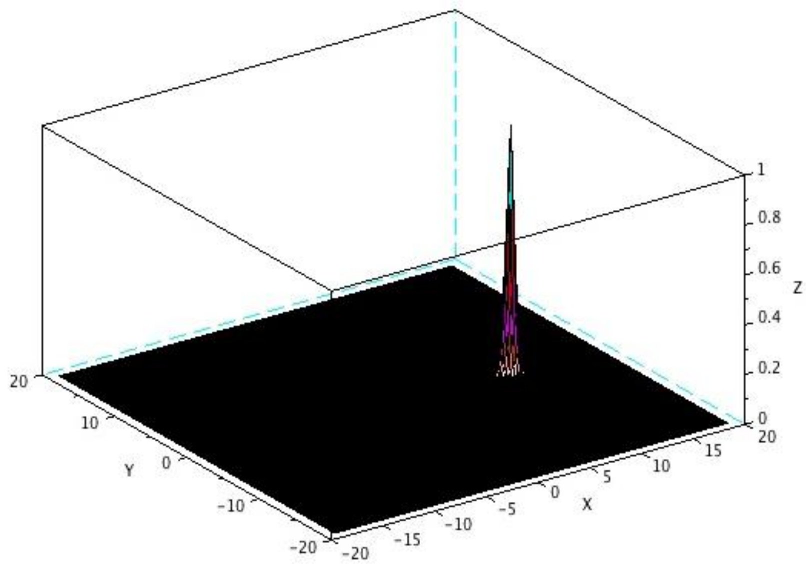

Reconstructed

Source profile,

Richardson-Lucy

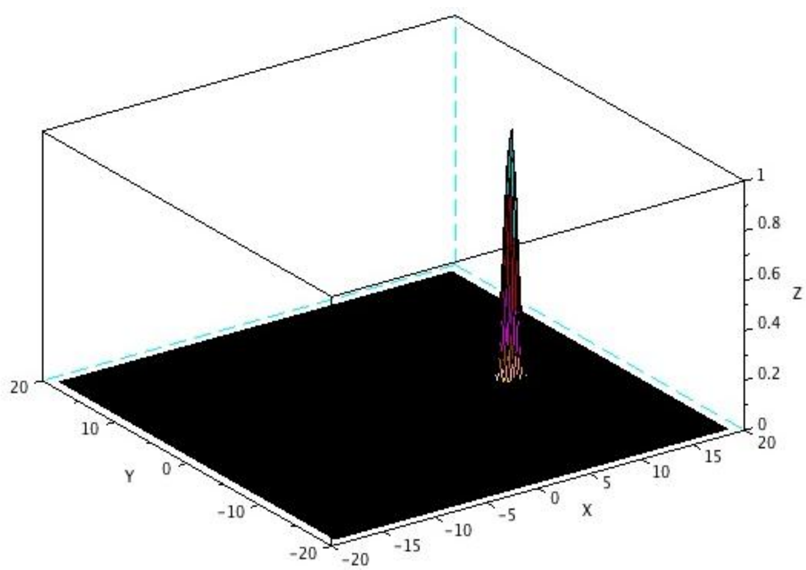

Reconstructed

Source profile,

Cross-correlation

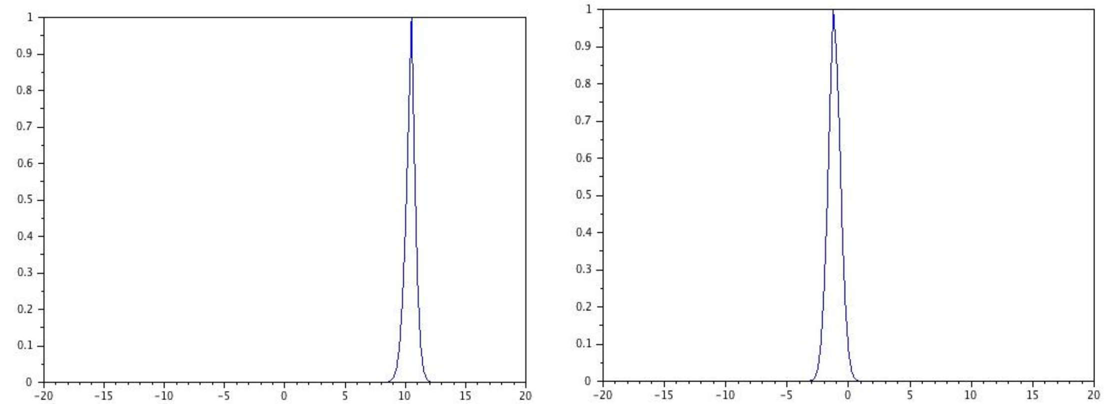

PSF x-section (left) and y-section (right) for RL reconstruction

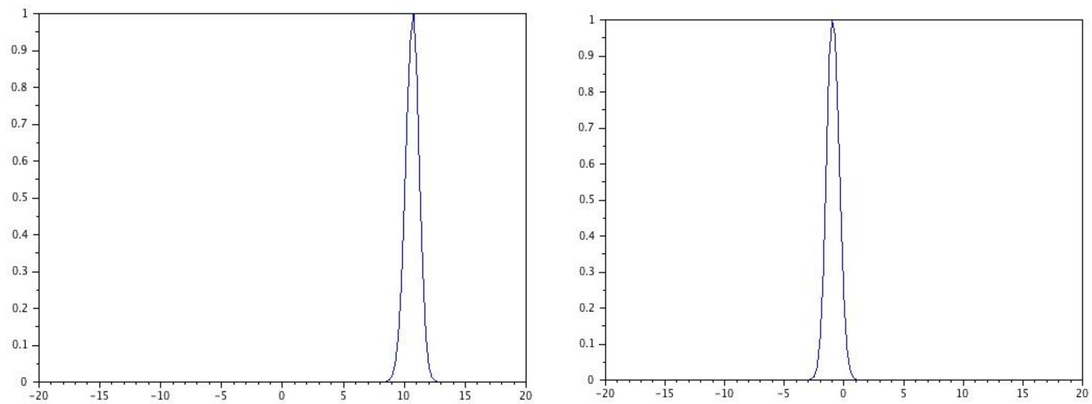

PSF x-section (left) and y-section (right) for CC reconstruction

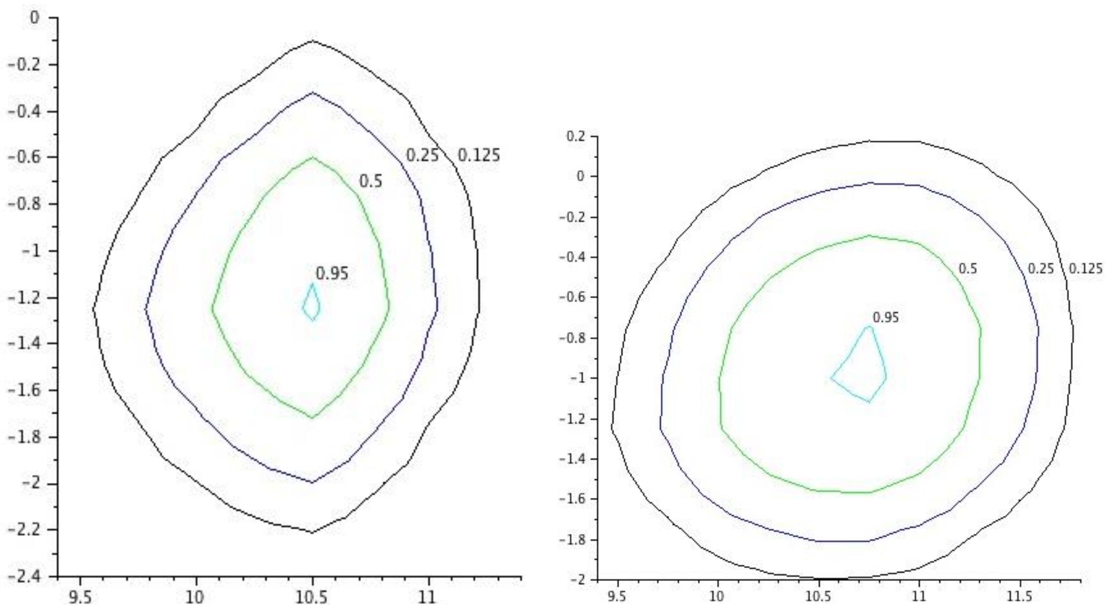

Profile contours: RL (left), CC (right). The green contour is at half maximum

	RL	**CC**
Central location (x,y) mm	10.5, -1.25	10.7, -1.0
FWHM (DX x DY) mm (arcmin)	0.75 x 1.1 (2.8 x 4.1)	1.1 x 1.2 (4.1 x 4.5)

Data: 20130729_161532_MULTI_Am2_600_022C_40keV_regular
(Americium source, 60 keV); position (-10.25,0); height from detector 897.5 mm

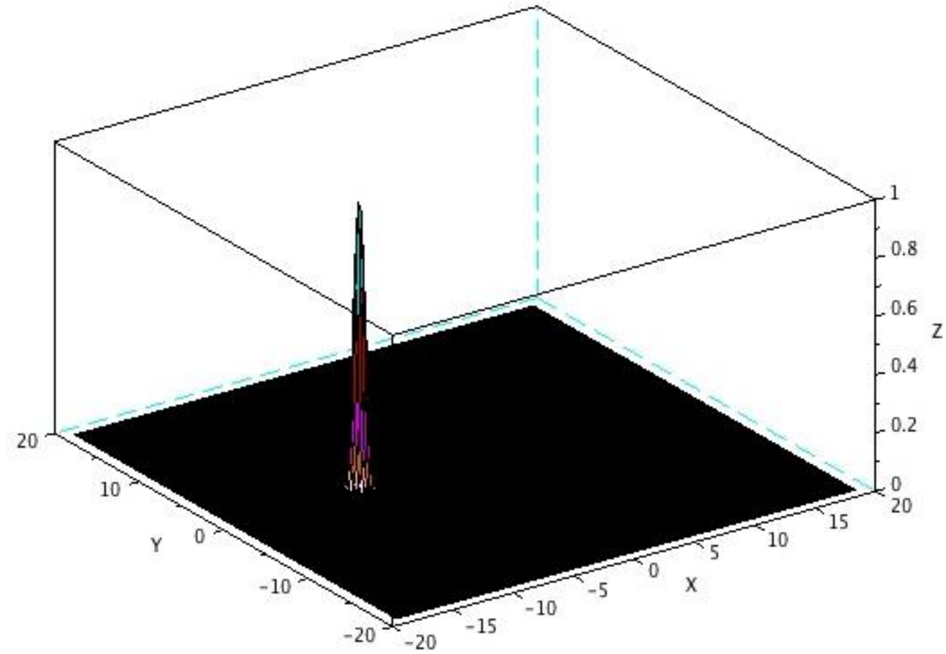

Reconstructed

Source profile,

Richardson-Lucy

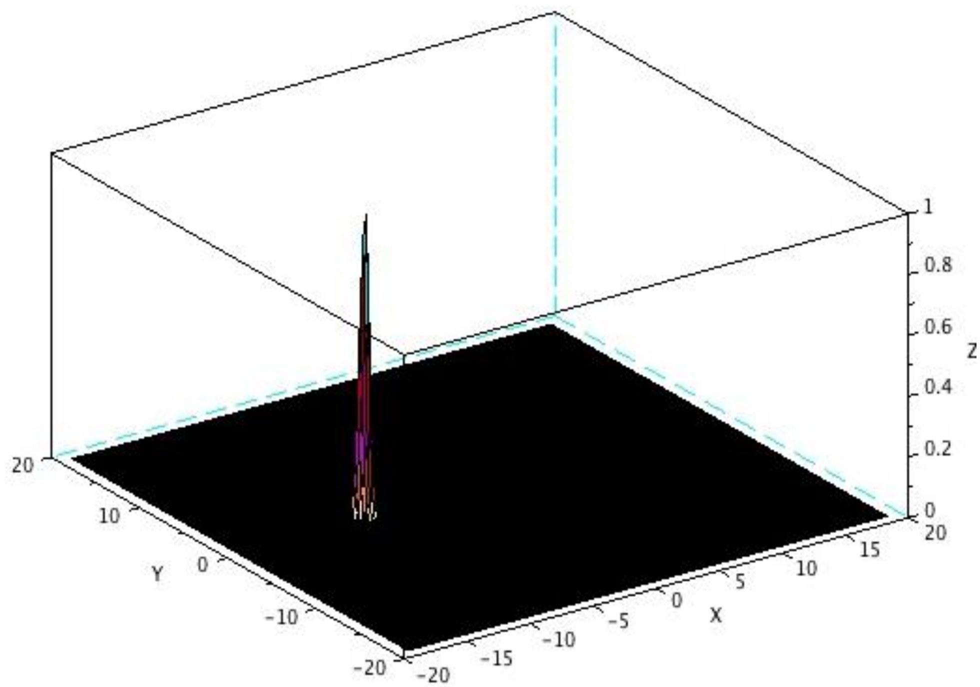

Reconstructed

Source profile,

Cross-correlation

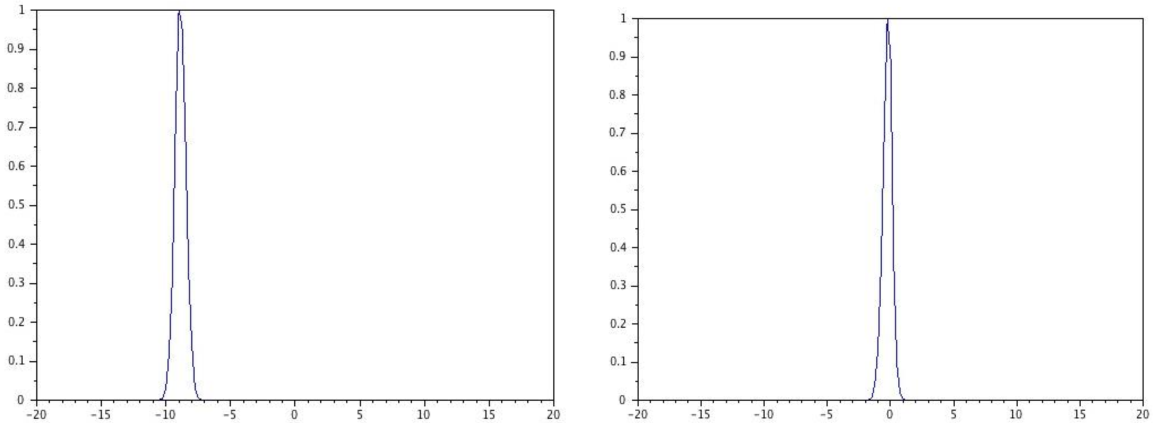

PSF x-section (left) and y-section (right) for RL reconstruction

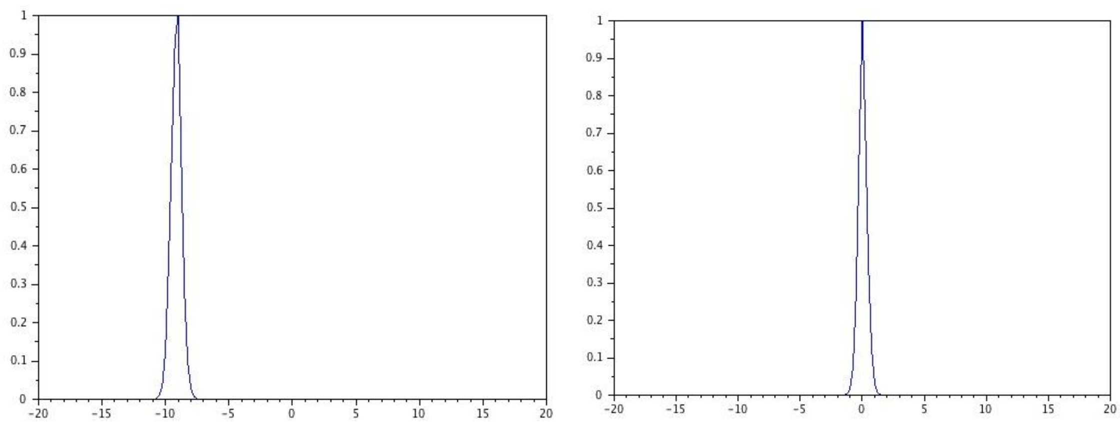

PSF x-section (left) and y-section (right) for CC reconstruction

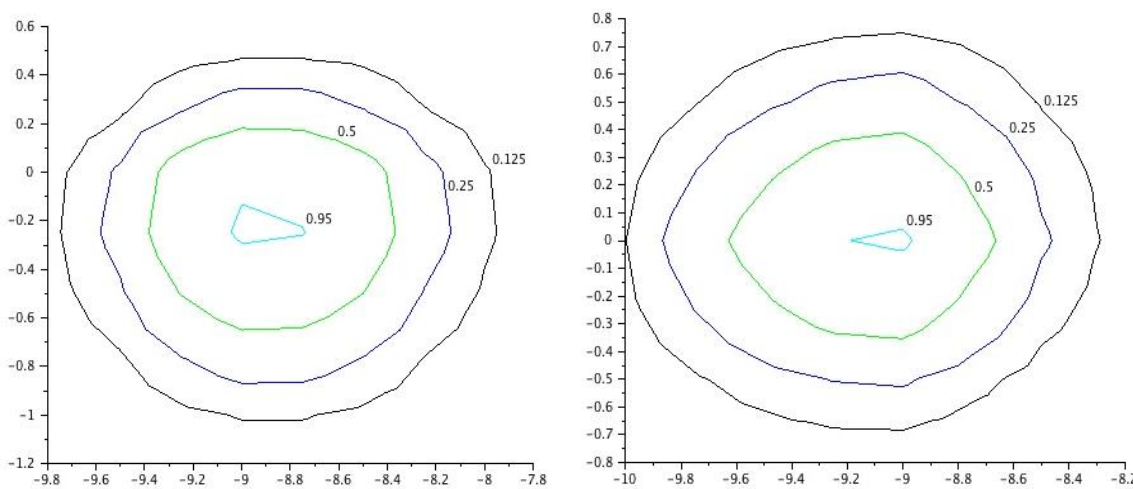

Profile contours: RL (left), CC (right). The green contour is at half maximum

	RL	CC
Central location (x,y) mm	-9.0, -0.2	-9.0, 0.0
FWHM (DX x DY) mm (arcmin)	1.0 x 0.8 (3.8 x 3.0)	0.9 x 0.7 (3.4 x 2.7)

Annexure II

Individual pixel calibration of a large area CZT detector array

N. Vagshette[a], P. Pawar[b], V. Bhalerao[a], D. Bhattacharya[a], A. R. Rao[c]

[a]*Inter-University Centre for Astronomy and Astrophysics, Pune, India*
[b]*S.R.T.M. University, Nanded, India*
[c]*Tata Institute of Fundamental Research, Mumbai, India*

Abstract

Large area hard X-ray detectors used in astronomy are prone to systematic errors in their data. Pixelated hard X-ray detectors like Cadmium Zinc Telluride offer the opportunity to calibrate the individual pixels and understand these systematics at the basic pixel levels. Here we describe the calibration technique used for the CZT-Imager payload of the ASTROSAT satellite. We use the alpha-tag technique to calibrate the individual pixels in the detector. The simultaneity of the X-rays and the alpha particles are determined digitally and we describe the methodology and the experimental setup used for tuning the design parameters. We demonstrate the use of alpha-tagging method for gain calibration of a set of pixels in the detector array.

Keywords: X- and γ-ray spectroscopy, X- and γ-ray telescopes and instrumentation, Laboratory experiments

1. Introduction

Cadmium Zinc Telluride (CZT) semiconductor detectors have been extensively used in hard X-ray astronomy during the past few years. These detectors have relatively high atomic numbers (Cd = 48, Te=52 and Zn=30) and higher band gap energy (E_{CZT}=1.6 eV) and hence it is easy to operate them at near room temperatures. Because of the high atomic number (Z), a few mm of CZT detector can easily absorb hard X-rays up to ~100 keV. Therefore, CZT detectors have been used in many X-ray space missions like Swift, INTEGRAL and most recently NuSTAR [1, 2, 3, 4]. The use of CZT detectors in X-ray astronomy is mainly due to their superior spectral resolution, temporal resolution and imaging capability.

CZT-Imager (CZTI) is one among four X-ray instruments on board the multi-wavelength astronomy satellite *ASTROSAT*[5, 6]. ASTROSAT CZTI covers the hard X-ray band, with a broad energy response from 10 to 100 keV. The instrument consists of 64 CZT modules divided into 4 quadrants, giving a total collecting area of 976 cm^2. The basic modules, procured from Orbotech Medical Solutions, are similar to those used in the Chandrayaan-I HEX payload [7, 8] and the Coronas-Photon RT-2 payload [9].

Well-calibrated X-ray detectors are crucial for characterising and measuring the X-ray emission process from astrophysical sources. X-ray detectors are generally characterised in two steps: (i) extensive ground testing to determine the various calibration parameters (like the energy scale) and (ii) in–orbit monitoring of these calibration parameters using an internal calibration source. The most commonly used radioactive source is Americium 241 (^{241}Am) which emits continuous calibration lines with energy between 13 keV and 60 keV. For example, the calibration of CZT detector for Swift Burst Alert Telescope (BAT) is done by using two ^{241}Am tagged sources mounted below the coded aperture mask, for calibrating the absolute energy scale and the detector efficiency for each CZT pixel in-flight [10].

In the CZTI payload, alpha tagging is done in a novel way by using scintillator detectors and photodiodes [6]. In this paper we describe the digital coincidence techniques used for tagging the X-rays, and demonstrate the efficacy of the method with laboratory test data.

2. Alpha tagging using ^{241}Am

Americium 241 is a man–made radioactive source which is directly obtained from plutonium bombarded with alpha particles. It decays by alpha particle emission (at 5485 keV - 84.5% and 5443 keV - 13%) to ^{237}Np [11]. The half-life of this decay is 432.2 years.

Email address: nilkanth@iucaa.ernet.in (A. R. Rao)

Because many of the resulting states are metastable, these decays are accompanied by low energy gamma radiations with the discrete energies at 59.5 keV (35.9%) being the most important one along with 26.35 keV (2.4%) and 13.9 keV (42%) emission. The details of the design of alpha-tag source and alpha-tagging methodology is given in [6]. To detect the alpha particles simultaneous to the X-ray emission a compact low mass alpha-tagged X-ray source was developed. The ^{241}Am source is embedded in a radiation detector which detects the alpha particles but is transparent to the X-rays (mainly 60 keV and hence lower energies would not be visible in this set up). Alpha particle and X-rays are simultaneously emitted from the ^{241}Am source and a Cesium Iodide (CsI(TI)) detects the alpha particles but it is transparent to X-rays. The light output created by the interaction of a alpha particle with CsI is detected by a photo-diode which converts it into an electric pulse, which is further amplified by a Charge Sensitive Preamplifier (CSPA). The setup of ^{241}Am source, CsI(TI), photo-diode and CSPA is called 'alpha module' and the whole setup is called the alpha tag (or alpha tag electronics). Some of the X-rays which escape from CsI are detected in the CZT detector. Since the processing of each interaction is done independently, there could be time lags between 5 and 15 μs in the alpha pulse with respect to X-ray pulse, due to different electronics characteristics. To identify all the detected source photons correctly with respective tagged alpha, we introduce two time scales: t_1 and t_2. When a CZT event is detected, the processing electronics waits for a time t_1 before deciding whether an alpha pulse is registered. When the alpha electronics detects a pulse, this information is deemed active for a time t_2. Both times can be varied by a digital command to the system.

The data modes for the CZT-Imager are described elsewhere [12]. The data are always stored in an event mode: each event, i.e., an ionising event in the main CZT module, is characterised by a pixel-id (8 bits; indicating the pixel number in each CZT module of 256 pixels), detector-id (4 bits; indicating the module number in the 16 module quadrant), and pulse height of the ionising event digitised to 12 bits. Each event is time stamped with a 16 bit clock with a least count of 20 μs. Further, one bit information indicates whether the alpha detector was active during the reading of the CZT. Another 8 bits provide veto detector information. These time tagged event data are packaged every second and each packet contains a header information which gives, among other house keeping information, the total number of alpha events detected in the alpha detector in one second (called $R_{s,head}$).

3. Experimental data

The experimental verification was done with two steps: first a single module was used to shine the alpha tagged X-rays at close quarters (to optimise the digital settings, t_1, and t_2) and then with these settings data is obtained for long duration in the flight settings. For the former one module was chosen (module number 5 of quadrant 2 of the flight model - FM2). Long duration data having exposure time (t) of 3600 s were obtained with operating temperature of 21° C. The source and background data were collected with different threshold of time t_1 and t_2 (in μs). In the experimental setup necessary care was taken to reduce the noise which are produced by X-rays coming from other directions. To check the variation of alpha and background counts with different combination of t_1 and t_2, we have generated the count map (alpha and total) and spectrum (alpha+total). Whereas time t_1 was chosen to be from 1μs and 2μs, and t_2 was taken to be one of 4μs, 5μs, 6μs, 7μs, 8μs, 9μs and 10μs.

3.1. Integrated spectrum

To see the spectral distribution of alpha tag sources and X-ray background, we have plotted together the alpha spectrum and total (alpha+background) spectrum. Spectrum of module 5 at time t_1=1μs and t_2=8μs is shown in fig 1. As alpha tag spectrum has very low counts, to enhance the feature, we have multiplied the alpha tag spectrum by a factor such that the background count in the channel range between 1500-2000 is the same as the total spectrum. The reciprocal of this multiplication factor is called the background suppression factor, f_{bg}. After multiplication, spectrum clearly shows the emission peak at around 1250 channel/59.5 keV (i.e. ^{241}Am X-ray source line) plus continuum. We have used a Gaussian function to fit this peak after subtracting the continuum emission. We compare this peak position and width (at t_1=1 and t_2=8 μs) obtained by fitting Gaussian function with calibrated spectra of ^{241}Am photopeak for same 59.5 keV emission line. A fit to both ^{241}Am α and calibrated photon peak led to peak centroids that agree within 3% (calibrated peak 1241.3±13.9) and resolution that agree within 37% (sigma=45.0±3.1). In figure 1 the blue colour profile shows the total spectrum, red colour profile shows the α spectrum, the green colour profile is the continuum subtracted α spectrum which was fitted with Gaussian function shown in black line. We calculate the peak position and resolution of alpha tag spectra of 1 hour of integration by various number of pixel grouping and we found that the the minimum number of 25 pixel group

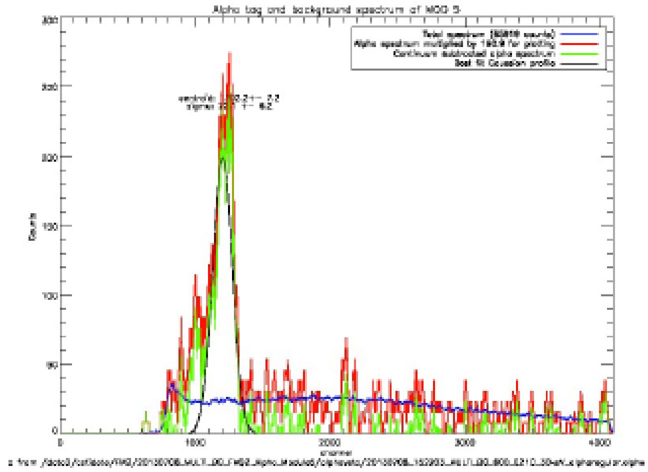

Figure 1: The integrated spectrum of alpha tag source (in red colour) and background (in blue colour) at time t_1=1 and t_2=8 μs.

t1	t2	peak	sigma
1	5	1222.1 ± 13.8	31.7 ±13.8
1	6	1229.0 ± 7.6	52.3 ±6.7
1	7	1234.2 ± 4.9	45.8 ±4.3
1	8	1202.2 ± 7.2	72.1 ±6.2
1	9	1232.7 ± 4.0	46.1 ±3.4
1	10	1214.8 ± 5.0	75.1 ±4.6
2	5	1278.4 ± 12.3	14.0 ±11.0
2	6	1239.3 ± 11.0	40.0 ±9.3
2	7	1215.4 ± 9.4	62.7 ±8.1
2	8	1220.2 ± 6.6	47.6 ±5.6
2	9	1230.7 ± 5.1	41.7 ±4.4
2	10	1247.8 ± 3.2	47.8 ±2.7

Table 1: alpha spectrum of FM2 module 5 at different time t_1 and t_2 is fitted with Gaussian function

is needed to estimate the peak position and resolution of spectra.

To calibrate the CZT detector we need an accurate detection of source spectrum. We shall use the observed α and photon detection rates, total observation time and time t_2 to calculate the coincident events (counts registered on the CZT detector, which matches with a corresponding α particle) as well as factor by which background is being suppressed in the coincident events f_{bg} (i.e. background reduction factor). To estimate the number of coincident events we calculate the parameters like the rate of α emission R_α (i.e. α counts per total observation time), rate of background photon R_b (i.e. background counts per total observation time) and the total observation time 't'. Therefore, the total number of α particles detected is R_αt and total background photon detected is R_bt. Each alpha detection is followed by a high time t_2, so that averaged number of background photons detected during that time is $R_b t_2$. In our case R_b ~ 18 / sec and t_2 is in the range of 4 - 10 μs, so $R_b t_2$ << 1, therefore the probability of multiple coincidence is negligible. The probability of single photon coinciding with alpha particle is $\approx R_b t_2$ and the total number of alpha particles detected is R_αt, so that the total number of coincidence events is expected to be $R_b t_2 \times R_\alpha$t, whereas R_bt is nothing but N_{bg}. Therefore, the another way of calculating the background suppression factor is

$$f_{bg} = \frac{coincident\ background\ counts\ detected}{total\ background\ counts}$$

$$= \frac{N_{bg} R_\alpha t_2}{N_{bg}} = R_\alpha t_2$$

Thus, in this case, the background reduction factor is independent of the background rate R_b.

We demonstrate this by plotting observed f_{bg} against the waiting time t_2 in Figure 2. As expected they are related linearly. We find a zero shift corresponding to about 1 μs which is understood as the result of the algorithm used in the onboard software: the event occurrence time and the micro-second counting are done independent to each other and as soon as an alpha event is recorded the register storing the value of t_2 is decremented by one resulting in an effective alpha waiting

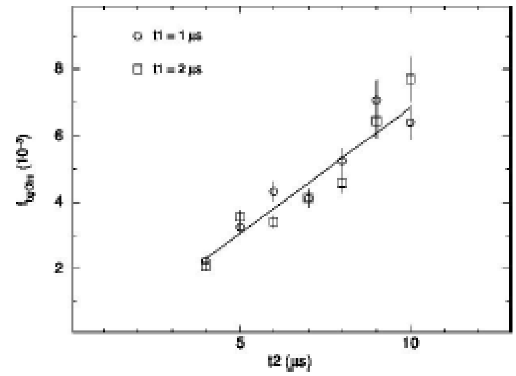

Figure 2: Plot of observed f_{bg} against the waiting time t2. The straight line is a linear fit to the data.

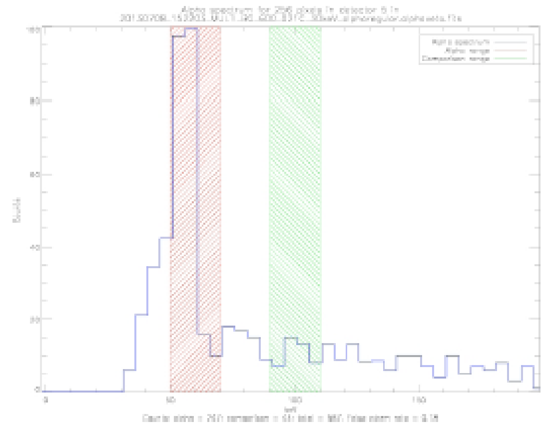

Figure 3: shows the gainoffset corrected spectra of alpha tag sources.

time of (t_2 - 1) μs. The slope of the relation corresponds an alpha count of 760±90 events per second which agrees with the alpha event recorded in the header (810 events per second).

Finally, we estimate the source count (and rate) by subtracting the estimated total number of background coincident events ($f_{bg}N_{bg}$) from the coincidence photon counts in in the source energy range $N_{sc,t}$. Thus, the total source counts N_s is given by

$$N_s = N_{sc,t} - f_{bg}N_{bg}$$

and the source rate

$$R_s = \frac{N_s}{t}$$

Similarly, the signal to noise defined as the R_s / ($R_{bg}f_{bg}$), see column 7 in table 3.

We have also plotted the gain-offset corrected spectra of alpha-tag source. Fig 3 shows the gain-offset corrected alpha-tagged spectra of module 5. The peak of the spectra is found to be at 59.5 keV ^{241}Am. To find the strength of signal at 59.5 keV we extracted the count in the spectra of two different region, one is in the energy range of 50 - 70 keV i.e. ^{241}Am line peak at 59.5 keV which is shown in red color rectangle box in figure and other was taken for comparison in the energy range 90 - 110 keV in green colour box. table 3 col. 12 and 13 shows the counts in the 50 - 70 keV, 90 - 110 keV and the ratio of comparison region to alpha region counts at different combination of t_1 and t_2.

3.2. *Count maps*

To find the information of each pixel and their response to alpha tag source, we produce the count maps of alpha tagged source. To calculate the number of alpha counts recorded by each pixel we use

$$N_s = N_{sc,t} - f_{bg}N_{bg}$$

The count map of alpha tagged source of module 5 at t_1=1μs and t_2=8μs is shown in fig 4. At different combination t_1 and t_2, we produced the count map and corresponding histogram. In this map (fig 4) each square indicates the one pixel area and the color associated with it shows the net count on that pixel. The different color shows the different count value. The histogram of this figure shows the number of pixels associated with alpha value. In this histogram the black continuum is the fit of Poissonian function, the cross points are values which are estimated by numerically from histogram and the errorbars are the poissonian error, the mean of this function is found to be 0.86±0.022.

4. QM module Integrated Spectra

In this section, we study the alpha tag technique for the Qualificaltion Model (QM) modules, here we follow a procedure similar to the one mentioned above for FM2 module 5. In this case we calculate the coincident event and background suppression factor for all modules at t_1 = 1 and t_2 = 8 μs. Long duration data having exposure time of 50400 s have been taken. For calculation we have used the alpha counts and total counts below 1500 channel (~70 keV) which are given in table 4 col 2 and 3. Initially we calculated the background suppression factor which is the reciprocal of multiplication factor (as defined above). Using the background suppression factor we calculated the source count and source rate

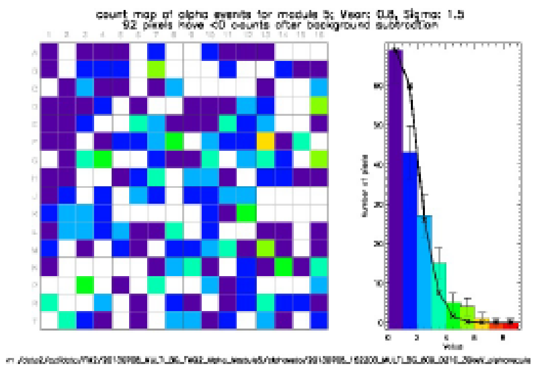

Figure 4: shows the count map of alpha events detected on module 5 and histogram of count map

mod no.	peak	sigma
00	1219.2 ± 0.6	54.7 ± 0.6
01	1219.9 ± 0.5	64.9 ± 0.4
02	1234.5 ± 0.4	58.0 ± 0.3
03	1215.2 ± 1.0	56.9 ± 0.8
05	1229.5 ± 1.0	60.5 ± 0.9
06	1231.6 ± 1.3	50.6 ± 1.2
07	975.4 ± 1.2	52.8 ± 1.1
08	1223.0 ± 3.2	53.5 ± 3.1
11	1217.1 ± 4.2	70.6 ± 4.0
14	1220.3 ± 4.3	63.1 ± 4.1

Table 2: alpha spectrum of QM modules at time t_1= 1 and t_2= 8 μs are fitted with Gaussian function

by subtracting the total number of background coincident events from the source counts in the source energy range, whereas the total detected background is used in the same energy range. In table 4 col. 4 and 5 show the background suppression factor and source rate for different modules. We have plotted the α and total emission spectra of all QM modules whereas the α spectra was well fitted with Gaussian function (see figure 5) using the same technique as we use the above FM2 module 5 data. The best fitted peak position and sigma values were reported in table 2.

It can be noticed that the background in the QM has a hump in the low energies. These are attributed to the fluorescent K_α and K_β lines of Tantalum (at 57.52 keV and 65.21 keV, respectively). A fit to the background data is shown in figure 6. Using these lines (along with the alpha tagged 59.5 keV) line, one can derive the gain and offset of each module, as shown for module 11 in figure 7.

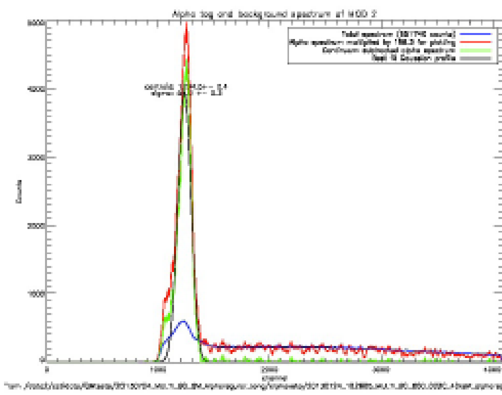

Figure 5: : figure shows the integrated spectrum of QM module 02 alpha tag source (in red colour) and background (in blue colour) at time t_1=1 and t_2=8 μs.

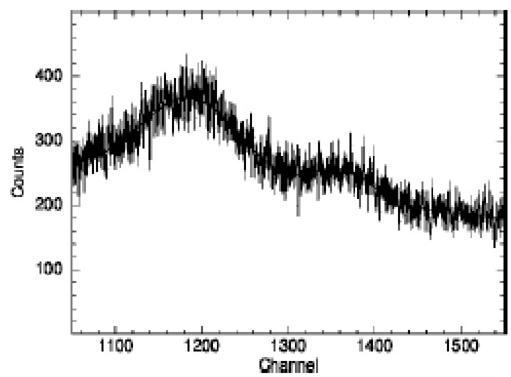

Figure 6: Background spectrum of QM which shows the fluorescent K_α and K_β lines plus straight line background. The line emission was well fitted with Gaussian function.

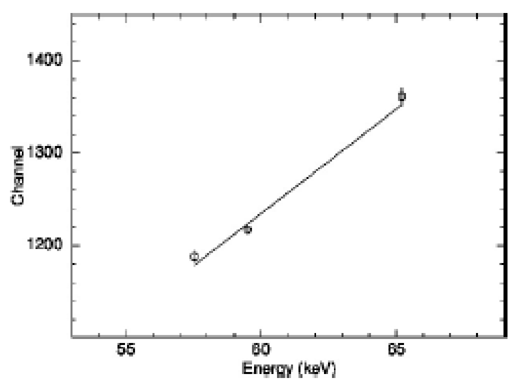

Figure 7: This figure plots the known energy verses corresponding peak position at particular channel, which was well fitted with least square fit method. The slope and intercept gives the gain and offset value of this module (QM module 11)

5. Conclusion

We have used an alpha tagged calibration technique for CZT detector. The experimental data were taken by using the different combination of time t_1 (look up time) and t_2 (scatter time). Analysis of the experimental data shows that the background suppression factor is depend only on time t_2. The background suppression factor increases monotonically by increasing the time t_2 from 4 to 10 μs. It is also seen that the background suppression factor increases by factor 2 when time t_2 is increased from 1 to 6 μs but it increases linearly (one-to-one correspondence) from 7 to 10 μs. Using the false alarm probability we notice that the time t_1=1 μs and t_2=8μs is good proxy for alpha tagged calibration; because the probability of background alpha emission is less then the other time scale.

The extremely low calibration count rate (less than 0.1 counts s^{-1} per module with a typical background rate of 15 counts s^{-1}) ensures that there is negligible false identification of genuine events as alpha tagged events (less than 0.1%), but still we can extract module wise gain information. Using the background lines, it is possible to identify the gain-offset of a set of pixels (a minimum of 25 pixels).

Table 3: Summary of FM2 mod 05 alpha tag calibration

t_1 (μs)	t_2 (μs)	$C_\alpha(\leq 70keV)$ (cts)	$C_{bg}(\leq 70keV)$ (cts)	$R_{s,head}$ (cts s^{-1})	f_{bgEst} (10^{-3})	f_{bgObs} (10^{-3})	$Ratio_{f_{bg}}$ (Est/Obs)	$R_{s,obs}$ (cts s^{-1})	$Ratio_{rate}$ (10^{-5})	SNR —	C_{60} (cts)	C_{100} (cts)	$C_{60by100}$ —
1	2	3	4	5	6	7	8	9	10	11	12	13	14
1	4	52	16397	809.48±27.06	3.24±0.108	2.24± 0.106	1.45±0.08	0.004 ±0.0025	0.53	0.42±0.24	37	20	1.85±0.513
1	5	132	16756	809.71±26.92	4.05±0.135	3.24± 0.184	1.25±0.08	0.022 ±0.0041	2.67	1.43±0.27	99	35	2.83±0.556
1	6	221	16676	809.37±27.64	4.86±0.166	4.33± 0.284	1.12±0.08	0.041 ±0.0055	5.11	2.06±0.27	155	39	3.97±0.712
1	7	277	16445	810.00±27.49	5.67±0.192	4.12± 0.265	1.37±0.11	0.058 ±0.0058	7.17	3.08±0.31	211	56	3.77±0.566
1	8	321	16463	809.23±27.41	6.47±0.219	5.24± 0.379	1.24±0.10	0.065 ±0.0067	8.06	2.72±0.28	247	44	5.61±0.919
1	9	347	16401	810.20±26.91	7.29±0.242	7.07± 0.594	1.03±0.09	0.064 ±0.0079	7.92	1.99±0.25	253	66	3.83±0.530
1	10	364	16704	809.54±26.47	8.10±0.265	6.41± 0.514	1.26±0.11	0.071 ±0.0077	8.81	2.40±0.26	277	67	4.13±0.563
2	4	43	16521	809.95±27.43	3.24±0.110	2.09± 0.096	1.55±0.09	0.002 ±0.0023	0.29	0.24±0.24	23	21	1.10±0.331
2	5	88	16357	808.77±27.34	4.04±0.137	3.55± 0.211	1.14±0.08	0.008 ±0.0036	1.03	0.52±0.22	50	29	1.72±0.402
2	6	149	16515	808.88±27.66	4.85±0.166	3.41± 0.199	1.42±0.09	0.026 ±0.0043	3.18	1.65±0.28	107	35	3.06±0.595
2	7	248	16327	809.63±27.26	5.67±0.191	4.14± 0.267	1.37±0.10	0.050 ±0.0056	6.19	2.67±0.30	177	42	4.21±0.723
2	8	301	16444	818.95±27.84	6.55±0.223	4.98± 0.352	1.31±0.10	0.061 ±0.0064	7.43	2.67±0.30	216	62	3.48±0.252
2	9	354	22505	809.31±27.14	7.28±0.244	6.45± 0.518	1.13±0.09	0.058 ±0.0085	6.80	1.98±0.30	240	65	3.69±0.266
2	10	345	16691	809.33±27.54	8.09±0.275	7.71± 0.677	1.05±0.09	0.060 ±0.0083	7.42	1.68±0.23	256	76	3.37±0.440

note: col. 1&2 are the time t1 and t2 in μs, col. 3 is alpha counts below 70 keV col. 4 is the total alpha+background counts below 70 keV, col. 5 is the alpha count rate when flag is on (taken from header), col. 6 is the estimated background suppression factor which is independent of background counts, col. 7 is the observed background suppression factor which is reciprocal of multiplication factor, col 8. is the ratio of estimated to observed background suppression factor, col. 9 is the the actual source rate estimated using observed f_{bg}, col. 10 is the ratio of observed to header source rate, col. 11 is the signal to noise ratio ($R_{s,obs}/R_{bkg}f_{bg,obs}$), col. 12 and 13 are the counts taken in peak emission region (i.e. between 50-70 keV) and comparator (90 - 110 keV) and col. 14 is the ratio of counts in peak emission to comparator.

Table 4: Summary of QM modues of alpha tag calibration at time t_1=1 and t_2=8 μs

mod no	$C_\alpha(\leq 1500cha)$	$C_{bg}(\leq 1500cha)$	f_{bg}	R_s	SNR	$C_{peak} \pm 40cha$	$C_{1460-1540}$	$C_{peak-by-comp}$
—	(cts)	(cts)	(10^{-3})	(cts s^{-1})	—	(cts)	(cts)	—
1	2	3	4	5	6	7	8	9
0	2328	165863	5.11±0.365	0.029±0.0022	1.75±0.13	962	89	10.81
1	4708	192066	4.85±0.337	0.075±0.0026	4.06±0.14	1959	100	19.59
2	4233	181419	5.30±0.386	0.065±0.0027	3.40±0.14	1820	87	20.92
3	2217	172855	4.71±0.324	0.028±0.0020	1.72±0.13	762	101	7.54
5	1513	144130	4.76±0.328	0.016±0.0017	1.21±0.13	551	75	7.35
6	1283	129161	5.39±0.396	0.012±0.0017	0.84±0.12	502	79	6.35
7	1604	216132	4.93±0.347	0.011±0.0023	0.50±0.11	425	106	4.01
8	1070	159970	4.84±0.336	0.006±0.0017	0.38±0.11	293	90	3.26
11	921	141311	5.43±0.401	0.003±0.0017	0.20±0.11	203	99	2.05
14	896	152071	4.88±0.341	0.003±0.0016	0.21±0.11	206	106	1.94

note: col. 1 is the mod no, col. 2 is alpha counts below 1500 channel col. 3 is the total alpha+background counts below 1500 channel, col. 4 is the observed background suppression factor, col. 5 is the alpha count rate, col. 6 is the signal to noise ratio. col. 7 and 8 are the counts taken in peak emission region (i.e. between peak±40 channel) and for comparator we used counts in channel between 1460 - 1540 and col. 10 is the ratio of counts in peak emission to comparator.

References

[1] S. D. Barthelmy, L. M. Barbier, J. R. Cummings, E. E. Fenimore, N. Gehrels, D. Hullinger, H. A. Krimm, C. B. Markwardt, D. M. Palmer, A. Parsons, G. Sato, M. Suzuki, T. Takahashi, M. Tashiro, J. Tueller, The Burst Alert Telescope (BAT) on the SWIFT Midex Mission, Space Sci. Rev.120 (2005) 143–164. arXiv:arXiv:astro-ph/0507410, doi:10.1007/s11214-005-5096-3.

[2] P. Ubertini, F. Lebrun, G. Di Cocco, A. Bazzano, A. J. Bird, K. Broenstad, A. Goldwurm, G. La Rosa, C. Labanti, P. Laurent, I. F. Mirabel, E. M. Quadrini, B. Ramsey, V. Reglero, L. Sabau, B. Sacco, R. Staubert, L. Vigroux, M. C. Weisskopf, A. A. Zdziarski, IBIS: The Imager on-board INTEGRAL, A&A411 (2003) L131–L139. doi:10.1051/0004-6361:20031224.

[3] T. Kitaguchi, B. W. Grefenstette, F. A. Harrison, H. Miyasaka, V. B. Bhalerao, W. R. Cook, III, P. H. Mao, V. R. Rana, S. E. Boggs, A. C. Zoglauer, Spectral calibration and modeling of the NuSTAR CdZnTe pixel detectors, in: Society of Photo-Optical Instrumentation Engineers (SPIE) Conference Series, Vol. 8145 of Society of Photo-Optical Instrumentation Engineers (SPIE) Conference Series, 2011. arXiv:1109.0378, doi:10.1117/12.896972.

[4] V. Bhalerao, Neutron Stars and NuSTAR, Ph.D. thesis, Caltech ¡EMAIL¿varun@astro.caltech.edu¡/EMAIL¿ (May 2012).

[5] P. C. Agrawal, A broad spectral band Indian Astronomy satellite ASTROSAT, Advances in Space Research 38 (2006) 2989–2994. doi:10.1016/j.asr.2006.03.038.

[6] A. R. Rao, S. Naik, M. Patil, J. P. Malkar, R. P. S. Kalyan Kumar, An alpha tagged X-ray source for the calibration of space borne X-ray detectors, Nuclear Instruments and Methods in Physics Research A 616 (2010) 55–58. arXiv:1002.2286, doi:10.1016/j.nima.2010.02.092.

[7] S. V. Vadawale, S. Purohit, M. Shanmugam, Y. B. Acharya, J. N. Goswami, M. Sudhakar, P. Sreekumar, Characterization and selection of CZT detector modules for HEX experiment onboard Chandrayaan-1, Nuclear Instruments and Methods in Physics Research A 598 (2009) 485–495. doi:10.1016/j.nima.2008.09.036.

[8] S. V. Vadawale, M. Shanmugam, S. Purohit, Y. B. Acharya, M. Sudhakar, Experimental measurements of charge carrier mobility: lifetime products for large sample of pixilated CZT detectors, in: Society of Photo-Optical Instrumentation Engineers (SPIE) Conference Series, Vol. 8453 of Society of Photo-Optical Instrumentation Engineers (SPIE) Conference Series, 2012. doi:10.1117/12.931424.

[9] T. B. Kotoch, A. Nandi, D. Debnath, J. P. Malkar, A. R. Rao, M. K. Hingar, V. P. Madhav, S. Sreekumar, S. K. Chakrabarti, Instruments of RT-2 experiment onboard CORONAS-PHOTON and their test and evaluation II: RT-2/CZT payload, Experimental Astronomy 29 (2011) 27–54. arXiv:1011.3331, doi:10.1007/s10686-010-9189-y.

[10] T. Sakamoto, S. D. Barthelmy, L. Barbier, J. R. Cummings, E. E. Fenimore, N. Gehrels, D. Hullinger, H. A. Krimm, C. B. Markwardt, D. M. Palmer, A. M. Parsons, G. Sato, M. Stamatikos, J. Tueller, T. N. Ukwatta, B. Zhang, The First Swift BAT Gamma-Ray Burst Catalog, ApJS175 (2008) 179–190. arXiv:0707.4626, doi:10.1086/523646.

[11] G. Audi, O. Bersillon, J. Blachot, A. Wapstra, The {NUBASE} evaluation of nuclear and decay properties, Nuclear Physics A 624 (1) (1997) 1 – 124. doi:http://dx.doi.org/10.1016/S0375-9474(97)00482-X.
URL http://www.sciencedirect.com/science/article/pii/S037594749700482X

[12] A. R. Rao, in press.